

THREE-DIMENSIONAL RESISTIVITY MODELLING AND
INTERPRETATION OF GEOTHERMAL FIELDS IN THE GEDIZ
GRABEN BY MAGNETOTELLURICS

by

Özlem Hacıođlu

B.S., Geophysical Engineering, Süleyman Demirel University, 2008

M.Sc., Geophysics, Bođaziçi University, 2012

Submitted to Kandilli Observatory and Earthquake
Research Institute in partial fulfillment of the
requirements for the degree of
Doctor of Philosophy

Graduate Program in Geophysics

Bođaziçi University

2018

ACKNOWLEDGEMENTS

I would sincerely like to thank my academic advisor, Assoc. Prof. Dr. Çağrı Diner for his encouragement and support from the first to the last stages of my PhD thesis. I would also like to thank to him especially for giving me the opportunity to work on this subject. He was always constructive in his advices, and his door was always open for me.

I would like to express my appreciation to my co-advisor Prof. Dr. Ahmet Tuğrul Başokur from the Department of Geophysical Engineering of Ankara University. He was abundantly helpful. I would like to thank him especially for providing the MT data utilized in this thesis. He also offered invaluable discussions and advices for this work, and his constructive discussions allow me to better understand the magnetotelluric data, and thus analysis and modeling of the data. He never hesitated while sharing his great knowledge and experiences.

I would also like to thank the members of my thesis monitoring committee, namely Prof. Dr. Semih Ergintav and Assoc. Prof. Dr. İrfan Akça for all of their guidance and valuable feedback throughout this process.

I would like to thank Prof. Dr. Gary Egbert for providing 3D magnetotelluric inversion code, ModEM. I am also grateful to Lemnis Geoscience for providing the 3D-Grid software.

I wish to express my gratitude to the Department of Geophysical Engineering of Karadeniz Technical University for giving me an opportunity to complete my PhD study. I would like to thank the Department of Geophysical Engineering of Ankara University for sharing their computer resources with me. I would also like to thank the Department of Geophysics of Boğaziçi University for providing a good environment for education and research.

I would like to thank Halil Arslan for his help in robust processing and for sharing his knowledge. I also thank the people who contributed to the collection of the MT data.

I am deeply thankful to my spouse Ayhan Hacıoğlu. Without Ayhan's understanding, patience and encouragement, I could not have done this work. I would also like to very sincerely thank my family for their encouragement, constant support and never-ending patience through all stages of my life.

ABSTRACT

THREE-DIMENSIONAL RESISTIVITY MODELLING AND INTERPRETATION OF GEOTHERMAL FIELDS IN THE GEDIZ GRABEN BY MAGNETOTELLURICS

The Gediz Graben hosting several geothermal systems is one of the most promising grabens in terms of temperature and production rate of western Anatolia. In order to provide the most comprehensive understanding about the geothermal systems situated in the graben, specifically about the reservoir types, heat sources and structural controls, 253 MT sites were installed at four different areas of the graben to delineate the electrical resistivity distribution at depth. The wide-band MT data were analyzed by phase tensor analysis, and then the data at 31 selected periods in the range from 0.001 s to 1000 s modeled in three-dimensions (3D). The resulting models reveal three different reservoir types, namely (i) a classical geoelectrical distribution of a high temperature geothermal system, with a prominent highly conductive hydrothermal alteration zone sitting above a more resistive deep reservoir zone, (ii) a deep reservoir zone characterized by fractures within metamorphic rocks in the highly resistive basement and (iii) a shallow reservoir (aquifer) corresponding to the hot springs in the shallow sedimentary layer existing in the Gediz Graben. The heat source of the geothermal systems may be attributed to the heat transfer from the interior of the Earth to the upper crust as a consequence of crustal thinning resulted from the extensional tectonics accompanied by magma intrusions into crust in western Anatolia. The 3D models bring out a well-defined interface between the sedimentary cover and underlying metamorphic basement owing to high resistivity contrast between two layers, characterizing the Gediz detachment fault (GDF). The geothermal fields formed along the southern margin of the graben are spatially coincident with the intersecting zone of two fractures, namely the GDF and high angle normal faults, and the circulation of geothermal fluids in reservoirs are dominantly controlled by these fractured zones and major faults. The crustal scale main graben-bounding fault (MGBF) acts as a conduit through which fluids and heat are

transported from deeper parts of the crust to near surface. The meteoric waters percolating deep into the crust through the north dipping normal faults are probably heated up by magmatic intrusions, and some of geothermal waters containing meteoric and magmatic fluids rise up to surface through the permeable faults, in particular through the lower bounding sub-horizontal GDF. Furthermore, 3D resistivity models suggest a thick sedimentary layer (2500-3000 m) in the middle part of the graben basin. The thickness of the sedimentary layer decreases gradually on the northern and southern margins of the graben and becomes much thinner towards the eastern end of the graben. 3D resistivity models also delineate an undulating basement topography under the conductive sedimentary fill of the graben.

ÖZET

GEDİZ GRABENİ'NDEKİ JEOTERMAL SAHALARIN MANYETOTELLURİK YÖNTEM İLE ÜÇ BOYUTLU ÖZDİRENÇ MODELLEMESİ VE YORUMLANMASI

Birçok jeotermal sisteme ev sahipliği yapan Gediz Grabeni, Batı Anadolu'nun sıcaklık ve üretim oranları açısından en umut verici grabenlerinden biridir. Grabende yer alan jeotermal sistemlerin özellikle rezervuar tipleri, ısı kaynakları ve yapısal kontrolleri hakkında en kapsamlı bilgiyi elde etmek amacıyla, grabendeki dört farklı sahada, yer altı öz direnç dağılımını ortaya koymak amacıyla 253 MT istasyon kurulmuştur. Geniş-bant MT veri faz tensörü yöntemi ile analiz edilmiş ve daha sonra üç-boyutlu (3B) olarak, 0.001 ile 1000 sn arasında seçilen 31 periyotta modellenmiştir. Elde edilen modeller üç farklı rezervuar tipine işaret etmektedir. Bunlar (i) üzerinde bulunan daha yüksek iletkenliğe sahip hidrotermal alterasyon bölgesi ile yüksek sıcaklıklı bir jeotermal sisteme ait klasik bir yer elektrik dağılımı ile karakterize edilen derin bir rezervuar, (ii) yüksek öz dirence sahip metamorfik temel içerisinde kırık ve çatlaklarla karakterize edilen derin bir rezervuar ve (iii) Gediz Grabeni'nde bulunan sığ sedimanter tabakalardaki sıcak kaynak sularına karşılık gelen sığ bir rezervuarın (akifer) varlığı şeklindedir. Jeotermal sistemlerin ısı kaynağı, Batı Anadolu'daki magmatik sokulumların eşlik ettiği açılma tektoniğinden kaynaklanan kabuksal incelmanın bir sonucu olarak yerin iç kısımlarından üst kabuğa doğru olan ısı transferine bağlanabilir. 3B modeller, Gediz sıyrılma fayı (GSF) ile karakterize edilen, sedimanter örtü ve altındaki metamorfik temel arasındaki yüksek öz direnç farklılığı ile ortaya koyulabilen iyi bir şekilde tanımlanmış bir ara yüzey ortaya koymaktadır. Grabenin güney kenarındaki jeotermal alanlar, GDF ve yüksek açılı normal fayların kesiştiği yerlerde bulunmaktadır ve rezervuarlarda bulunan jeotermal akışkanların sirkülasyonu bu faylar tarafından kontrol edilmektedir. Ana graben-sınırlayıcı fay (AGSF), akışkanların ve ısının kabuğun derin kısımlarından yüzeye taşındığı bir kanal görevi görmektedir. Kuzeye eğimli normal faylar boyunca kabuğun derinlerine sızan meteorik sular, muhtemelen magmatik

sokulumlar ile ısınmaktadır ve meteorik-magmatik sıvılar içeren jeotermal suların bir kısmı özellikle GDF ve diğer geçirimli faylar aracılığı ile yüzeye ulaşmaktadır. Ayrıca, 3B özdirenç modelleri, graben baseninin orta kısmında kalın bir sedimanter tabakaya (2500-3000 m) işaret etmektedir. Bu sedimanter tabakanın kalınlığı grabenin kuzey ve güney ucuna doğru kademeli olarak azalmaktadır ve grabenin doğu ucunda çok daha fazla incelmektedir. 3B özdirenç modelleri ayrıca graben boyunca iletken sedimanter dolgu altında ondülasyonlu bir taban topoğrafyası ortaya koymaktadır.

TABLE OF CONTENTS

ACKNOWLEDGEMENTS	ix
ABSTRACT	ix
ÖZET	ixii
TABLE OF CONTENTS	ix
LIST OF FIGURES	xi
LIST OF SYMBOLS	xxiv
LIST OF ACRONYMS/ABBREVIATIONS	xxvii
1. INTRODUCTION	1
2. MAGNETOTELLURIC METHOD IN GEOTHERMAL EXPLORATION	5
2.1. Geothermal Systems Overview	5
2.2. Electrical Conductivity of Rocks	8
2.3. Basic Theory of the Magnetotelluric Method	11
2.4. Transfer Functions of Magnetotelluric Responses	22
2.4.1. The Impedance Tensor	22
3. MAGNETOTELLURIC STUDY OF THE GEDIZ GRABEN GEOTHERMAL FIELDS	24
3.1. Tectonic and Geologic Settings	24
3.1.1. Tectonic Setting	24
3.1.2. Geologic Structure and Stratigraphy	26
3.1.3. Geothermal Manifestations	33
3.2. Magnetotelluric Measurements	37
3.2.1. Data Acquisition	37
3.2.2. Data Processing	40
3.2.3. Data Analysis	44
4. MODELING OF MAGNETOTELLURIC DATA	56
4.1. Magnetotelluric Modeling	56
4.2. Three-Dimensional Inversion of the Gediz Graben Data Set	66
4.3. Three-Dimensional Inversion Results	67
4.3.1. Area A	67

4.3.2. Area B	74
4.3.3. Area C	80
4.3.4. Area D	87
5. SENSITIVITY AND SYNTHETIC TESTS	93
5.1. Sensitivity Tests	93
5.1.1. Test for Area A	93
5.1.2. Test for Area B	97
5.1.3. Test for Area C	99
5.1.4. Test for Area D	101
5.2. Synthetic Tests	103
6. DISCUSSION	115
7. CONCLUSION	125
REFERENCES	1
APPENDIX A: SKEW ANGLES	147
APPENDIX B: INITIAL MODELS	148
APPENDIX C: DATA MISFITS	150

LIST OF FIGURES

Figure 2.1.	A representative model of an ideal geothermal system (modified from Berktold, 1983 and geothermal-energy.org).	5
Figure 2.2.	Conceptual model of a geothermal systems (modified from Pellerin <i>et al.</i> , 1996).	7
Figure 2.3.	Typical electrical conductivity ranges for Earth materials (modified from Palacky, 1987; Marti, 2006 and Miensopust, 2010).	9
Figure 2.4.	Boundary conditions on normal (a) and tangential (b) components of EM fields (modified from Stratton, 1941).	17
Figure 3.1.	Simplified tectonic map of Turkey and surrounding (modified from Barka, 1992; Bozkurt, 2001; Gürer <i>et al.</i> , 2006). Dotted line shows the approximate extent of the Aegean Extensional Province (AEP). DSFZ: Dead Sea Fault Zone, EAFZ: East Anatolian Fault Zone, NAFZ: North Anatolian Fault Zone, NEAFZ: North East Anatolian Fault Zone, GG: Gediz Graben.	25
Figure 3.2.	Simplified geological map of the western Anatolia showing locations of the Gediz and other major grabens (modified from Sözbilir, 2005; Emre and Sözbilir, 2007; Serpen <i>et al.</i> , 2009; Mertoğlu <i>et al.</i> , 2015). White box shows the location of study area, Gediz Graben (GG). NMM: Northern Menderes Massif, CMM: Central Menderes Massif, SMM: Southern Menderes Massif, SG: Simav Graben, KMG: Küçük Menderes Graben, BMG: Büyük Menderes Graben, SDF: Simav Detachment Fault, GDF: Gediz Detachment Fault, BMDF: Büyük Menderes Detachment Fault, K: Kızıldere, G: Germencik.	27

- Figure 3.3. Regional tectonic map of the Gediz Graben, showing the faults, location of the geothermal fields, hot springs, hot water wells and power plants (modified from Oner and Dilek, 2013; Serpen *et al.*, 2009; Yilmazer *et al.*, 2010; Mertoğlu *et al.*, 2015). Regional heat flow values are taken from Erkan (2015). GDF: Gediz Detachment Fault, MGBF: Main Graben-Bounding Fault, NMBF: Northern Margin Bounding Fault. 28
- Figure 3.4. A typical metamorphic core complex composed of a core of metamorphic rocks exposed in a window through non-metamorphic rocks, particularly sedimentary rocks (modified from Fossen, 2016). 30
- Figure 3.5. The field photo displaying Gediz detachment surface (photo taken by Ahmet Tuğrul Başokur and the location pointed out by Erdin Bozkurt). 31
- Figure 3.6. Simplified stratigraphic columnar section of the Gediz Graben and its basement (a) and block diagram (b), illustrating the internal structure of the Gediz Graben and Menderes Massif (modified from Çiftçi and Bozkurt, 2009a; 2009b; Oner and Dilek, 2013). 32
- Figure 3.7. A schematic instrument set up of MT sites used for the field campaigns 38
- Figure 3.8. MT site distribution over the Gediz Graben, showing the location of the MT sites, geothermal fields, hot springs, hot water wells and surface trace of active faults (modified from Yilmazer *et al.*, 2010; Oner and Dilek, 2013; Mertoğlu *et al.*, 2015). Rectangles A, B, C and D are areas for which 3D modeling was performed. MGBF: Main Graben-Bounding Fault, NMBF:Northern Margin Bounding Fault. . . . 39

- Figure 3.9. Observed apparent resistivity and phase curves of four representative sites A-712 from area A, B-405 from area B, C-87-36 from area C and D-90-89 from area D, derived from the off-diagonal components of the impedance tensor Z 43
- Figure 3.10. Graphical representation of a phase tensor ellipse and its invariants Φ_{\min} , Φ_{\max} , β and α (modified from Caldwell *et al.*, 2004). 44
- Figure 3.11. Map view of observed phase tensor ellipses at three selected periods 0.001 s, 1 s, and 286 s for area A. The phase tensor ellipses are normalized with major axes and filled with the skew angle. The black lines indicate surface trace of faults. The gray lines mark the GDF. 47
- Figure 3.12. Map view of observed phase tensor ellipses at three selected periods 0.001 s, 1 s and 286 s for area B. The phase tensor ellipses are normalized with major axes and filled with the skew angle. The black lines indicate surface trace of faults. The gray lines mark the GDF. 48
- Figure 3.13. Map view of observed phase tensor ellipses at three selected periods 0.001 s, 1 s, and 286 s for area C. The phase tensor ellipses are normalized with major axes and filled with the skew angle. The black lines indicate surface trace of faults. 49
- Figure 3.14. Map view of observed phase tensor ellipses at three selected periods 0.001 s, 1 s and 286 s for area D. The phase tensor ellipses are normalized with major axes and filled with the skew angle. The black lines indicate surface trace of faults. The gray lines mark the GDF. 50
- Figure 3.15. Rose diagram representation of regional geoelectric strike angles showing strike estimated from the azimuth of phase tensor for the data from area A for the full period range (a) and different period ranges (b) shown on each subfigures. Red sectors illustrate dominant direction of

strike. Strike values change between 0° and 180°. 0° is north and 90° is east. The resolution of the rose diagrams is 5°..... 51

Figure 3.16. Rose diagram representation of regional geoelectric strike angles showing strike estimated from the azimuth of phase tensor for the data from area B for the full period range (a) and different period ranges (b) shown on each subfigures. Red sectors illustrate dominant direction of strike. Strike values change between 0° and 180°. 0° is north and 90° is east. The resolution of the rose diagrams is 5°..... 52

Figure 3.17. Rose diagram representation of regional geoelectric strike angles showing strike estimated from the azimuth of phase tensor for the data from area C for the full (a and b) and different period ranges (c and d) shown on each subfigures. a and c show strike directions computed for sites located at the northern part of the area C while b and d show strike directions computed for sites located at the southern part of the area C. Red sectors illustrate dominant direction of strike. Strike values change between 0° and 180°. 0° is north and 90° is east. The resolution of the rose diagrams is 5°..... 53

Figure 3.18. Rose diagram representation of regional geoelectric strike angles showing strike estimated from the azimuth of phase tensor for the data from area D for the full (a, b and c) and different period ranges (d, e and f) shown on each subfigures. a and d show strike directions computed for sites located at the northern part of the Gediz Graben, b and d show strike directions computed for sites located at the graben, and c and f show strike directions computed for sites located at the southern part of the graben. Red sectors illustrate dominant direction of strike. Strike values change between 0° and 180°. 0° is north and 90° is east. The resolution of the rose diagrams is 5°..... 54

Figure 4.1. Staggered finite difference grid for the 3D MT forward problem. The partial differential equation is formulated in terms of \mathbf{E} specified on cell edges, which is the primary EM field component. The \mathbf{H} components that can be specified naturally on the cell faces are the secondary EM field in this numerical formulation (modified from Egbert and Kelbert, 2012; Kelbert *et al.*, 2014). The indices i, j and k are used to number the grid point in x,y and z directions, successively. 59

Figure 4.2. The electric and magnetic loops in a staggered grid in discretizing Maxwell's equations (modified from Zhdanov, 2015). 60

Figure 4.3. 3D perspective view displaying vertical north-south slices through the model and site locations (white dots) at surface. The red arrow shows the location of the Kurşunlu hot spring (KHS). The pink asterisks represent hot water wells. Conductive features are labelled with C. . . . 68

Figure 4.4. Resistivity depth sections derived from 3D model for 0.25, 0.5, 1 and 2 km. The white dots show the site locations. The pink asterisks show the location of hot water wells. The red dot marks the location of the KHS. The gray lines mark the GDF, and black lines indicate surface trace of normal faults. Conductive features are labelled with C. Dashed circle (C1) represents reservoir of the KHS. MGBF: Main Graben-Bounding Fault. 69

Figure 4.5. Resistivity distribution with depth along preferred profiles A-A', B-B' and C-C'. The location map of the preferred profiles is shown at the bottom right corner. The location of KHS is shown as red arrow. Red triangles show the location of MT sites. The gray dashed lines mark the GDF, and black lines represent normal faults existing in the study area (modified from Çiftçi and Bozkurt, 2009a; 2009b). Conductive features are labelled with C. 70

Figure 4.6. Measured data (dots) and 3D responses (lines) for two representative sites shown as green dots in the insert. Apparent resistivity and phase derived from off-diagonal (XY and YX) and diagonal (XX and YY) components of impedance tensor. 72

Figure 4.7. Data misfits at each site for four components of the impedance tensor Z_{xx} , Z_{xy} , Z_{yx} , Z_{yy} . MT sites are marked by circles with color representing the nRMS misfit. 73

Figure 4.8. 3D perspective view displaying conductor C through the model and site locations (white dots) at surface. 74

Figure 4.9. Resistivity depth sections derived from 3D model for 0.25, 0.5, 2 and 4 km. The white dots show the site locations. The gray lines mark the GDF, and black lines represent normal faults. Conductive feature is labelled with C. 76

Figure 4.10. Resistivity distribution with depth along preferred profiles A-A', B-B' and C-C'. The location map of the preferred profiles is shown at the bottom right corner. Red triangles show the location of MT sites. The gray lines mark the GDF, and black lines represent normal faults existing in the study area (modified from Çiftçi and Bozkurt, 2009b). Conductive feature is labelled with C. 77

Figure 4.11. Measured data (dots) and 3D responses (lines) for two representative sites shown as green dots in the insert. Apparent resistivity and phase derived from off-diagonal (XY and YX) and diagonal (XX and YY) components of impedance tensor. 78

Figure 4.12. Data misfits at each site for four components of the impedance tensor (Z_{xx} , Z_{xy} , Z_{yx} , Z_{yy}). MT sites are marked by circles with color representing the nRMS misfit. 79

Figure 4.13.	3D perspective view displaying conductor C through the model and site locations (white dots) at surface. Conductive layer is labelled with C.	80
Figure 4.14.	Resistivity depth sections derived from 3D model for 0.25, 0.5, 1 and 3 km. The white dots show the site locations. The black lines indicate surface trace of normal faults. Conductive features are labelled with C. MGBF: Main Graben-Bounding Fault, NMBF: Northern Margin Bounding Fault.	82
Figure 4.15.	Resistivity distribution with depth along preferred profiles A-A', B-B' and C-C'. The location map of the preferred profiles is shown at the bottom right corner. Red triangles show the location of MT sites. The black lines represent normal faults existing in the study area (modified from Çiftçi and Bozkurt, 2009a; 2009b). Conductive features are labelled with C.	83
Figure 4.16.	Measured data (dots) and 3D responses (lines) for two representative sites shown as green dots in the insert. Apparent resistivity and phase derived from off-diagonal (XY and YX) and diagonal (XX and YY) components of impedance tensor.	85
Figure 4.17.	Data misfits at each site for four components of the impedance tensor (Z_{xx} , Z_{xy} , Z_{yx} , Z_{yy}). MT sites are marked by circles with color representing the nRMS misfit.	86
Figure 4.18.	3D perspective view displaying conductors C1 and C2 through the model and site locations (white dots) at surface. The red arrow shows the location of the Veli Çeşmesi hot spring (VHS). Conductive features are labelled with C.	87

- Figure 4.19. Resistivity depth sections derived from 3D model for 0.25, 0.5, 1 and 3 km. The white dots show the site locations. The red dot marks the location of the VHS. The gray lines mark the GDF, and black lines represent normal faults. Conductive features are labelled with C. MGBF: Main Graben-Bounding Fault, NMBF: Northern Margin Bounding Fault. 89
- Figure 4.20. Resistivity distribution with depth along preferred profiles A-A', B-B' and C-C'. The location map of the preferred profiles is shown at the bottom right corner. Red triangles show the location of MT sites. The gray lines mark the GDF, and black lines represent normal faults existing in the study area (modified from Çiftçi and Bozkurt, 2009a; 2009b). Conductive features are labelled with C. 90
- Figure 4.21. Measured data (dots) and 3D responses (lines) for two representative sites shown as green dots in the insert. Apparent resistivity and phase derived from off-diagonal (XY and YX) and diagonal (XX and YY) components of impedance tensor. 91
- Figure 4.22. Data misfits at each site for four components of the impedance tensor (Z_{xx} , Z_{xy} , Z_{yx} , Z_{yy}). MT sites are marked by circles with color representing the nRMS misfit. 92
- Figure 5.1. Sensitivity tests of the 3D inversion model obtained from Area A. (a) Schematic illustration of the tested 3D model together with modifications. The depth and cross sections with resistivity value of replacing blocks are shown in the corresponding model. (b) Comparison between responses of preferred inversion and tested models. 95
- Figure 5.2. Sensitivity test of the 3D inversion model obtained from Area A. (a) Schematic illustration of the tested 3D model together with

	modifications. The depth and cross sections with resistivity value of replacing blocks are shown in the corresponding model. (b) Comparison between responses of preferred inversion and tested models.	96
Figure 5.3.	Sensitivity test of the 3D inversion model obtained from Area B. (a) Schematic illustration of the tested 3D model together with modifications. The depth and cross sections with resistivity value of replacing blocks are shown in the corresponding model. (b) Comparison between responses of preferred inversion and tested model.	98
Figure 5.4.	Sensitivity tests of the 3D inversion model obtained from Area C. (a) Schematic illustration of the tested 3D model together with modifications. The depth and cross sections with resistivity value of replacing blocks are shown in the corresponding model. (b) Comparison between responses of preferred inversion and tested models.	100
Figure 5.5.	Sensitivity test of the 3D inversion model obtained from Area D. (a) Schematic illustration of the tested 3D model together with modifications. The depth and cross sections with resistivity value of replacing blocks are shown in the corresponding model. (b) Comparison between responses of preferred inversion and tested model.	102
Figure 5.6.	Synthetic geoelectric model mimics the geoelectric model obtained from the investigation area A. The model is composed of three zones having different resistivity values, namely an alteration zone with an electrical resistivity of 10 Ωm , a relatively conductive zone (30 Ωm) and a highly resistive basement (300 Ωm). The white dots represent the site locations chosen as similar to the locations of sites existing	

- in area A. The red line shows the location of the SE-NW cross section. 104
- Figure 5.7. 3D inversion results of the test model. The model obtained by inverting full impedance tensor components. The starting model was a homogenous half-space of 100 Ωm , and the error floor were set as 5% value of $|Z_{xy}Z_{yx}|^{1/2}$. The total RMS misfit of 0.93 were achieved after 95 iterations. The white dots represent the site locations, and the red line marks the location of the SE-NW cross section. 105
- Figure 5.8. Synthetic geoelectric model mimics the geoelectric model obtained from the investigation area B. The model is composed of four zones having different resistivity values, namely a conductive zone with an electrical resistivity of 10 Ωm , a relatively conductive zone (30 Ωm) and two resistive zones (250 and 500 Ωm). The white dots represent the site locations chosen as similar to the locations of sites existing in area B. The red line shows the location of the SW-NE cross section. 107
- Figure 5.9. 3D inversion results of the test model. The model obtained by inverting full impedance tensor components. The starting model was a homogenous half-space of 100 Ωm , and the error floor were set as 5% value of $|Z_{xy}Z_{yx}|^{1/2}$. The total RMS misfit of 0.96 were achieved after 23 iterations. The white dots represent the site locations, and the red line marks the location of the SW-NE cross section. 108
- Figure 5.10. Synthetic geoelectric model mimics the geoelectric model obtained from the investigation area C. The model is composed of four zones having different resistivity values, namely a resistive zone (500 Ωm), conductive zone (20 Ωm) and a zone of 100 Ωm and 250 Ωm . The

white dots the site locations chosen as similar to the locations of sites existing in area C. The red line shows the location of the SW-NE cross section. 110

Figure 5.11. 3D inversion results of the test model. The model obtained by inverting full impedance tensor components. The starting model was a homogenous half-space of 100 Ωm, and the error floor were set as 5% value of $|Z_{xy}Z_{yx}|^{1/2}$. The total RMS misfit of 0.97 were achieved after 18 iterations. The white dots represent the site locations, and the red line marks the location of the SW-NE cross section. 111

Figure 5.12. Synthetic geoelectric model mimics the geoelectric model obtained from the investigation area B. The model is composed of three zones having different resistivity values, namely a shallow conductive zone (20 Ωm), a resistive zone (250 Ωm) and a deep conductive zone (30 Ωm). The white dots represent the site locations chosen as similar to the locations of sites existing in area D. The red line shows the location of the S-N cross section. 113

Figure 5.13. 3D inversion results of the test model. The model obtained by inverting full impedance tensor components. The starting model was a homogenous half-space of 100 Ωm, and the error floor were set as 5% value of $|Z_{xy}Z_{yx}|^{1/2}$. The total RMS misfit of 1.0 were achieved after 18 iterations. The white dots represent the site locations, and the red line marks the location of the S-N cross section. 114

Figure 6.1. Cross section derived from the preferred 3D inverse model and the corresponding interpretation for Area A. The location map of the preferred profile is shown at the bottom right corner. The dashed white line corresponds to the area with a resistivity lower than 10 Ωm, which

- has been attributed to the hydrothermal alteration of clay minerals. Solid black lines indicate normal faults, and dashed black lines mark the interpreted faults. The dashed gray line marks the GDF. The blue and red arrows deduce flows of cold and geothermal fluids. The partial transparent gray line indicates production well (SAN-3). 118
- Figure 6.2. Cross section derived from the preferred 3D inverse model and the corresponding interpretation for Area B. The location map of the preferred profile is shown at the bottom right corner. Solid black lines indicate normal faults. GF: Girelli segment of the GDF. 120
- Figure 6.3. Cross section derived from the preferred 3D inverse model and the corresponding interpretation for Area C. The location map of the preferred profile is shown at the bottom right corner. The dashed white line corresponds to the area representing undulating graben floor, which has been associated with the sedimentary fill of the Gediz Graben. Solid black lines indicate normal faults, and dashed black lines mark the interpreted faults. 122
- Figure 6.4. Cross section derived from the preferred 3D inverse model and the corresponding interpretation for Area D. The location map of the preferred profile is shown at the bottom right corner. The dashed white line corresponds to the area with a resistivity lower than 30 Ωm , which has been attributed to shallow sediments of the Gediz Graben. Solid black lines indicate normal faults, and dashed black lines mark the interpreted faults. The dashed gray line marks the GDF. 124
- Figure A.1. The histograms showing the skew angles at each investigation area, area A (a), B (b), C (c) and D (d). 148
- Figure B.1. A schematic view of the 3D model used for the inversion in investigation area A. X- and Y-axes denote N-S and E-W directions,

	respectively. Z-axis is downwards. The MT sites are located at the center of the grid.	148
Figure B.2.	A schematic view of the 3D model used for the inversion in investigation area B. X- and Y-axes denote N-S and E-W directions, respectively. Z-axis is downwards. The MT sites are located at the center of the grid.	148
Figure B.3.	A schematic view of the 3D model used for the inversion in investigation area C. X- and Y-axes denote N-S and E-W directions, respectively. Z-axis is downwards. The MT sites are located at the center of the grid.	149
Figure B.4.	A schematic view of the 3D model used for the inversion in investigation area D. X- and Y-axes denote N-S and E-W directions, respectively. Z-axis is downwards. The MT sites are located at the center of the grid.	149
Figure C.1.	Data fits presented as nRMS at each investigation area (A, B, C and D) for full impedance tensor (\mathbf{Z}).	149

LIST OF SYMBOLS

a	Porosity constant
\mathbf{A}	Any vector field
\mathbf{b}	Boundary condition vector
\mathbf{B}	Magnetic induction
\mathbf{C}	Discrete approximation of the curl of cell edge vectors
\mathbf{C}^\dagger	Discrete approximation of the curl of cell face vectors
\mathbf{C}_d	Data covariance matrix
\mathbf{C}_m	Model covariance matrix
\mathbf{d}	Data vector
\mathbf{D}	Electrical displacement
\mathbf{D}_s	Coefficient matrix (for the first variations of the EM fields)
\mathbf{D}'	Distortion matrix
\mathbf{e}	A typical element of finite-dimensional cell edge vector fields
ϵ	Error
\mathbf{E}	Electric field
\mathbf{f}	Forward operator
G_σ	Green's function
\mathbf{h}	A typical element of finite-dimensional cell face vector fields
\mathbf{H}	Magnetic intensity
I	Current
\mathbf{J}	Current density
\mathbf{J}	Jacobian matrix
k	Wave number
K	Clay mineral constant
m_c	Cementation exponent
\mathbf{m}	Model parameter vector
\mathbf{M}	Magnetotelluric tensor
\mathbf{n}	Unit normal vector

p	Consolidation constant
q	Electric charge
\mathbf{r}	Data residual
R	Boltzman's constant
R_x^*, R_y^*	Complex conjugate EM fields
\mathbf{S}_m	Discrete forward operator
S_w	Water saturation proportion
\mathbf{t}	Unit tangent vector
T	Period
U	Scalar potential
\mathbf{V}	Diagonal matrix of integration volume elements
W	Scalar potential
x	Distance
\mathbf{X}	Real part of the impedance tensor
\mathbf{Y}	Imaginary part of the impedance tensor
z	Depth
\mathbf{Z}	Impedance tensor
α	Non-invariant angle
β	Skew angle
Γ	Proportion of clay minerals
δ_d	Skin depth
ΔV	Potential difference
ε	Electrical permittivity
ϵ	Activation energy
μ	Magnetic permeability
μ	Diagonal matrix of magnetic permeability
ρ	Electrical resistivity
ρ_w	Pore fluid resistivity
σ	Electrical conductivity
σ	Diagonal matrix of electric conductivity
ζ	Any scalar

δ	Dirac delta-function
\mathcal{Z}	Reminder function
τ	Temperature
ν	Trade-off parameter
ψ	Function of an element of finite-dimensional cell edge vector fields
φ	Porosity
ϕ	Phase
Φ	Phase tensor
θ	Penalty function
ω	Angular frequency

LIST OF ACRONYMS/ABBREVIATIONS

1D	One-dimensional
2D	Two-dimensional
3D	Three-dimensional
AEP	Aegean Extensional Province
ADU	Analog/Digital Signal Conditioning Unit
B MDF	Büyük Menderes Detachment Fault
BMG	Büyük Menderes Graben
CMM	Central Menderes Massif
DSFZ	Dead Sea Fault Zone
EA FZ	East Anatolian Fault Zone
EM	Electromagnetic
emf	Electromotive force
GDF	Gediz Detachment Fault
GG	Gediz Graben
GPS	Global Positioning System
KMG	Küçük Menderes Graben
KHS	Kurşunlu hot spring
MGBF	Main Graben-Bounding Fault
MPI	Message Passing Interface
MT	Magnetotellurics
NAFZ	North Anatolian Fault Zone
NEAFZ	North East Anatolian Fault Zone
NLCG	Non-linear conjugate gradients
NMBF	Northern Margin Bounding Fault
NMM	Northern Menderes Massif
RMS	Root Mean Square
RR	Remote Reference
SMM	Southern Menderes Massif
SG	Simav Graben

SDF	Simav Detachment Fault
SRTM	Shuttle Radar Topography Mission
TE	Transverse electric
TM	Transverse magnetic
VHS	Veli Çeşmesi hot spring

1. INTRODUCTION

A geothermal system can be described as a specific area where portions of the thermal energy in the crust of the Earth is localized. The thermal energy, known as geothermal energy, can be used directly such as agricultural heating or indirectly such as electric power generation (Williams *et al.*, 2011). The electrical and electromagnetic (EM) methods are one of the most powerful tools for investigating and deciphering such systems, namely, geothermal reservoirs. Among various EM methods, the magnetotelluric (MT) method is mostly utilized for geothermal exploration worldwide (Uchida *et al.*, 2002; Munoz, 2014; Patro; 2017).

The MT method is the only EM technique that is utilized to reach reliable depths greater than several kilometers required for some geothermal systems (Uchida, 1995; Munoz, 2014), and since 1970s, it has been widely used in geothermal areas in order to investigate structural properties, current state and evaluation of geothermal systems, and hydrothermal circulation of fluids (Lubimova *et al.*, 1972; Berktold, 1983; Ogawa *et al.*, 1998; Uchida and Sasaki, 2006; Harinarayana *et al.*, 2006; Heise *et al.*, 2008, 2016; Newman *et al.*, 2008; Aizawa *et al.*, 2009; Bertrand *et al.*, 2012). Many of those studies have revealed conductive structures associated with circulation of hydrothermal fluids, alteration zones (clay cap) and/or partial melting (Jones and Dumas, 1993; Harinarayana *et al.*, 2004, 2006; Arango *et al.*, 2009; Arnason *et al.*, 2010; Oskooi and Manzella, 2011).

The MT method have testified to be very successful for characterizing geothermal targets in many geothermal areas (Uchida, 1995; Chiang *et al.*, 2015; Zhang *et al.*, 2015). A typical resistivity structure of a geothermal system is defined by the following two properties: (i) a reservoir zone generally having higher conductivity values than the surrounding non-geothermal areas because of exhibiting higher temperatures than the host rocks and (ii) the highest conductivity values often associated with the low temperature clay minerals (cap layer). A high temperature water circulation also takes place beneath the cap layer. However, the resistivity structures in geothermal systems are not always simple and

change among geothermal fields, and thus, detailed investigations at such fields are necessary for appropriate interpretations (Uchida, 1995; Uchida *et al.*, 2002; Munoz, 2014).

Geothermal settings generally consist of a system of faults and/or fractures filled with conducting geothermal fluids and altered rocks. These systems may contain high concentrations of dissolved salts, resulting in conducting electrolyte solutions in a rock matrix depending on temperatures (Munoz, 2014). However, in such systems, the high conductivity structures in general correspond to the clay mineral alteration zones resulting from the hydrothermal processes, and typically locating around the geothermal reservoirs (Pellerin *et al.*, 1996; Munoz, 2014; Patro, 2017).

In active geothermal systems, both fluid and bulk electrical conductivities are strongly controlled by temperature. The bulk electrical conductivity of the geothermal reservoir rocks is also dominated by alteration mineral type, fluid conductivity and porosity (Caldwell *et al.*, 1986). On the other hand, the type of rock, water composition, permeability, temperature and the age of the system controls the hydrothermal alteration (Browne, 1978; Ussher *et al.*, 2000). The prevalent rock alteration minerals having high electrical conductivity are smectite and smectite-illite clays which are hydrothermally altered at shallow depths since hydrothermal processes taking place above the geothermal reservoirs and typically existing at low temperatures (< 150 °C) (Browne, 1978; Munoz, 2014). These anomalously conductive zones (< 10 Ω m) are the active components of the geothermal settings, and it is easy to detect these conductive coats by utilizing significant conductivity contrasts existing in geothermal areas. For this reason, the MT method, which is based on the measurements of electrical resistivities of rock and rock forming minerals, is widely applied in natural resource explorations in geothermal areas.

The 3D MT investigation of geothermal fields is a powerful tool when specifying the deep electrical resistivity structure of geothermal reservoirs since its sensitivity to conductivity contrast and large penetration capability. Extensive 3D modeling of MT data clearly illustrates the geometry of geothermal reservoirs (Heise *et al.*, 2016; Uchida, 2010; Lee *et al.*, 2010; Bertrand *et al.*, 2012, 2013, 2015; Pina-Varas *et al.*, 2014; Chang *et al.*, 2014; Niasari, 2015a; 2015b; Erdođan and Candansayar, 2017), which is important for the

drillings performed by the priori information related to the position and structure of the reservoir rocks (Patro, 2017) and obtaining conceptual geoelectric models of the geothermal systems.

The western Anatolia, hosting a number of geothermal systems is one of the most rapidly deforming continental regions in the world. Recent north-south extensional tectonics, as a result of the northward movement of the Arabian plate and the westward movement of the Anatolian plate, results in high heat flow and seismicity, many active geothermal systems, several grabens and horsts, and normal faults throughout western Anatolia. In the area, faults bounding the grabens lead to the deep circulation and heating of the fluids, which means that the geothermal systems exist along the edges of the grabens in this tectonically active region.

In western Anatolia, the largest regional heat flow anomalies are observed in the Menderes Metamorphic Massif (MMM), and several grabens, which are medium-to-high enthalpy (120-240 °C) systems, have formed within this massif (Serpen *et al.*, 2009). Among these grabens, Gediz graben is one of the most significant geothermal areas, and its structural and tectonic properties, and geothermal energy potential have been studied in detail (Seyitoğlu and Scott, 1996; Cohen *et al.*, 1995; Koçyiğit *et al.*, 1999; Bozkurt and Sözbilir, 2004; Serpen *et al.*, 2009; Oner and Dilek, 2013; Erdoğan and Candansayar, 2017). Although many geothermal exploration projects, which are based on geoelectric surveys, particularly MT measurements, in the main grabens of the western Anatolia have recently been completed or are presently being developed due to the geothermal resource potential of the region, these studies are generally of industry standard, and the results of them are restricted because of exploration license policies. Therefore, the main objective of this study is to provide the most comprehensive understanding about the geothermal systems situated in the Gediz Graben, specifically about the reservoir types, heat sources and structural controls. By utilizing the MT results, it is aimed to understand the structural properties and heat sources of the different types of reservoirs in a more comprehensive way. To accomplish this goal, we applied an inversion process by constructing 3D conceptual models including topography.

The current study highlights the significance of the MT method when detecting and characterizing geothermal systems in geothermal areas, especially in areas where extensional tectonics exists, and it has been successfully applied in the Gediz Graben, western Anatolia. The thesis includes six chapters. The magnetotelluric method in geothermal exploration are introduced in the following chapter. The essential information on the tectonic and geologic settings of the study area, and the acquisition, processing and analyzing of the Gediz Graben data set are explained in Chapter 3. The modeling of the MT data and the results of the 3D inversions of the data set are presented in Chapter 4. In order to test the validity and dimensions of the striking conductive features demonstrated in 3D models for four different areas (A, B, C and D) of the Gediz Graben, a set of tests, which are conducted against the 3D resistivity models in addition to multiple inversion runs including a range of starting models, grid discretization, data weighting and smoothing parameters, are given in Chapter 5. The results of the 3D models are interpreted in Chapter 6 in order to contribute to the understanding of the reservoir types, heat sources and structural controls of the geothermal fields located in the graben, and finally, the results are briefly summarized in Chapter 7. The joint interpretation of the findings reached in this study together with other geological, geophysical and hydrogeological information provides a better understand of the internal structure of geothermal systems existing in the Gediz Graben.

2. MAGNETOTELLURIC METHOD IN GEOTHERMAL EXPLORATION

2.1. Geothermal Systems Overview

A geothermal system is essentially composed of three components, a reservoir, a heat source and a fluid, and it stores natural heat in rocks and fluids within the Earth's crust (Munoz, 2014; Patro, 2017). Figure 2.1 displays a schematic representation of an ideal geothermal system. These systems can be classified in terms of their temperatures and the nature of the reservoirs. According to the heat sources associated with magmatic intrusion ($>600\text{ }^{\circ}\text{C}$) at shallow part of the crust (5-10 km) or naturally increasing temperatures of the Earth, they are characterized as magmatic and non-magmatic geothermal systems. Magmatic geothermal systems involve steam or water dominated convective hydrothermal fluids, hot-dry rocks and partial melts whereas non-magmatic (non-volcanic) systems are generally attributed to hot fluids existing in crystalline or sedimentary reservoirs (Meju, 2002; Munoz, 2014; Patro, 2017).

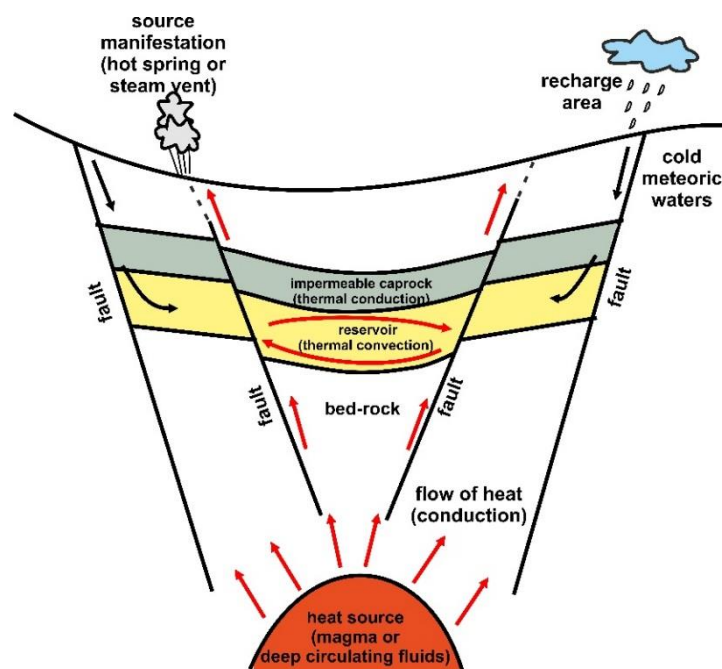


Figure 2.1. A representative model of an ideal geothermal system (modified from Berktold, 1983 and geothermal-energy.org).

The fluids, mostly meteoric water, can be found in the liquid or vapor phase in geothermal systems, which depends on the temperature and pressure conditions of the reservoirs (Patro, 2017). In magmatic geothermal systems, magmatic intrusion heats up the water in reservoir rocks that are bounded by impermeable rocks or generally faults, and these geothermal fluids transport the thermal energy from the deep to the near surface via permeable faults. On the other hand, in non-magmatic systems, meteoric water is heated up by a deep hot water circulation in contact with a heat source (Berkthold, 1983; Tamanyu and Sakaguchi, 2003; Munoz, 2014).

The geothermal systems can also be subdivided into three divisions depending on the enthalpy of geothermal fluids that characterizes the energy content of the fluids and their potential forms of utilization, which are low, medium and high enthalpy resources (Patro, 2017). The high enthalpy geothermal systems (magmatic source) are described as geothermal systems with temperatures above 150-225 °C (e.g., Muffler and Cataldi, 1978; Hochstein, 1990). These systems are generally situated in tectonically active regions such as plate boundaries or in young volcanic regions since the total thermodynamic energy in such regions is sufficient to produce these high temperatures (Munoz, 2014). The geothermal processes in high enthalpy geothermal systems generally result in the generation of extensive clay mineral (smectite, illite) alterations, and the electrical resistivity structure describes a highly conductive clay cap ($< 10 \Omega\text{m}$) overlying a relatively less conductive reservoir (Patro, 2017) (Figure 2.2). The low enthalpy geothermal systems (non-magmatic source) can be defined as geothermal systems with hot fluids in sedimentary or crystalline reservoirs (aquifers), and the natural permeability of reservoirs controlled through faults and fractures can be enhanced through additional stimulation of fluid pathways (Munoz, 2014; Patro, 2017). In such systems, the principle aim is to image high conductivity anomalies correlated with hot water aquifer zones describing reservoirs. However, it is difficult to describe a generalized conceptual model covering the whole range of low enthalpy geothermal systems since the structural, lithological and compositional properties in such systems show a wide range of variety (Munoz, 2014; Patro, 2017).

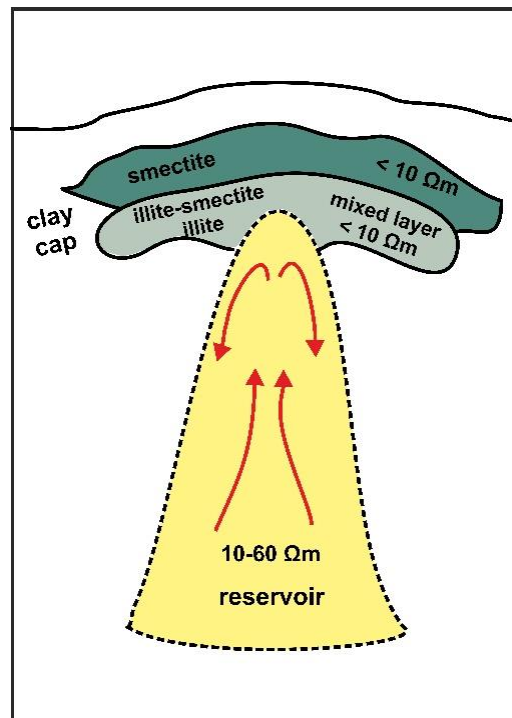


Figure 2.2. Conceptual model of a geothermal system (modified from Pellerin *et al.*, 1996).

Another classification can be made by considering volcanism. Volcanic geothermal systems are attributed to volcanic activity in one way or another (Saemundsson, 2009). The heat sources of these systems are magma or hot intrusions associated with volcanos. On the other hand, the heat source for non-volcanic geothermal systems (including low enthalpy systems) might be regional geothermal gradient in sedimentary rocks or deep water circulation along faults (Tamanyu and Sakaguchi, 2003; Saemundsson, 2009; Munoz, 2014). In non-volcanic geothermal systems, conductive anomalies are associated with saline geothermal fluids situated in sedimentary or crystalline reservoirs (Munoz, 2014).

Several researchers have applied MT method in order to characterize high (e.g., Uchida, 2005; Heise *et al.*, 2008; Arnason *et al.*, 2010; Kuyumcu *et al.*, 2011) and low enthalpy (e.g., Harinarayana *et al.*, 2006; Lee *et al.*, 2007; Arango *et al.*, 2009; Niasari *et al.*, 2015a, b) geothermal systems in many regions in the world. Some of these geothermal systems are volcanic such as the Rotokawa geothermal field, Taupo volcanic zone, New Zealand (Heise *et al.*, 2008; 2016) and some of them are non-volcanic such as the Sipoholon geothermal system, Sumatra, Indonesia (Niasari *et al.*, 2015a; 2015b). Exploration for geothermal resources around the world show that the EM methods, particularly the MT

method, have successfully contributed to mapping geothermal systems and development of geothermal resources since the method is able to reveal the typical properties characterizing geothermal systems such as alteration zones by measuring electrical resistivity of rocks.

2.2. Electrical Conductivity of Rocks

The electrical conductivity simply characterizes the ability of a material to pass free electric charges under the influence of an applied field. It ranges over 10 orders of magnitude for rocks and rock-forming minerals of the Earth (Figure 2.3). The variations in the observed conductivities are not only dependent on the types of rocks, but also on the overall physical condition of the medium. The temperature of a medium is the most important parameter that heavily controls the observed conductivities. In addition to temperatures and the compositions of rocks, there are many factors such as partial melting attributed to upwelling at plate boundaries, aqueous fluids, and metallic, carbon or sulfidic content of rocks, dominating bulk conductivities (Chave and Jones, 2012).

The transmission of electrical currents by free charges in rocks and rock forming minerals becomes in three ways: electronic, semi-conduction and electrolytic conduction. Electronic conduction occurs in metallic ore minerals such as magnetite, and the charge carriers in this type of conduction are electrons. Conduction in graphite can be an example of this type of conduction in EM studies. In semi-conduction, a small proportion of the electrons leads to conduction that occurs in poor conductors having few free charge carriers. This type of conduction is controlled in mantle minerals such as olivine. The electrolytic conduction occurs in crustal rocks involving pores and fractures filled with solution containing free ions such as NaCl. In active tectonic regimes, especially in geothermal and volcanic areas, high conductivities can be explained by partial melts acting as an electrolyte (Caldwell *et al.*, 1986; Simpson and Bahr, 2005; Karato and Wang, 2013).

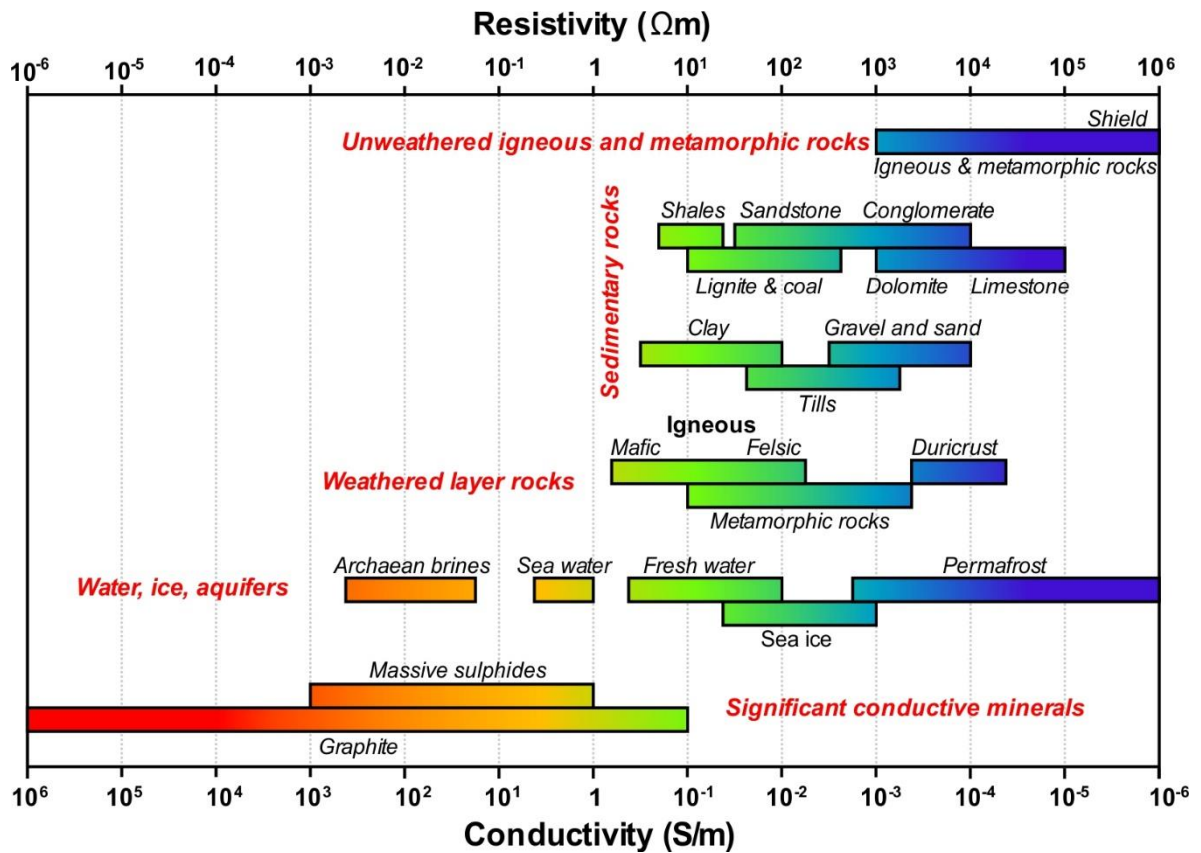


Figure 2.3. Typical electrical conductivity ranges for Earth materials (modified from Palacky, 1987; Marti, 2006 and Miensopust, 2010).

The bulk electrical conductivity of a porous (sedimentary) rock is significantly related to the volume of included fluid and its conductivity and the size and agreement of pores while fluid conductivity is controlled by temperature, concentration of fluid in addition to the mobility and charge of ions (Ritter *et al.*, 2005). The empirical law of Archie (1942) expresses the influence of pore fluid resistivity (ρ_w) on the bulk electrical resistivity of a rock (ρ) which has pores partially filled with brine and remaining voids being filled with oil or gas by the following equation:

$$\rho = a \rho_w \varphi^{-m_c} S_w^{-p} \quad (2.1)$$

where φ is the porosity, and S_w is the water saturation proportion in pores. a and m_c are constants depending on the type of porosity. m_c is called cementation or compaction exponent (Archie, 1942). The value of consolidation constant p is close to 2 for clean unconsolidated and consolidated sands.

In geothermal areas, the alteration minerals, especially clays (smectites-illites), are quite common and they make a considerable contribution to the conductivity of the medium. In that case, Archie's equation will significantly underestimate the bulk electrical resistivity of rocks (Caldwell *et al.*, 1986), and thus, it is modified to include the effect of clay minerals as follows:

$$\rho = a \rho_w \varphi^{-m} S_w^{-p} (1 + K\Gamma\rho_w)^{-1} \quad (2.2)$$

where Γ is the proportion of clay minerals, and K is a constant depends on the type of the clay minerals (Caldwell *et al.*, 1986). Since the number of exchangeable ions strongly affect the conductivity of clay minerals, the value of K changes with the cation exchange capacity, which is high in clay minerals such as smectite and low in minerals such as illite, chlorite and kaolinite (Caldwell *et al.*, 1986).

The high temperatures associated with geothermal activity together with clay mineral alterations and salinity become a significant parameter in geothermal areas. Llera *et al.*, (1990) performed resistivity measurements of water saturated rocks, and showed the correlation between resistivity logs and their measured core resistivities. They suggested that the change of the electrical resistivity of rocks (except granite and crystalline limestone) decreases with increasing temperature up to 200 °C due to increased ionic mobility. However, at temperatures above 200 °C, the electrical resistivity of rocks is controlled by both the saturating solution, fracture characteristics of rocks and by chemical reactions between pore electrolyte and mineral grains (Llera *et al.*, 1990). Ussher *et al.*, (2000) have also suggested that the conductive zones in geothermal areas exhibit a significant correlation with temperatures between 70 and 200 °C, which is associated with clay mineral alterations occurring in this temperature range.

Salinity is the other factor affecting the conductivity in geothermal areas. Increasing fluid salinity results in higher electrical conductivities because of enhanced ion mobility (Ucok *et al.*, 1980). In high salinity reservoirs, high conductivity zones at intermediate temperatures can be considered as hot saline fluids of the geothermal systems, but most

commonly, associated with clay hydrothermal alteration occurring in that temperature (Ussher *et al.*, 2000).

2.3. Basic Theory of the Magnetotelluric Method

The MT method is a natural-source (passive), frequency domain electromagnetic method. This method provides to image the electrical resistivity structure of the Earth from the surface down to the 410 km transition zone and beyond (Chave and Jones, 2012). The frequency range of natural EM signals interested in MT method is from 10^{-4} to 10^4 Hz (Jiracek *et al.*, 1995).

The natural variations in the Earth's magnetic field depend on the frequency of the EM fields. Two mechanisms that operate within distinct frequency regimes produce these variations in the Earth's magnetic field. The EM fields with frequencies lower than 1 Hz are generated by the interaction of the Earth's magnetosphere with the solar winds. When encountering the terrestrial magnetic field (at the magnetopause) with solar wind plasma, positive and negative charged particles are deflected in opposite directions, and therefore generating an electric field. Variations in velocity, density and magnetic field intensity of solar winds give rise to time varying EM fields. The EM fields with frequencies greater than 1 Hz is created by meteorological activity such as lightning discharges. The EM signals generated by worldwide lightning activity travel around the world within a waveguide bounded by the ionosphere and surface of the Earth. In the transition between magnetospheric and ionospheric current systems (between approximately 0.5 and 5 Hz), the intensity of natural EM fields is very low, and this frequency is referred to as the MT dead-band (Simpson and Bahr, 2005; Chave and Jones, 2012).

The MT method provides to measure the time varying EM fields at the surface of the Earth, which is possible in the existence of the Earth's static magnetic field. The time variation of this internal field is small, and it is the external field, which is mentioned above, produces the energy source for MT. The measured time varying fields can be characterized as the total field or vector sum of the primary and secondary fields. The primary fields are created by an external source while the secondary fields are produced by the induced

secondary currents (known as eddy currents) in the conducting ground (Chave and Jones, 2012). When the Earth model is a uniform half-space, then the EM fields follow a regular pattern. However, in inhomogeneous real Earth, this regular pattern is disturbed, and thus secondary fields perturb the total EM fields (Hohmann, 1983). Measuring these perturbed fields at the surface of the Earth gives an insight to describe the resistivity structure of the Earth.

As with almost all electromagnetic methods, MT method is also governed by the fundamental equations of electromagnetic theory, the Maxwell's equations (Tikhonov, 1950; Cagniard, 1953). Maxwell's equations provide to characterize the induction and propagation of EM signals in a magnetisable and polarisable medium without its own electric or magnetic source, and three constitutive equations are also necessary to derive the Maxwell's equations.

As being the first constitutive equation Ohm's law states that the current density \mathbf{J} (A/m^2) is linearly dependent on the external electric field \mathbf{E} (V/m) in many materials, and it constructs a relation between the electric current density \mathbf{J} and the electric field \mathbf{E} by taking electrical conductivity σ (S/m) into account:

$$\mathbf{J} = \sigma \mathbf{E} \quad (2.3)$$

where both \mathbf{E} and \mathbf{J} are vectors, and σ is a second-rank tensor, but in practice, it is often reduced to a scalar value. All nondiagonal elements of the tensor are zero when two of the orthogonal coordinate directions of the tensor are regarded to lie in the direction of the maximum and minimum conductivities. In practice, it is generally reduced to a scalar value (Chave and Jones, 2012).

The second constitutive equation describes the relation between the electric field \mathbf{E} , the electrical displacement \mathbf{D} (C/m^2) and the electrical permittivity ε :

$$\mathbf{D} = \varepsilon \mathbf{E} \quad (2.4)$$

where ϵ is the free-space value ($\epsilon_0 = 8.85 \times 10^{-12} \text{ C}^2/\text{Nm}^2$) of electrical permittivity.

The total current density \mathbf{J} indeed is the sum of the current density of free charges and displacement currents (arising from polarization effects):

$$\mathbf{J} = \sigma \mathbf{E} + \frac{\partial \mathbf{D}}{\partial t} \quad (2.5)$$

where the first term on the right hand side represents diffusion and second is related to displacement currents.

The EM induction is a diffusion process since the second term on the right hand side of Equation 2.4 (the displacement current density) is negligibly small compared with the first term (the conduction current density) (Simpson and Bahr, 2005).

Under the assumption of $e^{i\omega t}$ time dependence, the angular frequency ω , which is given by $\omega = \frac{2\pi}{T}$, is the oscillation frequency of electric field \mathbf{E} , and by utilizing the constitutive Equations 2.3 and 2.4, the limit of assumption can be shown that

$$\sigma \mathbf{E} \gg \frac{d\mathbf{D}}{dt} \Rightarrow 1 \gg \frac{\epsilon \frac{\partial \mathbf{E}}{\partial t}}{\sigma \mathbf{E}} \simeq \frac{\epsilon}{\sigma T} \quad (2.6)$$

and thus, the displacement currents can be ignored when

$$T \gg \frac{\epsilon}{\sigma} \quad (2.7)$$

where T is period of \mathbf{E} .

At very short periods and very low conductivity values, the displacement currents become at least one order of magnitude smaller than the diffusion currents. In MT method, the frequency range of interest is 10^{-4} and 10^4 , and the minimum value of conductivity is 10^{-6} S/m (Figure 2.3), therefore, the assumption of ignoring time varying displacement currents, which is quasi-static approximation, is valid almost all MT data. This makes the EM

induction clearly a pure diffusion process (Kaufman and Keller, 1981; Simpson and Bahr, 2005).

The third constitutive equation characterizes the relation between the magnetic induction \mathbf{B} (Wb/m² or T), the magnetic intensity \mathbf{H} (A/m) by taking the magnetic permeability μ into account:

$$\mathbf{B} = \mu\mathbf{H} \quad (2.8)$$

where μ is the free-space value ($\mu_0 = 4\pi \times 10^{-7}$ H/m) of magnetic permeability. While μ is a second-rank tensor for an anisotropic linear medium, it is a scalar for an isotropic media

Therefore, the Maxwell's equations are given below:

- i. Gauss's Law for the Electric Field: The first law of Maxwell's equations is the Gauss's law for the electric field. This law states that the electric field (or the electric displacement) is generated by free charges. Mathematically, the electric flux through a closed surface of a volume is equal to the electric charges inside the volume, and can be described in differential form (Griffiths, 1999) as

$$\nabla \cdot \mathbf{E} = \frac{q}{\epsilon_0} \quad (2.9)$$

where q (C) is the electric charge.

- ii. Faraday's Law: The second law of Maxwell's equations is the Faraday's law. This law physically means that a changing magnetic field induces an electric field, i.e., time varying magnetic fields induce corresponding changes in the electric field which flows in a closed loop with the axis oriented in the direction of the inducing field, and can be characterized in differential form (Griffiths, 1999) as

$$\nabla \times \mathbf{E} = -\frac{\partial \mathbf{B}}{\partial t} \quad (2.10)$$

- iii. Gauss's Law for the Magnetic Field: The third law of Maxwell's equations is the Gauss's law for the magnetic field. The physical content of this law tells that there are no point sources (no monopoles) for the magnetic field, i.e., there are no free-magnetic charges. Mathematical description of the law is that the total magnetic flux through a closed surface is zero (solenoidal field), and can be expressed in differential form (Griffiths, 1999) as

$$\nabla \cdot \mathbf{B} = 0 \quad (2.11)$$

- iv. Ampere's Law: The fourth law of Maxwell's equation is the Ampere's law. Maxwell added a new term to Ampere's law, which is the displacement currents ($\frac{\partial \mathbf{D}}{\partial t}$) term. The law states that the behavior of time varying magnetic fields depends on the electric current density and time varying displacement currents, i.e., the vector sum of the electric currents and time varying electric fields generates the circulating magnetic fields, and can be defined in differential form (Stratton, 1941) as

$$\nabla \times \mathbf{H} = \mathbf{J} + \frac{\partial \mathbf{D}}{\partial t} \quad (2.12)$$

Each of the fields (primary and secondary) in EM problems must obey Maxwell's equations (Equations 2.9, 2.10, 2.11 and 2.12). These equations represent how EM waves propagate in a uniform media. It is possible to describe the behavior of the EM fields by utilizing the integral forms of the equations, which are derived from Stokes' theorem, at boundaries between the mediums having different electrical properties. Stokes' theorem states can be shown as below (Ward and Hohmann, 1987)

$$\int_S (\nabla \times \mathbf{A}) \cdot \mathbf{n} ds = \oint_C \mathbf{A} \cdot d\mathbf{l} \quad (2.13)$$

where \mathbf{n} is a unit vector normal to the area element ds of the surface S and $d\mathbf{l}$ is a vector element of length along the contour.

Thus, by using Stokes' theorem (Equation 2.13) and assuming that the surface S does not vary with time, Faraday's law (Equation 2.10) and Ampere's law (Equation 2.12) can be written in integral form as follows

$$\oint_C \mathbf{E} \cdot d\mathbf{l} = -\frac{\partial}{\partial t} \int_S \mathbf{B} \cdot \mathbf{n} ds \quad (2.14)$$

and

$$\oint_C \mathbf{H} \cdot d\mathbf{l} = I + \frac{\partial}{\partial t} \int_S \mathbf{D} \cdot \mathbf{n} ds \quad (2.15)$$

in which the current I is defined as

$$I = \int_S \mathbf{J} \cdot \mathbf{n} ds \quad (2.16)$$

Equations 2.14 and 2.15 are the integral forms of Maxwell's two equations, Faraday's and Ampere's laws, respectively.

By utilizing the Divergence or Gauss Theorem,

$$\int_V \nabla \cdot \mathbf{A} dv = \int_S \mathbf{A} \cdot \mathbf{n} ds \quad (2.17)$$

where S denotes a closed surface enclosing the volume V and \mathbf{n} is a unit outward normal. Then, the other two laws (Equations 2.9 and 2.11) of Maxwell can be converted into integral form as follows

$$\oint_S \mathbf{E} \cdot \mathbf{n} ds = \frac{q}{\epsilon_0} \quad (2.18)$$

and

$$\oint_S \mathbf{B} \cdot \mathbf{n} ds = 0 \quad (2.19)$$

Equations 2.18 and 2.19 are the integral forms of Maxwell's two equations, Gauss's law for the electric field and for the magnetic field, respectively.

Considering a boundary between two mediums, 1 and 2, with different electrical properties, $\epsilon_1, \mu_1, \sigma_1$ and $\epsilon_2, \mu_2, \sigma_2$, respectively, the normal \mathbf{n} is positive across the boundary from medium 1 to 2, and the tangent \mathbf{t} is parallel to the boundary (Figure 2.4).

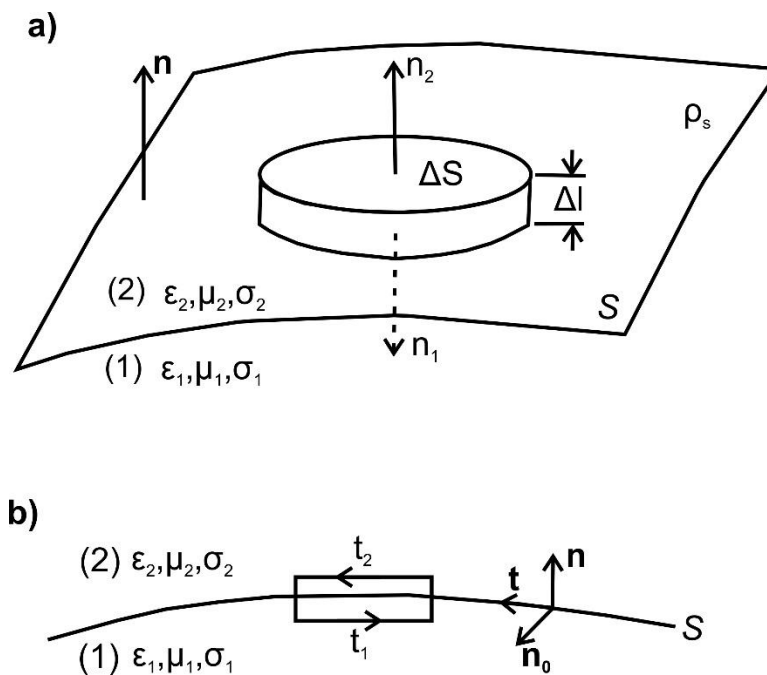


Figure 2.4. Boundary conditions on normal (a) and tangential (b) components of EM fields (modified from Stratton, 1941).

As the superscripts of \mathbf{n} and \mathbf{t} in the next equations represent the normal and tangential components of the fields, successively, the behavior of the field components at a boundary is given as follows (Stratton, 1941; Ward and Hohmann, 1987; Zhdanov, 2015)

The normal component B_n of \mathbf{B} is continuous across an interface separating medium 1 and medium 2, i.e.,

$$B_{n1} = B_{n2} \quad (2.20)$$

The normal component D_n of \mathbf{D} is discontinuous across an interface separating medium 1 and medium 2 owing to the accumulation of a surface charge density ρ_s , i.e.,

$$D_{n2} - D_{n1} = \rho_s \quad (2.21)$$

The tangential components E_t of \mathbf{E} are continuous across an interface separating medium 1 and medium 2, i.e.,

$$E_{t1} = E_{t2} \quad (2.22)$$

The tangential component H_t of \mathbf{H} is continuous across an interface separating medium 1 and medium 2 when there is no surface currents, i.e.,

$$H_{t1} = H_{t2} \quad (2.23)$$

The normal component J_n of \mathbf{J} must be continuous across an interface separating medium 1 and medium 2 when the displacement currents are neglected, i.e.,

$$J_{n1} = J_{n2} \quad (2.24)$$

The scalar potentials W and U described as $\mathbf{E} = -\nabla W$ and $\mathbf{H} = -\nabla U$ for static fields are continuous across an interface, i.e.,

$$W_1 = W_2 \quad (2.25)$$

and

$$U_1 = U_2 \quad (2.26)$$

To obtain equations in the frequency domain, we perform Fourier transform by assuming a plane wave with an $e^{i\omega t}$ harmonic time dependence with frequency ω :

$$\frac{\partial \mathbf{B}(t)}{\partial t} = i\omega \mathbf{B}(\omega) \quad (2.27)$$

Taking the divergence of Equation 2.12 by taking $\nabla \cdot (\nabla \times \mathbf{A}) = 0$ (for any vector field \mathbf{A}) into account gives

$$\nabla \cdot (\nabla \times \mathbf{H}) = \nabla \cdot (\sigma \mathbf{E}) = \sigma \nabla \cdot \mathbf{E} + \mathbf{E} \cdot \nabla \sigma = 0 \quad (2.28)$$

Substituting Gauss's Law for the electric field in Equation 2.28 yields

$$\frac{\rho}{\varepsilon_0} = -\mathbf{E} \cdot \frac{\nabla \sigma}{\sigma} = -\mathbf{E} \nabla \ln \sigma \quad (2.29)$$

Then, we obtain Maxwell's equations in the frequency domain

$$\nabla \times \mathbf{E} = -i\omega \mathbf{B} \quad (2.30)$$

$$\nabla \times \mathbf{B} = \mu_0 \sigma \mathbf{E} \quad (2.31)$$

$$\nabla \cdot \mathbf{E} = -\mathbf{E} \nabla \ln \sigma \quad (2.32)$$

$$\nabla \cdot \mathbf{B} = 0 \quad (2.33)$$

Taking the curl of Equations 2.30 and 2.31, we can derive the diffusion equations in terms of the electric and magnetic fields. For this purpose, we make use of the following two proven vector identities (Simpson and Bahr, 2005)

$$\nabla \times (\nabla \times \mathbf{A}) = \nabla (\nabla \cdot \mathbf{A}) - \nabla^2 \mathbf{A} \quad (2.34)$$

$$\nabla \times (\zeta \mathbf{A}) = \zeta \nabla \times \mathbf{A} - \mathbf{A} \times \nabla \zeta \quad (2.35)$$

where \mathbf{A} and ζ are any vector and scalar, respectively.

Then, the diffusion equation of the electrical field can be written as

$$\nabla_{\mathbf{x}}(\nabla_{\mathbf{x}}\mathbf{E}) = \nabla_{\mathbf{x}}(-i\omega\mathbf{B})$$

$$\nabla(\nabla \cdot \mathbf{E}) - \nabla^2\mathbf{E} = -i\omega(\nabla_{\mathbf{x}}\mathbf{B})$$

$$\nabla^2\mathbf{E} = i\omega\mu_0\sigma\mathbf{E} - \nabla(\mathbf{E}\nabla\ln\sigma) \quad (2.36)$$

The diffusion equation for the magnetic field can also be given as

$$\nabla^2\mathbf{B} = i\omega\mu_0\sigma\mathbf{B} + \mu_0\mathbf{E}\times\nabla\sigma \quad (2.37)$$

By assuming an Earth model for which $\nabla \cdot \mathbf{E} = 0$ (isotropic and homogenous half-space), the conductivity is constant ($\nabla\sigma = 0$). Therefore, the diffusion Equations 2.36 and 2.37 simplify below expressions

$$\nabla^2\mathbf{E} = i\omega\mu_0\sigma\mathbf{E} \quad (2.38)$$

$$\nabla^2\mathbf{B} = i\omega\mu_0\sigma\mathbf{B} \quad (2.39)$$

These equations (Equations 2.38 and 2.39) are second order differential equations with solutions valid for the source geometry is the function of depth only and of the form (Simpson and Bahr, 2005):

$$\mathbf{E} = \mathbf{E}_1e^{i(\omega t - kz)} + \mathbf{E}_2e^{i(\omega t + kz)} \quad (2.40)$$

$$\mathbf{B} = \mathbf{B}_1e^{i(\omega t - kz)} + \mathbf{B}_2e^{i(\omega t + kz)} \quad (2.41)$$

where z is depth.

Since assuming the Earth does not generate EM energy, but only dissipates or absorbs it, the amplitudes of the terms \mathbf{E}_2 and \mathbf{B}_2 should be zero. In a homogenous half-

space (where $\frac{\partial^2 E}{\partial x^2} = \frac{\partial^2 E}{\partial y^2} = 0$), taking the second derivative of the Equation 2.40 and inserting the solution to the Equation 2.38, we then obtain the equation as

$$\nabla^2 \mathbf{E} = \frac{\partial^2 \mathbf{E}}{\partial z^2} = k^2 \mathbf{E}_1 e^{i(\omega t - kz)} = k^2 \mathbf{E} \quad (2.42)$$

Therefore, the Equation 2.38 is reduced to the homogenous Helmholtz equation (Zhdanov, 2015):

$$k^2 \mathbf{E} = i\omega\mu_0\sigma \mathbf{E} \quad (2.43)$$

Thus, the complex wave number k is

$$k = \sqrt{i\omega\mu_0\sigma} = \frac{\pm(1+i)}{\sqrt{2}} \sqrt{\omega\mu_0\sigma} = \pm \left(\sqrt{\frac{\omega\mu_0\sigma}{2}} + i \sqrt{\frac{\omega\mu_0\sigma}{2}} \right) \quad (2.44)$$

The inverse of the real part of k controls the attenuation of EM energy, and its inverse is known as the frequency dependent EM skin depth or penetration depth δ_d :

$$\delta_d = \frac{1}{\text{Re}(k)} = \sqrt{\frac{2}{\omega\mu_0\sigma}} \quad (2.45)$$

It describes the depth at which the intensity of EM field decades to $\frac{1}{e}$ of its original amplitude.

2.4. Transfer Functions of Magnetotelluric Responses

The Earth in MT method is assumed as a linear and time invariant system. In this system, the Earth is termed as a transfer function describing the linear relationship between an input and predictable output (i.e., a linear relationship between the measured EM field components) at a given frequency. Due to the assumption of homogenous earth, the transfer functions are considered independent from the EM source fields. They depend only on the electrical properties of the materials in which the EM signals travels through and thus describe the resistivity distribution of the underlying materials depending on measured frequency (Simpson and Bahr, 2005; Berdichevsky and Dmitriev, 2008). Although there are several description of MT transfer functions, they are commonly represented by the impedance tensor.

2.4.1. The Impedance Tensor

The impedance tensor \mathbf{Z} relates the orthogonal components of the horizontal electric (E_x, E_y) and magnetic (H_x, H_y , or equivalently $B_x/\mu_0, B_y/\mu_0$) fields at a given frequency. This relation can be expressed as (Simpson and Bahr, 2005)

$$\begin{pmatrix} E_x \\ E_y \end{pmatrix} = \begin{pmatrix} Z_{xx} & Z_{xy} \\ Z_{yx} & Z_{yy} \end{pmatrix} \begin{pmatrix} H_x \\ H_y \end{pmatrix} \quad \text{or} \quad \mathbf{E} = \mathbf{ZH} \quad (2.46)$$

where \mathbf{Z} (Ω) is a complex second rank tensor. Each component of it consists of real and imaginary parts, i.e., it has a magnitude and phase.

The general properties of the impedance tensor are directly related to the dimensionality of subsurface medium. While there are some simplifications in the 1D and 2D cases, the impedance tensor in 3D Earth is fully occupied. In that case, all elements of impedance tensor are non-zero, and needed to be computed for each frequency (Ritter *et al.*, 2005).

Since \mathbf{Z} is complex, at a particular frequency, we can write amplitude and phase relation as

$$\rho_a(\omega) = \frac{1}{\mu_0 \omega} |Z(\omega)|^2$$

$$\phi(\omega) = \tan^{-1} \left[\frac{\text{Im}(Z(\omega))}{\text{Re}(Z(\omega))} \right] \quad (2.47)$$

where ρ_a (Ωm) is called the apparent resistivity since it is an average resistivity for a volume sensitive at a given frequency in a half-space, and ϕ (degree) is phase of Z .

3. MAGNETOTELLURIC STUDY OF THE GEDIZ GRABEN GEOTHERMAL FIELDS

3.1. Tectonic and Geologic Settings

3.1.1. Tectonic Setting

Our study area (Gediz Graben) (Figure 3.1), which is a part of the Aegean Extensional Province (AEP), is subjected to an ongoing approximately N-S directed extensional deformation. Five different main models have been suggested to explain the cause and origin of the extension in the region. These models include: back-arc spreading (McKenzie, 1978; Le Pichon and Angelier, 1979; Meulenkamp *et al.*, 1988), tectonic escape (Dewey and Şengör, 1979; Şengör and Yılmaz, 1981; Şengör *et al.*, 1985), orogenic collapse (Dewey, 1988; Seyitoğlu and Scott, 1996), episodic-two stage graben (Koçyiğit *et al.*, 1999; Bozkurt and Sözbilir, 2004) and inconsistent convergence rates (Doglioni *et al.*, 2002). In the back-arc spreading model, back-arc spreading accompanied by southwestward roll-back of the subducting African plate and south-southwestward migration of the Aegean arc is attributed to the continental extension in western Anatolia. In tectonic escape model, the Anatolian plate moved westward along its boundary faults, namely North Anatolian and East Anatolian fault zones (NAFZ and EAFZ), because of the roughly north-south directed collision of the Arabian and Eurasian plates during late Serravalian time (~12 Ma). In the orogenic collapse model, extensional tectonics is associated with spreading and thinning of an overthickened (65-70 km) crust. Gravitational collapse of the crust in this model is commenced by late Oligocene-early Miocene (24-20 Ma) immediately after cessation of the Palaeogene-Eocene shortening and overthickening of the crust during the closure of the northern branch of Neotethys. In the episodic-two stage graben model, continental extension resulted in two extensional stage, an Early-Middle Miocene orogenic collapse and a Plio-Quaternary normal faulting and graben formation due to the westward movement of the Anatolian plate along NAF and EAF, and these two stage were separated by a short phase of N-S crustal shortening during late Serravalian-late Early Pliocene times. More recently, the inconsistent convergence rates in western Anatolia, namely the different convergence

rates between northeastward-directed subduction of the African plate relative to the Anatolia, characterizes the continental extension in the region.

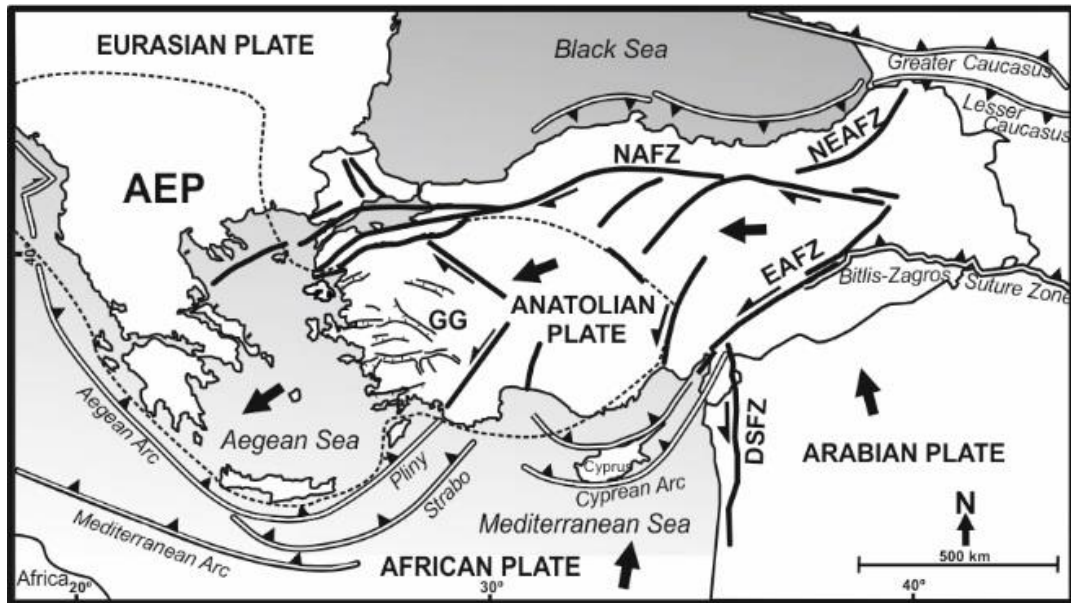


Figure 3.1. Simplified tectonic map of Turkey and surrounding (modified from Barka, 1992; Bozkurt, 2001; Gürer *et al.*, 2006). Dotted line shows the approximate extent of the Aegean Extensional Province (AEP). DSFZ: Dead Sea Fault Zone, EAFZ: East Anatolian Fault Zone, NAFZ: North Anatolian Fault Zone, NEAFZ: North East Anatolian Fault Zone, GG: Gediz Graben.

Although several geodynamic models have been suggested to clarify the genesis and age of the crustal extension in the western Anatolia, in fact, the mechanism of extension is more complex owing to the interplay among different processes. Therefore, a combination of different processes based on above models would be a better explanation in order to describe the nature of the extension. Today, there is no still consensus about timing and origin of the continental extension but no doubt about the occurrence of the continental extension in two distinct stages (Bozkurt and Mittwede, 2005).

3.1.2. Geologic Structure and Stratigraphy

The extensional tectonics in western Anatolia leads to development of horst-graben systems, and the geothermal systems formed along the edges of these grabens (Figure 3.2). While graben basins are filled with Neogene to Recent continental deposits, horst blocks are composed of amalgamated continental fragments of the Anatolian plate. The grabens and intervening horst blocks in the region shows two dominant structural directions, approximately E-W directed grabens and N-S directed basins (Çiftçi and Bozkurt, 2010).

Among several grabens, Gediz Graben, which is also known as Alaşehir or Salihli-Alaşehir graben, is the most prominent and the best developed graben in the western Anatolia (Çiftçi and Bozkurt, 2009b) (Figure 3.2 and 3.3). It was formed above the N-dipping, low angle detachment zone between the early Miocene and the Pleistocene (Oner and Dilek, 2011, 2013). It is a 150 km long, 3-40 km wide, 2-3 km thick, WNW-ESE trending (changing from W-E in the western end to NW-SE direction in its eastern end), asymmetric curvilinear and actively growing graben. It also contains the most seismically active and largest faults along its southern margin (Koçyiğit, 1999; Bozkurt and Sözbilir, 2004; Çiftçi and Bozkurt, 2007, 2009b; Oner and Dilek, 2011, 2013), and experienced numerous earthquakes during the last century (Arpat and Bingöl, 1969; Eyidoğan and Jackson, 1985; Bozkurt, 2003).

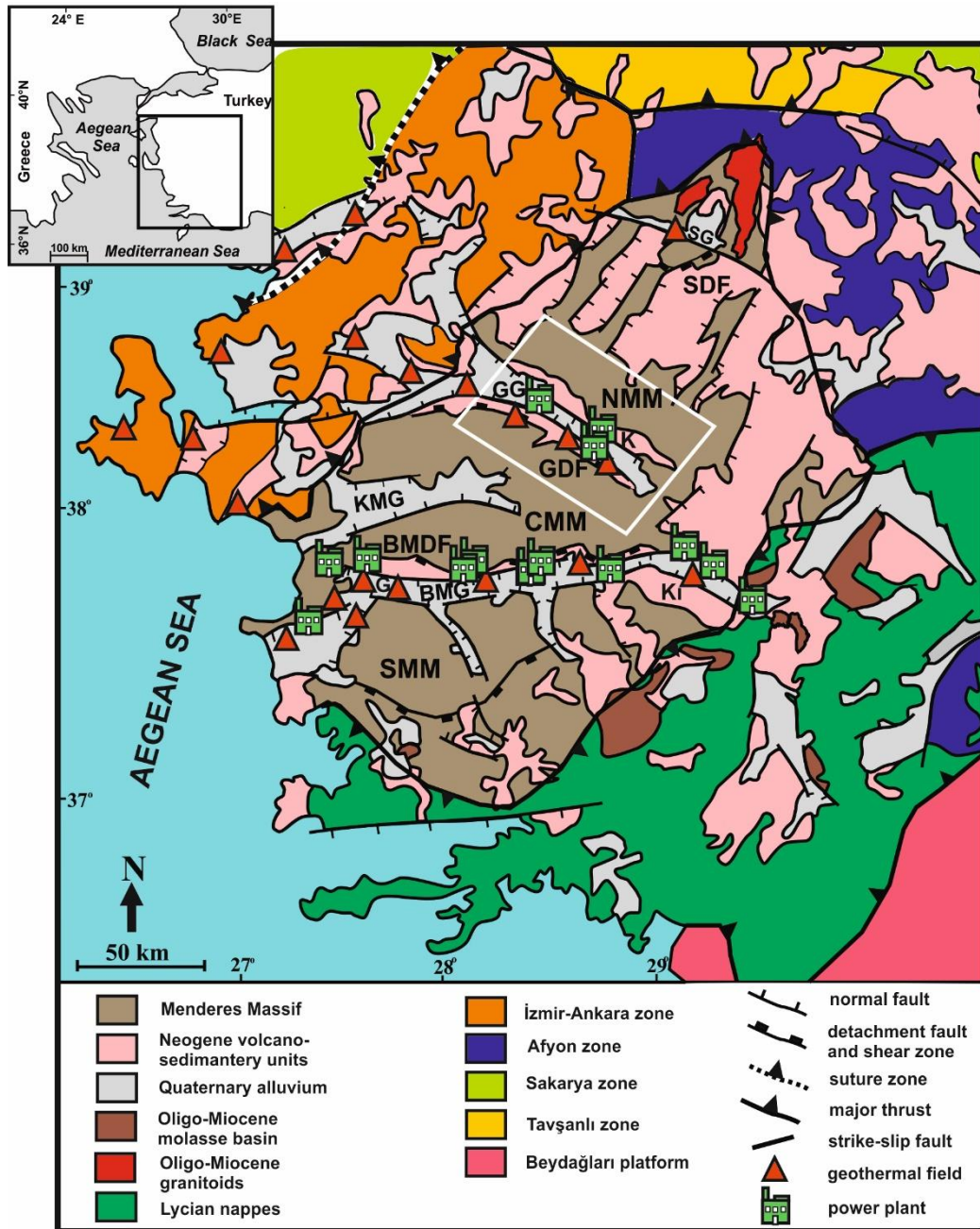


Figure 3.2. Simplified geological map of the western Anatolia showing locations of the Gediz and other major grabens (modified from Sözbilir, 2005; Emre and Sözbilir, 2007; Serpen *et al.*, 2009; Mertoğlu *et al.*, 2015). White box shows the location of study area, Gediz Graben (GG). NMM: Northern Menderes Massif, CMM: Central Menderes Massif, SMM: Southern Menderes Massif, SG: Simav Graben, KMG: Küçük Menderes Graben, BMG: Büyük Menderes Graben, SDF: Simav Detachment Fault, GDF: Gediz Detachment Fault, BMDF: Büyük Menderes Detachment Fault, K: Kavaklıdere, K1: Kızıldere, G: Germencik.

The geothermal fields lying within or along the margins of the Gediz Graben are bounded by normal faults (Figure 3.3). The faults are classified into two groups in terms of their different structural characteristics. These are: (i) large scale, E-W to NW-SE trending, presently low-angle (dip between 0-32°), north dipping and currently inactive normal faults (Gediz detachment fault) situated along the southern margin of the Gediz Graben, and (ii) nearly E-W to WNW-ESE or ENE-WSW trending, high-angle (dip $\geq 40^\circ$), north dipping and seismically active normal faults bounding the southern margin of the graben (Lips *et al.*, 2001; Çiftçi and Bozkurt, 2007, 2009a, b, 2010; Oner and Dilek, 2013).

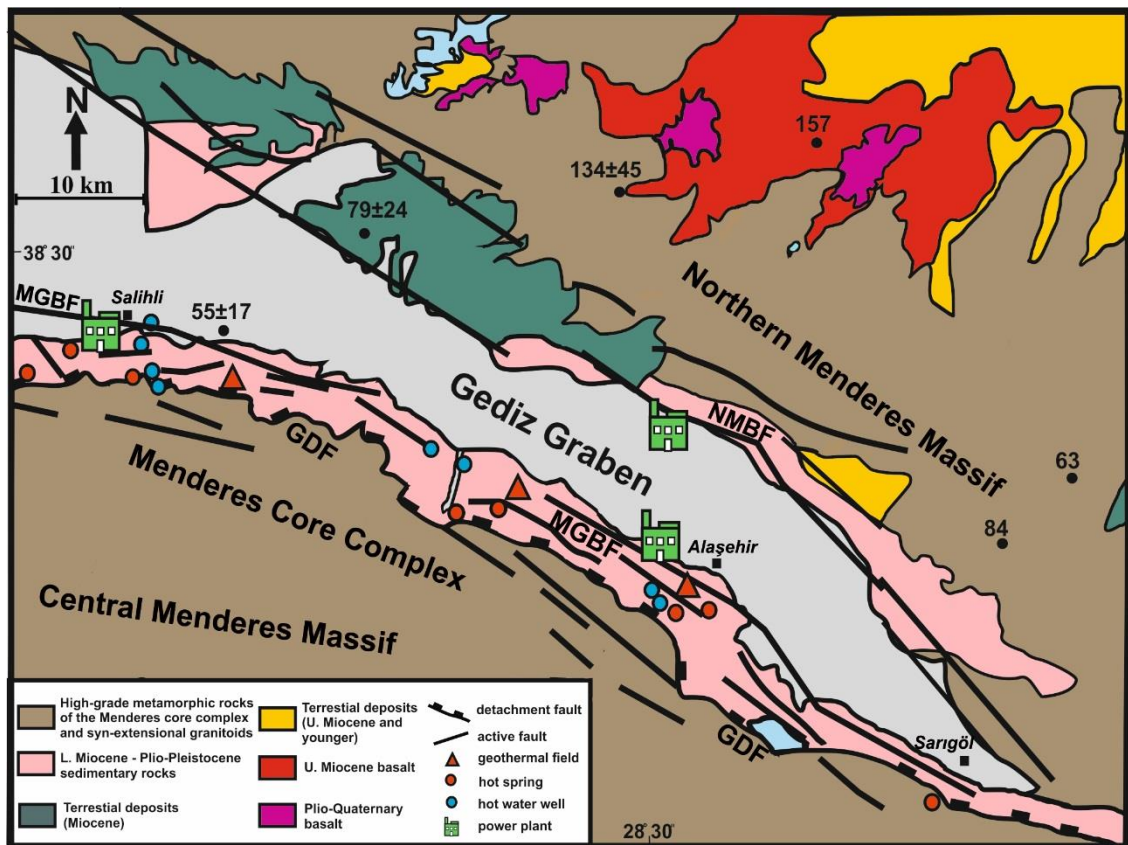


Figure 3.3. Regional tectonic map of the Gediz Graben, showing the faults, location of the geothermal fields, hot springs, hot water wells and power plants (modified from Oner and Dilek, 2013; Serpen *et al.*, 2009; Yılmazzer *et al.*, 2010; Mertoğlu *et al.*, 2015). Regional heat flow values are taken from Erkan (2015). GDF: Gediz Detachment Fault, MGBF: Main Graben-Bounding Fault, NMBF: Northern Margin Bounding Fault.

Figure 3.4 shows a typical metamorphic core complex consists of a core of metamorphic rocks underlying sedimentary rocks in an extensional regime. Similarly, Gediz detachment fault separates high-grade metamorphic rocks of the Menderes Massif (metamorphic core complex) and syn-extensional granites in the footwall from the lower Miocene-Quaternary sediments in the hanging wall (Bozkurt and Sözbilir, 2004; Baba and Sözbilir, 2012; Oner and Dilek, 2013). Figure 3.5 also displays Gediz detachment surface in area B. The high-angle normal faults in the Gediz Graben are observed as either single faults with diverse size (sub-kilometers to tens of kilometers), e.g., the main graben-bounding fault (MGBF) or as fault sets including discontinuous, mostly synthetic and parallel to sub-parallel segments (Çiftçi and Bozkurt, 2007, 2009a), and develop in a graben-facing step-like pattern dominated by first-order major and second-order synthetic to antithetic faults (Bozkurt and Sözbilir, 2004; Çiftçi and Bozkurt, 2007, 2009a). Actively growing travertines, shifting or bending of river courses, hot water springs and ground ruptures of historical and recent earthquakes in the region is a clear evidence of the seismic activity of the high-angle normal faults that controls both the southern and northern margins of the graben (Çiftçi and Bozkurt, 2009a). The active high-angle normal faults within the Gediz Graben play a significant role as being ideal heat flow conduits for the geothermal resources founded in the intersect points of the differently-directed faults (Yılmaz *et al.*, 2010), and the circulation of the thermal waters in geothermal systems is also directly related to these fault zones. Additionally, NNE-SSW trending, dip angles varying between 85° and 60° and west/east dipping oblique-slip scissors (hinge) faults are observed in the Gediz Graben (Oner and Dilek, 2011).

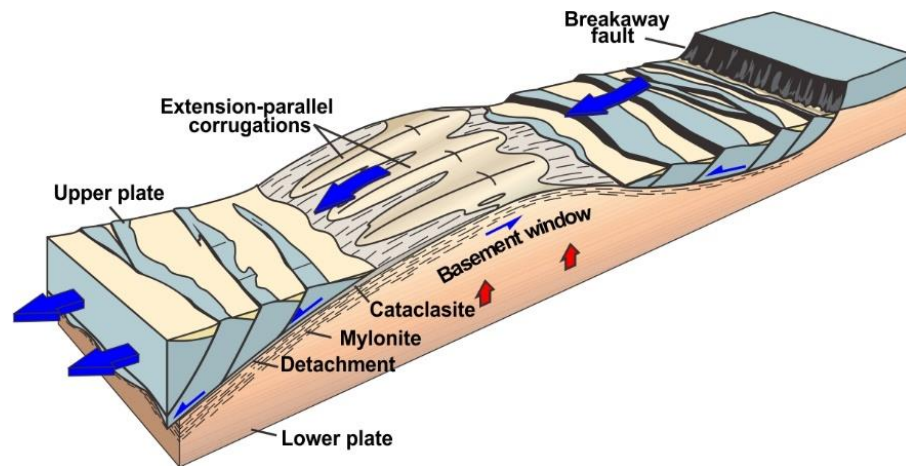


Figure 3.4. A typical metamorphic core complex composed of a core of metamorphic rocks exposed in a window through non-metamorphic rocks, particularly sedimentary rocks (modified from Fossen, 2016).

The lithostratigraphic units representing the Gediz Graben are classified into two groups as being the basement and cover units. Metamorphic rocks of Menderes Massif (e.g., gneiss, mica schists, quartz schists and marble), which are composed of high to low grade metamorphism (Özen *et al.*, 2010), form the Neogene basement that lies underneath the graben-fill, and the Miocene to Recent sedimentary rocks within the graben basin consist of the cover units (Çiftçi and Bozkurt, 2009b) (Figure 3.6). The basement rocks of the Gediz Graben dominantly composed of spotted gneiss at the bottom and various types of schists at the top (Yilmazer *et al.*, 2010). The porosity and permeability of the basement rocks vary in terms of the amount of carbonates that they contain. The basement rocks such as marbles and dolomitic marbles including intense amount of carbonates are highly fractured and act as a reservoir for fluids. The quartz-schist units and fractured gneiss of the basement also act as an aquifer for mineralized and hot waters for Gediz Graben geothermal systems (Özen *et al.*, 2010; Yilmazer *et al.*, 2010). Two sedimentary sequences exist in the Gediz Graben basin strata (Seyitoğlu *et al.*, 2000; Oner and Dilek, 2011, 2013). The Neogene sediments consisting of alluvial-fan deposits containing clay-rich intervals have very low permeability, and thus these units may act as a cap rock for the geothermal systems in the region (Tarcan *et al.*, 2000; Faulds *et al.*, 2009; Yilmazer *et al.*, 2010; Özen *et al.*, 2010).



Figure 3.5. The field photo displaying Gediz detachment surface (photo taken by Ahmet Tuğrul Başokur and the location pointed out by Erdin Bozkurt).

As shown in Figure 3.6, the lowermost and the oldest part of the graben-fill is called the Alaşehir Formation that is composed of two subunits, Zeytinçay and Evrenli members, containing conglomerates, sandstones, siltstones and organic-rich shales. The Çaltılık Formation overlying the Alaşehir formation consists of conglomerates, sand stones and limestone lenses. The Alaşehir Formation is overlain by the Çaltılık Formation comprising two subunits, Hamamdere and Salihli members. These units consist of conglomeratic deposits of an alluvial fan system and sandy deposits of a fluvial system, successively. The Kaletepe Formation overlying the Gediz Formation with an angular unconformity comprises of conglomerates with minor sandstone and mudstone intercalations. The Bintepeleler Formation exposed only along the northern margin of the Gediz Graben is composed of very coarse-grained, texturally immature, chaotic alluvial conglomerates at the base, and stratigraphically upward limestones become dominant in the formation. The uppermost units in the Gediz Graben is Quaternary alluviums composed of fluvial sediments of the modern Gediz River (Çiftçi and Bozkurt, 2009a; Çiftçi and Bozkurt, 2010).

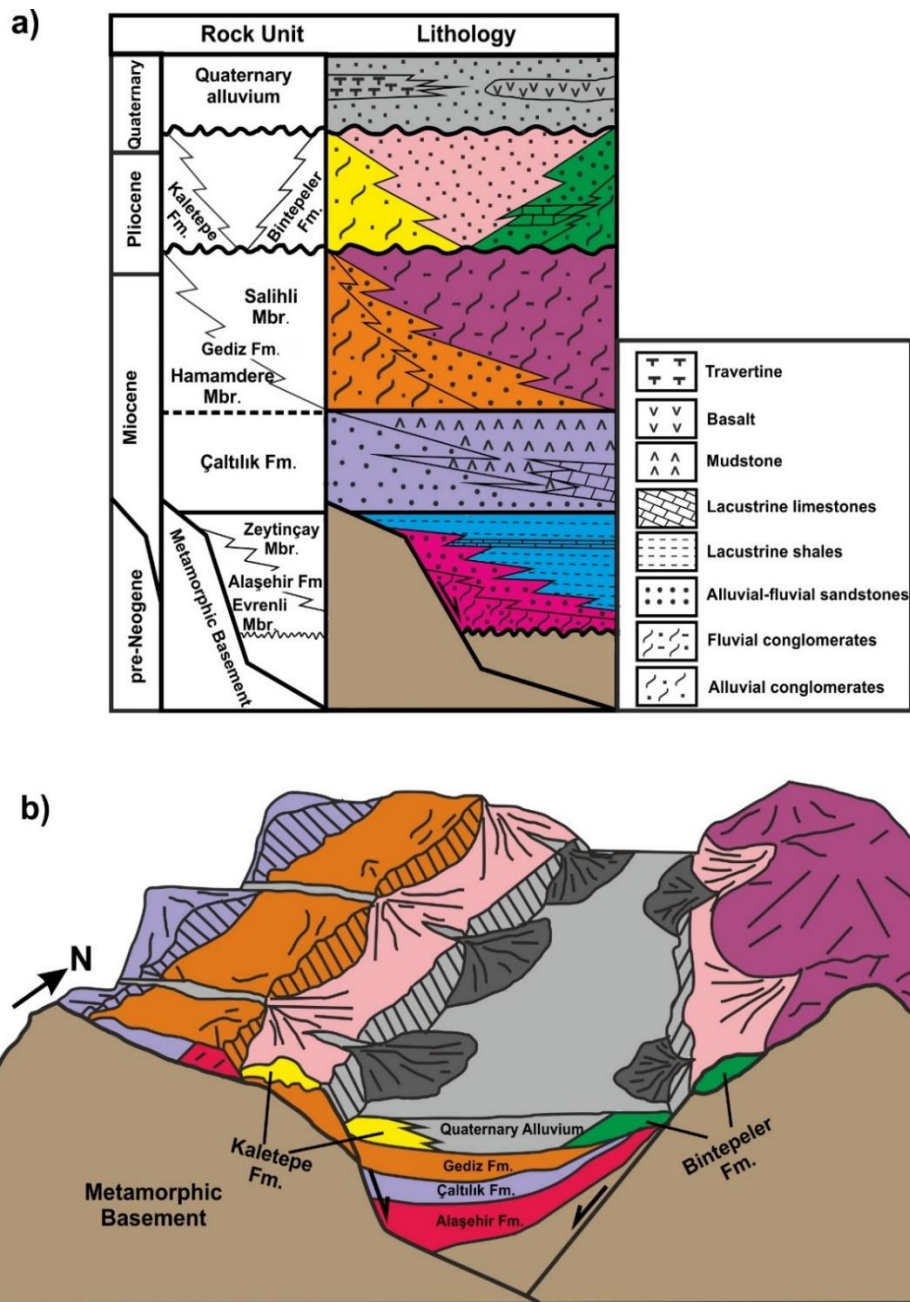


Figure 3.6. Simplified stratigraphic columnar section of the Gediz Graben and its basement (a) and block diagram (b), illustrating the internal structure of the Gediz Graben and Menderes Massif (modified from Çiftçi and Bozkurt, 2009a; 2009b; Oner and Dilek, 2013).

3.1.3. Geothermal Manifestations

Several liquid-dominated low to high enthalpy geothermal systems with aquifer temperatures ranging from 150 to 242 °C exist in the Neogene grabens within the Menderes Massif in western Anatolia (Tarcan, 2005) (Figure 3.2). Kızıldere (242 °C) is the highest temperature geothermal system known in Turkey, and Germencik (232 °C) is the second area having the highest reservoir temperature (Tarcan, 2005; Serpen *et al.*, 2009). These two hottest geothermal fields are respectively located near the eastern and western ends of the Büyük Menderes Graben, and the third high temperature geothermal system Kavaklıdere (182 °C) is located in the Gediz Graben (Figure 3.2). There are also numerous hot springs and fumaroles near these geothermal areas (Faulds *et al.*, 2009).

Geothermal manifestations such as hot springs, fumaroles, travertines and mud pools are the most prominent indications of hot water circulation at depth. In the Gediz Graben, these manifestations are mainly located along the active southern margin of the graben. Geothermal systems, which are Turgutlu-Urganlı, Salihli-Kurşunlu, Caferbeyli and Sart, and Alaşehir-Kavaklıdere geothermal fields (Serpen *et al.*, 2009), and hot springs and hot water wells corresponding to the geothermal systems are situated near the Gediz detachment fault at the intersection of the ~N-S striking faults. As permeable flow channels, these faults bounding geothermal systems provide a suitable condition for deep circulation of fluids.

Salihli geothermal system in the Gediz Graben has a well deep temperature of 155 °C at 1189 m. The maximum temperature in Urganlı geothermal system is 83 °C, and Alaşehir geothermal system has a maximum temperature of 215 °C (Tarcan *et al.*, 2000; Tarcan, 2005; Yilmazer *et al.*, 2010). The depth of geothermal wells drilled in the Gediz Graben varies between 40 and 1507 m (Yilmazer *et al.*, 2010), and the deepest (1507 m) and third high temperature (215 °C at the bottom hole) well in Turkey was drilled in Alaşehir-Kavaklıdere (Yilmazer *et al.*, 2010).

Geothermal fluids in the Gediz Graben is utilized for balneological purposes, district heating and green house heating (Serpen *et al.*, 2009; Mertoğlu *et al.*, 2015). The Alaşehir power plant was also installed at Alaşehir geothermal field for power production (Mertoğlu *et al.*, 2015) (Figure 3.3). Kurşunlu geothermal field in the Gediz Graben is the most

significant area in Turkey owing to district heating (Özen *et al.*, 2010). The total discharge rate at Kurşunlu is 145 l/s for the main producing wells. The discharge rates in the graben are highest at reservoirs predominantly composed of marbles (Faulds *et al.*, 2009).

The other geothermal surface manifestations in the Gediz Graben is travertines. There are several travertine deposits in the Gediz Graben. Travertine is formed by precipitation of carbonate minerals (Wyatt, 1986). Travertines are mostly deposited around thermal springs (Wyatt, 1986), and dominated by active faults existing in the Gediz Graben (Çakır, 1999; Selim and Yanik, 2009).

3.1.4. Existing Geophysical Studies

Western Anatolia is seismically one of the most active regions of continental crust in the world and currently undergoing N-S trending continental extension. The extension rate estimated from Global Positioning System (GPS) measurements is 30 ± 2 mm/yr (McClusky *et al.*, 2000). The surface geology in the region has been widely studied but the deep crustal structure and earthquake activity has been less investigated. With the help of developing a regional network, Akyol *et al.*, (2006) studied region and show that crustal velocities in the western Anatolia are strikingly lower than the average continental values, which is attributed to high temperatures, fluids at high pore pressure or high degree of fracture in the crust. By locating local earthquakes, they also show that peak seismicity in the region occurs at depths of ~10 km.

Saunders *et al.*, (1998) by utilizing seismic waveform data from two temporary arrays in western Anatolia suggested that the crustal thickness beneath the western Anatolia is ~ 30 km. By analyzing teleseismic waveform data, Zhu *et al.*, (2006) proposed a crustal thickness of 28-30 km in the central Menderes Massif, which is thinner than the surrounding regions where crustal thicknesses are 32-34 km. Computing synthetic waveforms of the 21 April 2000 Denizli (Honaz) and the 9 July 1998 Izmir (Doğanbey) earthquakes, Horasan *et al.*, (2002) also suggested an average crustal thickness of 33 km for the region, and Pn and S velocities of 7.85 and 4.53 km/s, successively. A recent study analyzing Pn travel times in

order to define crustal thicknesses also suggests that the crustal thicknesses beneath western Anatolia is between 28 ± 2 and 33 ± 2 km (Mutlu and Karabulut, 2011).

The highest temperature geothermal systems in the western Anatolia have formed along the margins of the approximately E-W trending grabens of the Menderes Massif. These high temperatures are associated with the high heat flow from the basement of the region. İlkışık (1995) utilizing silica geothermometer on hot springs performed a heat flow study, and suggested that the mean value of heat flow for western Anatolia is 107 ± 45 mW/m², which is ~60% higher than the world average. Furthermore, the maximum value of heat flow in the region was obtained from the Gediz and Büyük Menderes Grabens. Dolmaz *et al.*, (2005) suggested a heat flow and Curie point depth map of western Anatolia by analyzing spectrum of aeromagnetic data. The map shows a high heat flow values and shallow Curie point depths for the Gediz Graben. Moreover, a regional heat flow map of Turkey constructed by Akın *et al.*, (2014) also shows that the heat flow values in the Gediz Graben varies between 125 mW/m² and 170 mW/m². In this study, geothermal gradient was estimated from the Curie point depths, which are less than 10 km in the geothermal fields (Aydın *et al.*, 2005), and obtained from airborne magnetic data through power spectrum method. The heat flow values were therefore obtained by multiplying geothermal gradient with thermal conductivities (Akın *et al.*, 2014). Aeromagnetic anomaly map of Turkey prepared from this study also exhibit low magnetic anomalies in the western Anatolia. Erkan (2015) using equilibrium temperatures from shallow (~100 m) boreholes in western Anatolia generated a heat flow map of the region. In this study, it is resulted that the central part of the Menderes Massif shows elevated heat flow values, and the highest values (>100 mW/m²) are observed in the northeastern part of the Gediz Graben near Kula volcanics.

As a part of the Bouguer gravity anomaly map of Turkey, the gravity anomaly map of western Anatolia exhibit negative anomalies that represents thin crust (Ateş *et al.*, 1999). Sari and Şark (2006) conducted a gravity study in the western Anatolia suggest that the Gediz and Büyük Menderes Grabens show negative Bouguer gravity anomalies, and the thickness of Neogene sediments in the Gediz Graben is more than 2 km according to the 3D analysis of the Bouguer gravity map.

The seismic data studied by Çiftçi and Bozkurt (2009a, 2009b, 2010) reconstructed the depositional history and geometry of the Gediz Graben. They utilized the data from 13 profiles and revealed the lithological boundaries of the sedimentary graben fill and the depth of the metamorphic basement in the existence of the continental extensional regime occurring in western Anatolia. They described two different sub-basins, Alaşehir and Salihli, differentiated by geological structure, evaluation and sedimentary fill. The thickness of the sedimentary fill in Alaşehir and Salihli sub-basins exceeds 3 km, and decreases along the margins. Besides, seismic profiles describe a few different sedimentary units overlying basement (Çiftçi and Bozkurt, 2010).

Çağlar (2001) constructed the electrical resistivity structure of the northwestern Anatolia along a MT profile crossing Istanbul, Sakarya and Bornova Zones. The results obtained from 2D modelling of the transverse electric (TE) and transverse magnetic (TM) mode data (>500 s) indicate a shallow conductive layer ($<80 \Omega\text{m}$) in the Gediz Graben, which is linked with sedimentary sequences in the graben. By using Schlumberger resistivity data, the thickness of the sedimentary fill in the Gediz Graben is given ~ 1.5 km in the study. 2D MT and gravity modeling along the Gediz Graben revealed an undulating basement topography changing in depth between 0.5 and 3-4 km, and two different basins having 3-4 and 1.5-2.5 km deep within the graben is described with the help of two different independently modeled data set (TE and TM mode data) (Gürer *et al.*, 2001). Gürer *et al.*, (2001) also characterized three different main zones in the crust of the Gediz Graben, namely sedimentary fill (15-50 Ωm) and basement of the Menderes Massif (200 Ωm) in the brittle upper crust and a highly conductive zone (10 Ωm) in the lower crust. This lower crustal conductive zone existing at an average depth of 10 km was associated with high heat flow values (120-300 mW/m^2) and shallow earthquake focal depths (average 13 km), which indicates partially melted viscoelastic lower crust. Ulugergerli *et al.*, (2007) also generated the electrical conductivity structure of western Anatolia from the Dardanelles to Gediz Graben through 2D joint inversion of TE and TM mode MT data. They also integrated the results of MT models with gravity, magnetic and earthquake data. The geoelectric models in this study reveal a shallow conductive zone ($<60 \Omega\text{m}$) beneath the northern end of the Gediz Graben, which is attributed to sediments filled the basin. The bottom depth of the grabens existing in western Anatolia is also proposed as ~ 3 km in the study. Erdoğan and

Candansayar (2017) have generated a 3D resistivity model using topographic variations and geological structure near Alaşehir in the Gediz Graben. They computed 3D MT responses of the 3D virtual model and utilized these responses as the input data for both 2D and 3D inverse modeling. They showed the superiority of 3D inversion over 2D inversion in the case of setting the 3D geological structure of the graben. In this study, a new geothermal resource was also revealed.

3.2. Magnetotelluric Measurements

3.2.1. Data Acquisition

The MT method provides to simultaneously measure the time varying natural source EM field components at the surface of the Earth or at the seafloor. The vertical electric field component E_z is zero at a measurement site situated at the surface of the Earth because the atmosphere is a perfect insulator (Chave and Jones, 2012). On the other hand, the measurement of vertical magnetic field component H_z is not necessarily required at every site since this component is only used for the estimation of the tipper vector.

The equipment used for MT data acquisition conventionally consists of sensors for measuring each field components and a data logger for controlling the acquisition process and data storage. There is various type of instruments utilized to measure MT data. The data presented in this thesis were collected using Metronix-ADU-07 (Analog/Digital Signal Conditioning Unit) system at 253 MT sites with additional remote-reference (RR) sites. The magnetic field components (H_x , H_y and H_z) were measured using Metronix MFS06 and MFS07 induction coils. Induction coils are the most generally used magnetic sensors, and an electromotive force (emf) is generated in a coil under the time variation of the component of the magnetic field parallel to the coil axis through the Faraday-Lenz law (Chave and Jones, 2012). The sensors used for measuring the horizontal electric fields were non-polarizable (to avoid additional electrochemical effects) lead, lead-chloride ($Pb-PbCl_2$) electrodes. The electric field components (E_x and E_y) were measured through the potential difference ($\Delta V/x = E_i$) between pairs of electrodes separated by a distance x . The receivers were able to record data in the period range 0.001-1000 s, and connected directly to the ADU-07, which

is the core unit of the system. Figure 3.7 displays a typical site setup utilized in this thesis. The recording unit and a ground electrode were located at the center of the layout, and four electrodes buried typically ~50 m from the center of the layout were oriented geographically north-south and east-west using a compass. To obtain a low contact resistance with the ground, all electrodes were buried in a hole filled with mud made from soil and salt water. The magnetic sensors were also approximately aligned north-south and east-west and besides leveled, and then all of them (north-south, east-west and vertical) were buried in the ground in order to protect them human and animal interferences and to keep them stable for temperature variations. The signals of sensors were stored in the data logger in a particular sampling frequency defined by Nyquist sampling theorem in order to avoid aliasing and oversampling of the data. The data acquisition was separated into several frequency bands with a different sampling frequency, which give way to enhance the sensitivity of sensors at a given frequency range.

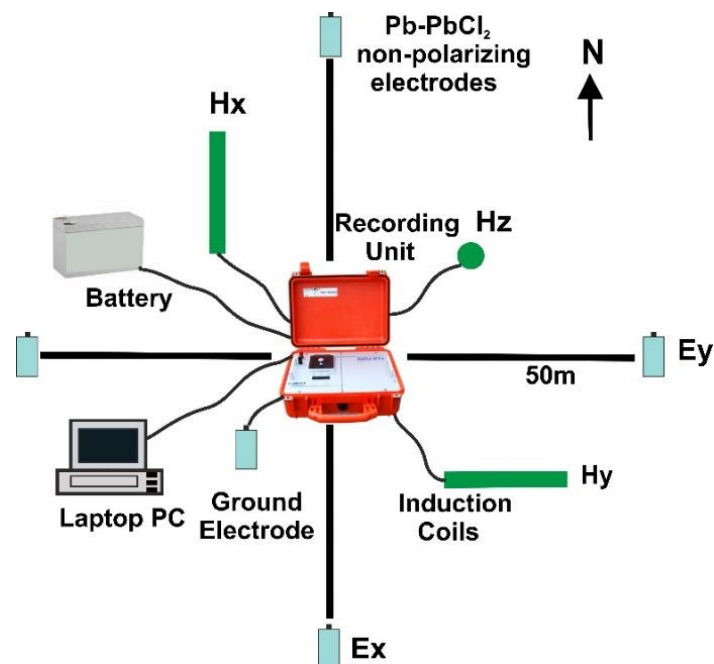


Figure 3.7. A schematic instrument set up of MT sites used for the field campaigns.

The aim of this field study is to image the subsurface electrical resistivity distribution of the study area, namely delineation of the fluid pathways of geothermal manifestations in the Gediz Graben. The MT survey, which was conducted by Ecolog International Service Solutions, WesternGeco and Lemnis Geoscience Ltd., includes 253 MT sites with about 0.2-

1 km irregular site spacing on a 3D grid (Figure 3.8). In the survey, several Metronix-ADU-07 systems were installed at accessible and secure areas in investigation areas C and D as remote reference (RR) sites. They were at least 20 km far from the survey areas. In RR technique, utilizing a signal (usually magnetic) from another site (remote site), the effect of bias at a local site were corrected by spectral analysis methods (Gamble *et al.*, 1979). In this study, the data collected from the RR sites were used to get much better data quality as minimizing the effect of bias arising from uncontrolled local noises.

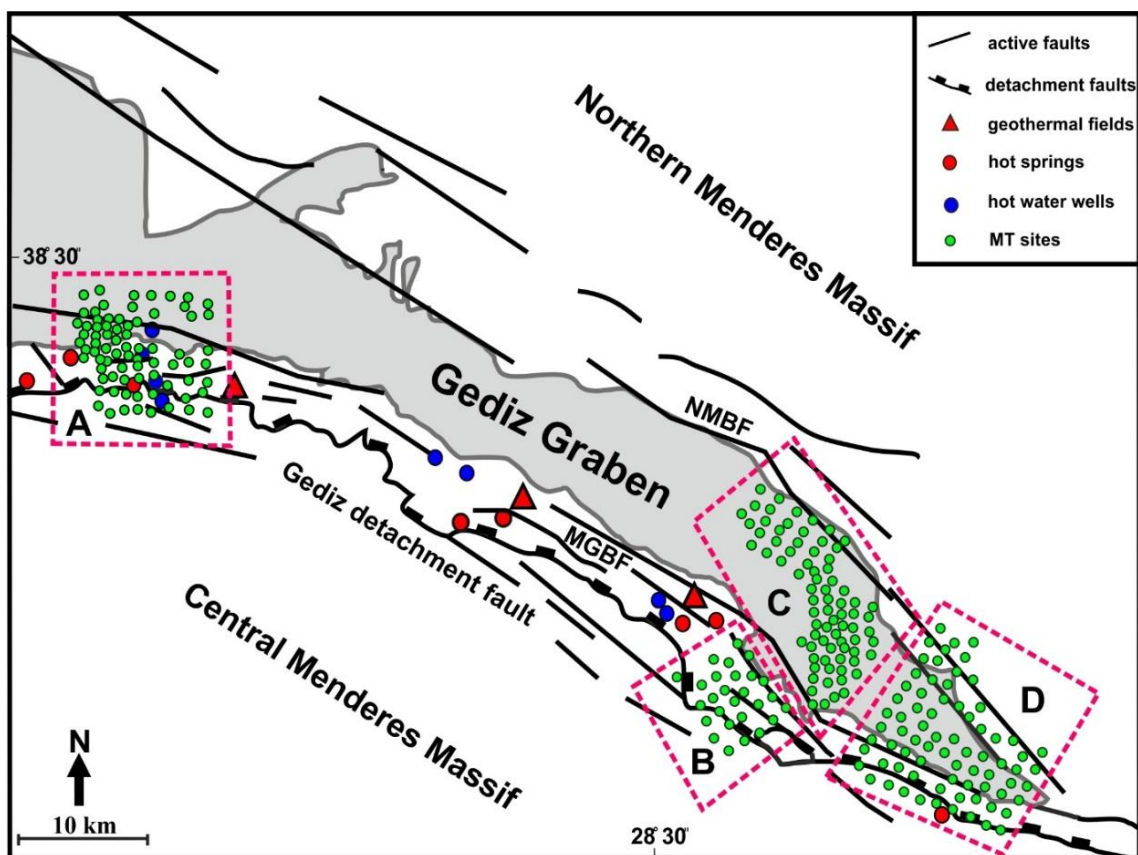


Figure 3.8. MT site distribution over the Gediz Graben, showing the location of the MT sites, geothermal fields, hot springs, hot water wells and surface trace of active faults (modified from Yilmazer *et al.*, 2010; Oner and Dilek, 2013; Mertoğlu *et al.*, 2015). Rectangles A, B, C and D are areas for which 3D modeling was performed. MGBF: Main Graben-Bounding Fault, NMBF: Northern Margin Bounding Fault.

3.2.2. Data Processing

The data recorded by MT data logger and stored on memory card in the form of time series. Firstly, the raw time series data were inspected, and bad or null data were removed. Then, the measured raw time series electric and magnetic field vectors in the MT data processing is reduced to reliable transfer functions which are the frequency domain spectral ratios between field components (Chave and Jones, 2012).

Robust and remote reference processing techniques are used in order to convert the time series data into MT transfer functions. All the processing techniques involve the following steps: pre-conditioning of the data, conversion from the time domain to frequency domain and estimation of transfer functions. Pre-conditioning is necessary to reduce the effects of trends and to remove severe noise (spikes), and also separates the time series into different length segments depending on the period band. Pre-conditioning is achieved with window functions (Jones *et al.*, 1989). The time series data are then transformed into the frequency domain by using a Fourier Transform (Discrete Fourier Transform) or wavelet transform. In the frequency domain, we have the raw power spectrum for each time segment for each channel (E_x , E_y , H_x , H_y and H_z), which are used to calculate the auto and cross spectra for each time segment. The auto and cross spectra are essentially the products of the field components and their complex conjugates, and they are stored in a spectral matrix for each evaluation frequency. There are several spectral matrices for the same evaluation frequency, and then, they are stacked. By attributing a weight to the spectra from each particular window, the stacking process can be modified. The weights can be defined by manually editing or with a robust technique. Then, the Earth response or transfer functions (the impedance tensor and tipper vector) are calculated (Simpson and Bahr, 2005).

The Equations 2.53 and 2.54 can be expanded as below

$$E_x(\omega) = Z_{xx}(\omega) \cdot H_x(\omega) + Z_{xy}(\omega)H_y(\omega) + \mathcal{Z}Z(\omega) \quad (3.1)$$

$$E_y(\omega) = Z_{yx}(\omega) \cdot H_x(\omega) + Z_{yy}(\omega)H_y(\omega) + \mathcal{Z}Z(\omega) \quad (3.2)$$

$$H_z(\omega) = T_x(\omega) \cdot H_x(\omega) + T_y(\omega)H_y(\omega) + \mathcal{Z}T(\omega) \quad (3.3)$$

where $\mathcal{Z}Z(\omega)$ and $\mathcal{Z}T(\omega)$ are called as reminder functions and represent uncorrelated noise (electrical noise for that case), which are necessary due to the measurement errors. The statistical solutions for impedance tensor \mathbf{Z} are needed to minimize this type of noise (Simpson and Bahr, 2005).

The least squares and robust processing techniques based on statistical processing methods are generally used to remove noise from MT data and used to solve the Equations 3.1, 3.2 and 3.3 as a bivariate linear regression problem (Simpson and Bahr, 2005). Therefore, the impedance elements can be estimated as below

$$Z_{xx} = \frac{\langle E_x R_x^* \rangle \langle H_y R_y^* \rangle - \langle E_x R_y^* \rangle \langle H_y R_x^* \rangle}{DET} \quad (3.4)$$

$$Z_{xy} = \frac{\langle E_x R_y^* \rangle \langle H_x R_x^* \rangle - \langle E_x R_x^* \rangle \langle H_x R_y^* \rangle}{DET} \quad (3.5)$$

$$Z_{yx} = \frac{\langle E_y R_x^* \rangle \langle H_y R_y^* \rangle - \langle E_y R_y^* \rangle \langle H_y R_x^* \rangle}{DET} \quad (3.6)$$

$$Z_{yy} = \frac{\langle E_y R_y^* \rangle \langle H_x R_x^* \rangle - \langle E_y R_x^* \rangle \langle H_x R_y^* \rangle}{DET} \quad (3.7)$$

and the tipper elements are given by

$$T_x = \frac{\langle H_z R_x^* \rangle \langle H_y R_y^* \rangle - \langle H_z R_y^* \rangle \langle H_y R_x^* \rangle}{DET} \quad (3.8)$$

$$T_y = \frac{\langle H_z R_y^* \rangle \langle H_x R_x^* \rangle - \langle H_z R_x^* \rangle \langle H_x R_y^* \rangle}{DET} \quad (3.9)$$

where

$$DET = \langle H_x R_x^* \rangle \langle H_y R_y^* \rangle - \langle H_x R_y^* \rangle \langle H_y R_x^* \rangle \quad (3.10)$$

and R_x^* and R_y^* are either local or remote complex conjugate electric or magnetic fields. In practice, magnetic remote reference is preferred over electric field since the horizontal magnetic fields shows greater homogeneity than the electric fields in the vicinity of lateral heterogeneities, and they are less affected by noise than the electric fields. Therefore, a remote magnetic field estimate is the least biased and thus statistically best (Simpson and Bahr, 2005).

There are several processing codes (e.g., Egbert and Booker, 1986; Larsen *et al.*, 1996; Egbert, 1997). In this thesis, robust processing software ProcMT (Metronix, Germany) and robust remote reference processing code suggested by Larsen *et al.*, (1996) were used to estimate smooth MT transfer functions relating the electric and magnetic field data collected in areas A and B, and C and D, respectively. These smoothly varying transfer functions pave the way for the identification and the removal of electric and magnetic outliers, performing the frequency and time domain weights utilized for obtaining robust estimates, and separation of the time series into MT and correlated noise signals, with the assumption that the remote site is free of the correlated noise (Larsen *et al.*, 1996). This iteratively determines the transfer functions between the local and remote (noisy free) magnetic fields from the original and decimated time series data. This iterative process facilitates to correct the outliers from the local magnetic field used in an iterative re-weighted method to define the impedance tensor. The electric fields are also corrected in time and frequency domain during the iterations by utilizing a smooth MT transfer function as estimating the electric field data from magnetic field data. This procedure is repeated for each time series band, and the complete sounding file is obtained by merging the results. Figure 3.9 shows the off-diagonal impedance elements, which is obtained by implementing above procedure on time series data, for sample sites A-1600 from area A, B-505 from area B, C-87-36 from area C and D-90-89 from area D. The MT data collected at four different areas of the graben is not affected by static shift.

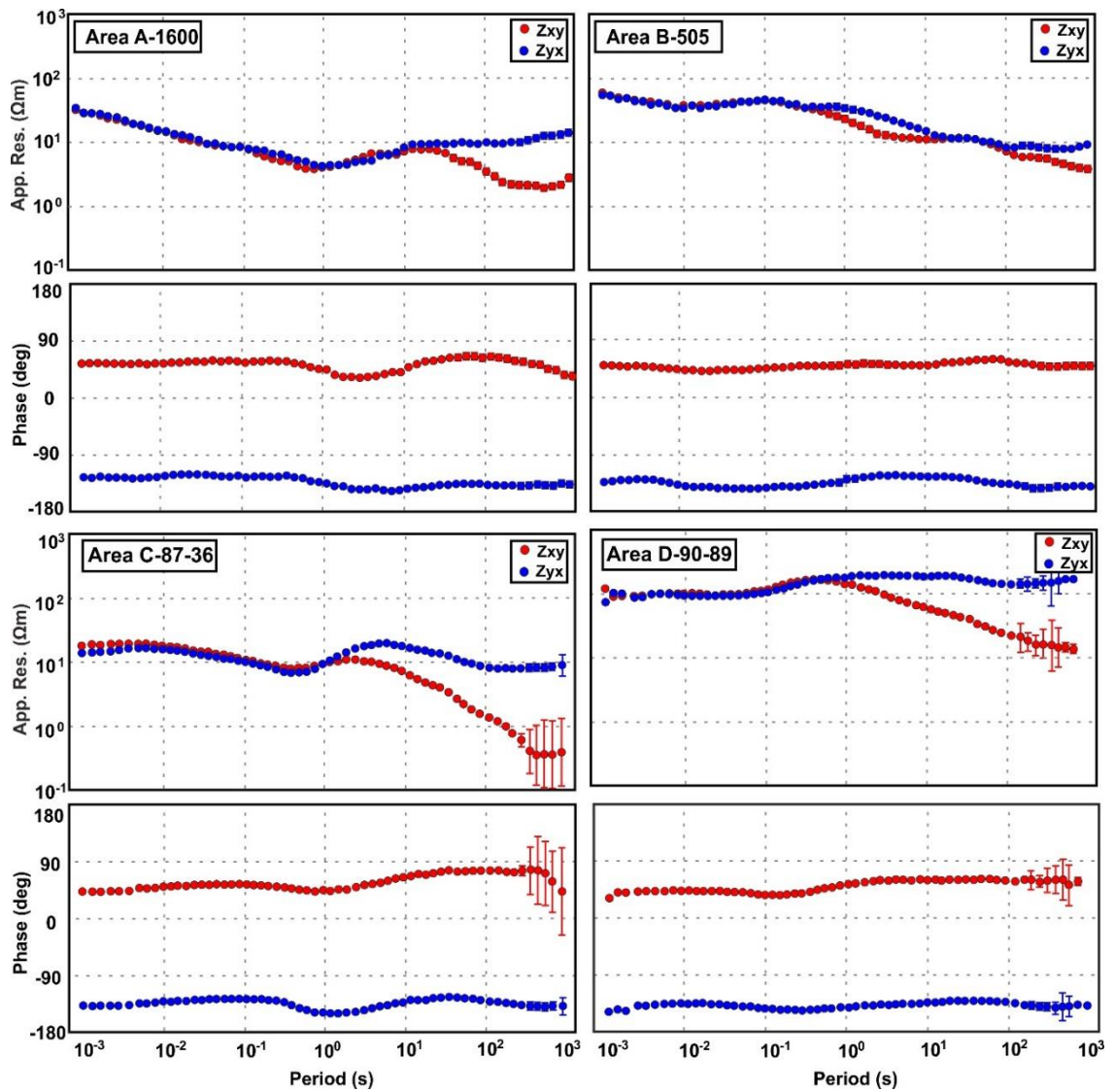


Figure 3.9. Observed apparent resistivity and phase curves of four representative sites A-1600 from area A, B-505 from area B, C-87-36 from area C and D-90-89 from area D, derived from the off-diagonal components of the impedance tensor Z .

3.2.3. Data Analysis

The analysis of the Gediz Graben data set has been performed utilizing the technique called as magnetotelluric phase tensor analysis (simply called as phase tensor). This technique provides a distortion-free information about the dimensionality and directionality of the data (Caldwell *et al.*, 2004).

The magnetotelluric phase tensor (Φ) characterized by the relation between the real (\mathbf{X}) and imaginary (\mathbf{Y}) parts of the impedance tensor, and it is described graphically by an ellipse defined by four invariants that are the major (Φ_{\max}) and minor (Φ_{\min}) axes, skew angle (β) and non-invariant angle (α) (Figure 3.10). The maximum and minimum phase difference between the horizontal components of the electric and magnetic fields is determined by the principle axes of the phase tensor whereas the asymmetry in the MT responses is characterized by the phase tensor skew angle (Caldwell *et al.*, 2004).

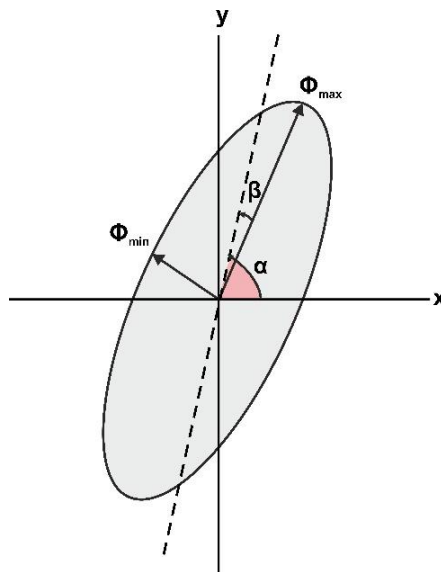


Figure 3.10. Graphical representation of a phase tensor ellipse and its invariants Φ_{\min} , Φ_{\max} , β and α (modified from Caldwell *et al.*, 2004).

Following Caldwell *et al.*, (2004), the phase tensor (Φ) can be given as below

$$\mathbf{Z} = \mathbf{X} + i\mathbf{Y} \quad (3.11)$$

$$\Phi = \mathbf{X}^{-1}\mathbf{Y} \quad (3.12)$$

When we assume that the tensor \mathbf{D}' describing the distortion over regional impedances, we can write:

$$\mathbf{Z}_R = \mathbf{X}_R + i\mathbf{Y}_R \quad (3.13)$$

Then, the relationship between the phase tensors of the observed and regional impedance tensors can be written from Equation 3.12:

$$\Phi = \mathbf{X}^{-1}\mathbf{Y} = (\mathbf{D}' \mathbf{X}_R)^{-1}(\mathbf{D}' \mathbf{Y}_R) = \mathbf{X}_R^{-1}\mathbf{D}'^{-1}\mathbf{D}' \mathbf{Y}_R = \mathbf{X}_R^{-1}\mathbf{Y}_R = \Phi_R \quad (3.14)$$

According to Equation (3.14), the observed and regional phase tensors are identical and thus, they are independent from distortions. The attraction of this approach is the independence of the electric field galvanic distortions (but not the magnetic field distortions) (Jones, 2012).

In a Cartesian coordinate system (x, y), Φ can be written in a matrix form:

$$\begin{bmatrix} \Phi_{xx} & \Phi_{xy} \\ \Phi_{yx} & \Phi_{yy} \end{bmatrix} = \frac{1}{\det(\mathbf{X})} \begin{bmatrix} X_{yy}Y_{xx} - X_{xy}Y_{yx} & X_{yy}Y_{xy} - X_{xy}Y_{yy} \\ X_{xx}Y_{yx} - X_{yx}Y_{xx} & X_{xx}Y_{yy} - X_{yx}Y_{xy} \end{bmatrix} \quad (3.15)$$

where $\det(\mathbf{X}) = X_{xx}Y_{yy} - X_{yx}Y_{xy}$ is the determinant of \mathbf{X} .

The phase tensor invariants, trace, skew and determinant of the matrix are algebraically defined as

$$tr(\Phi) = \Phi_{xx} + \Phi_{yy} \quad (3.16)$$

$$sk(\Phi) = \Phi_{xy} + \Phi_{yx} \quad (3.17)$$

$$\det(\Phi) = \Phi_{xx} \Phi_{yy} - \Phi_{xy} \Phi_{yx} \quad (3.18)$$

By re-expressing all invariants as the first order functions:

$$\Phi_1 = \text{tr}(\Phi)/2 \quad (3.19)$$

$$\Phi_2 = [\det(\Phi)]^{1/2} \quad (3.20)$$

$$\Phi_3 = \text{sk}(\Phi)/2 \quad (3.21)$$

Then, the main invariants Φ_{\min} , Φ_{\max} and β is defined by the equations:

$$\Phi_{\min} = (\Phi_1^2 + \Phi_3^2)^{1/2} - (\Phi_1^2 + \Phi_3^2 - \Phi_2^2)^{1/2} \quad (3.22)$$

$$\Phi_{\max} = (\Phi_1^2 + \Phi_3^2)^{1/2} + (\Phi_1^2 + \Phi_3^2 - \Phi_2^2)^{1/2} \quad (3.23)$$

$$\beta = \frac{1}{2} \tan^{-1} \left(\frac{\Phi_{xy} - \Phi_{yx}}{\Phi_{xx} + \Phi_{yy}} \right) \quad (3.24)$$

The angle, α expressing the dependence of the tensor on the coordinate system is

$$\alpha = \frac{1}{2} \tan^{-1} \left(\frac{\Phi_{xy} + \Phi_{yx}}{\Phi_{xx} - \Phi_{yy}} \right) \quad (3.25)$$

The characteristics of the phase tensor ellipses provide the information about the dimensionality of the data. In 1D Earth model, the phase tensor is described by a unit circle. In 2D Earth model, the phase tensor is symmetric ($\beta = 0$), and Φ_{\max} is parallel or perpendicular to the geoelectric strike. For a 3D Earth model, the phase tensor is non-symmetric ($\beta \neq 0$). In that case, β characterizes a measure of the dimensionality of the MT data. The large values of β ($|\beta| > 3^\circ$) implies the presence of a 3D regional resistivity structure (Caldwell *et al.*, 2004).

Plotting the phase tensor ellipses gives essential information about dimensionality of the data and additional information about the direction of the current flow. The phase tensor ellipses of the Gediz Graben data set are drawn for short (0.001 s), intermediate (1s) and long (268 s) periods, derived from phase tensor analysis according to Caldwell *et al.*, (2004) (Figures 3.11, 3.12, 3.13 and 3.14).

The phase tensor ellipses of area A at short period (i.e., 0.001 s) show weak polarizations and skew values mostly smaller than $[-2^\circ \ 2^\circ]$, which implies that one-or-two dimensionality is dominant at shallow depths. At intermediate period (i.e., 1s), ellipses exhibit 2D character at most of the sites, which is indicated by small skew angles ($|\beta| < 3^\circ$) and the polarization directions of the phase tensor ellipses. The polarization direction of most of the ellipses at that period shows a consistent trend with the regional strike direction, as being parallel or perpendicular to the GDF and normal faults existing in the study area. At long period (i.e., 268 s), most of the sites show a skew value above $|\beta| > 3^\circ$ (as indicated by dark red and dark blue colors), characterizing an asymmetric resistivity structure or 3D environment. Furthermore, the orientation of the phase tensor ellipses, as being perpendicular to the faults seems to be affected by the GDF and normal faults (Figure 3.11).

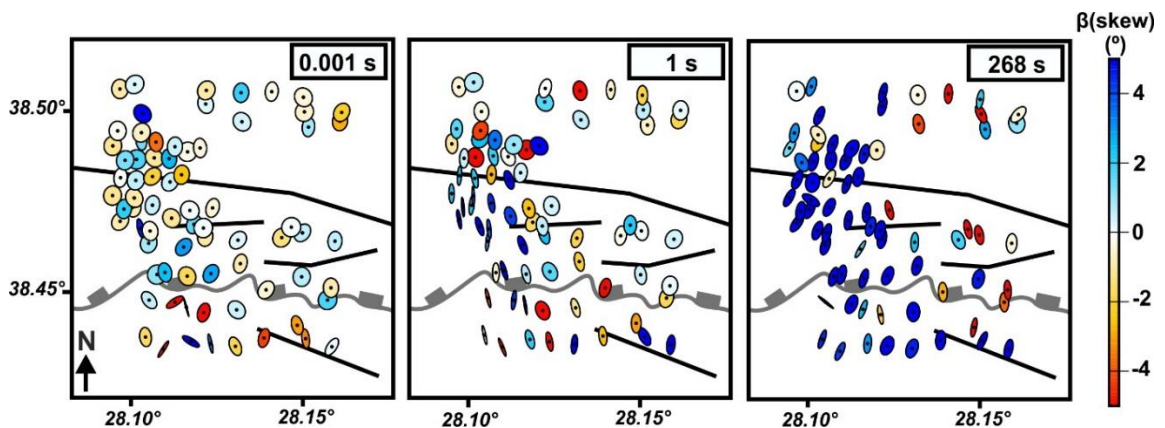


Figure 3.11. Map view of observed phase tensor ellipses at three selected periods 0.001 s, 1 s, and 286 s for area A. The phase tensor ellipses are normalized with major axes and filled with the skew angle. The black lines indicate surface trace of faults. The gray lines mark the GDF.

The MT data from area B at short (i.e., 0.001 s) and intermediate (i.e., 1 s) periods have a skew angle of phase tensor less than 3° for most of sites, which is consistent with 1D and 2D regional resistivity structures. Most of the principle axes of the ellipses close to the normal faults also point to the NW-SE or opposite direction, indicating a 2D environment. However, at long period (i.e., 268 s), the phase tensors show a clear ellipticity with extremely flattened ellipses at sites located above the GDF and normal faults. The flattened ellipses are an indicator of the presence of abrupt lateral geoelectrical interfaces caused by faults. Furthermore, the polarization direction of the ellipses above the GDF and normal faults shows perpendicular direction with respect to the strike of the faults (Figure 3.12). Therefore, the characteristic of phase tensor ellipses at long periods indicates the existence of a 3D resistivity structure in corresponding depths.

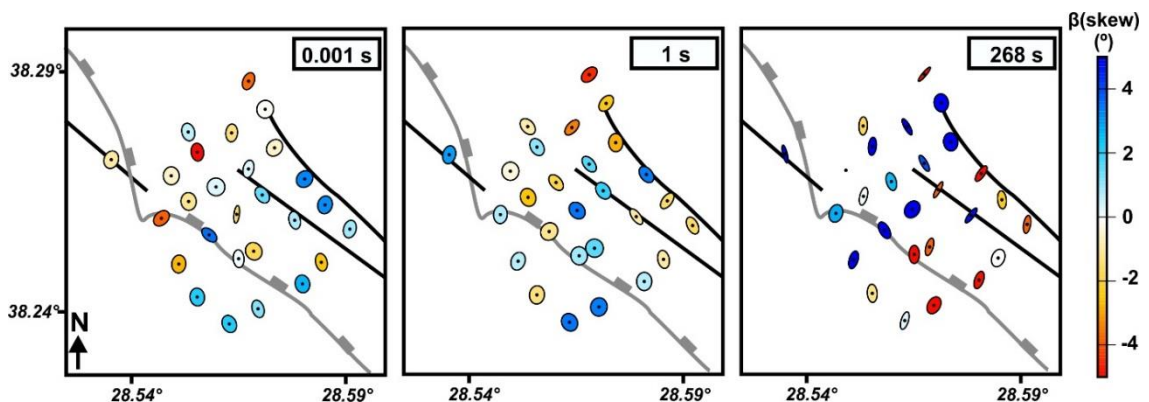


Figure 3.12. Map view of observed phase tensor ellipses at three selected periods 0.001 s, 1 s and 286 s for area B. The phase tensor ellipses are normalized with major axes and filled with the skew angle. The black lines indicate surface trace of faults. The gray lines mark the GDF.

The phase tensor ellipses of area C at short period (i.e., 0.001 s) show circular geometry at almost all sites with skew angles close to zero, suggesting a 1D resistivity structure. At intermediate period (i.e., 1 s), the skew angle of phase tensors is less than 3° and major axes of most of the ellipses are aligned in the NE direction and others show a polarization direction perpendicular to that direction, which indicates a 2D resistivity structure. At long period (i.e., 268 s), phase tensors exhibit a strong ellipticity with higher skew values (mostly $> [-4^\circ \ 4^\circ]$) at most sites, and flattened ellipses indicate the existence of abrupt lateral geoelectrical interfaces at that depth, indicating complex 3D features. The

phase tensors ellipses of MT sites situated above the normal fault also show high skew values and a polarization direction parallel to the fault (Figure 3.13).

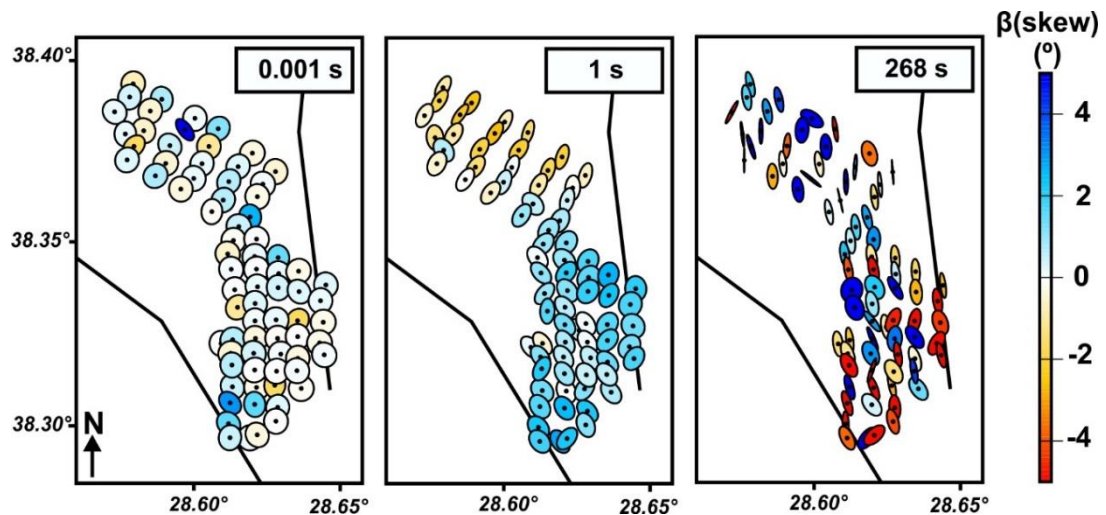


Figure 3.13. Map view of observed phase tensor ellipses at three selected periods 0.001 s, 1 s, and 286 s for area C. The phase tensor ellipses are normalized with major axes and filled with the skew angle. The black lines indicate surface trace of faults.

The MT data from area D at short period (i.e., 0.001 s) exhibit circular phase tensor ellipses with skew angles close to zero for most of sites, which suggests a 1D regional resistivity structure. At intermediate period (i.e., 1 s), most of sites show small values of skew angle ($|\beta| < 3^\circ$), and phase tensor ellipses display a polarization direction parallel or perpendicular to the regional strike, namely the GDF and normal faults, which suggests a 2D resistivity structure. At long period (i.e., 268 s), phase tensors indicate a strong ellipticity and high values of skew angles ($|\beta| > 3^\circ$), which indicates a 3D regional resistivity structure at corresponding depth. The polarization direction of phase tensor ellipses at long period also show a consistent trend of the NW-SE, which is coincident with the regional strike direction and parallel to the GDF and normal faults existing in the study area (Figure 3.14).

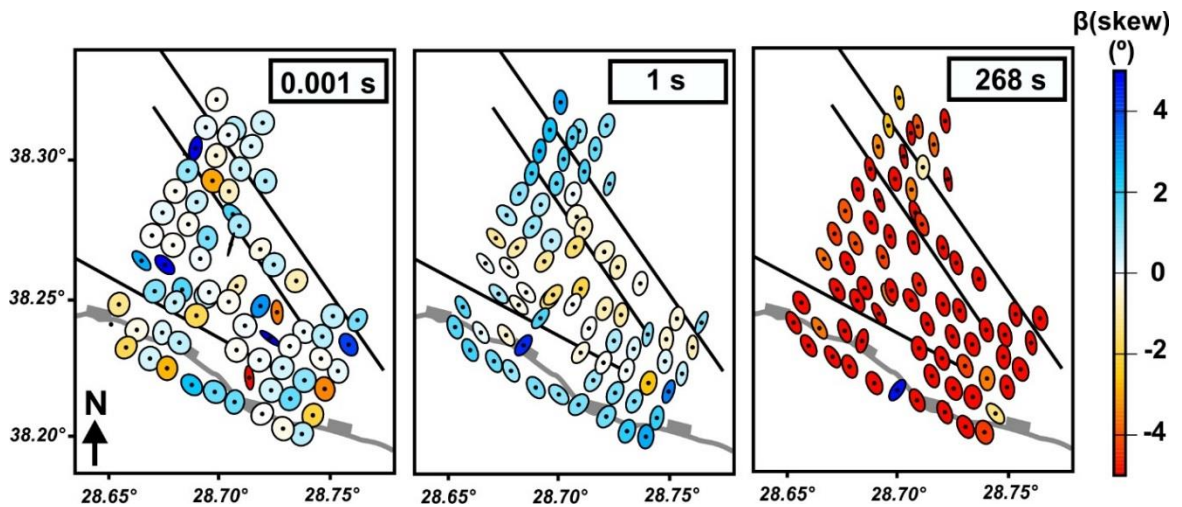


Figure 3.14. Map view of observed phase tensor ellipses at three selected periods 0.001 s, 1 s and 286 s for area D. The phase tensor ellipses are normalized with major axes and filled with the skew angle. The black lines indicate surface trace of faults. The gray lines mark the GDF.

In order to illustrate the preferred geoelectric strike direction, the results of phase tensor analyses are shown in the form of rose diagrams of geoelectric strike angles for all periods and different range of periods (Figures 3.15, 3.16, 3.17 and 3.18). Rose diagrams are plotted by period in order to depict information about geoelectric strike direction of various depths. These diagrams as circular histograms represent the occurrence rate of observed strike values, and high amplitudes (red color) of their values show the dominant direction of strike. The geoelectric strike direction has a principal 90° ambiguity, which can be clarified by the structural trend of the study area.

The rose diagram obtained using the MTPy python toolbox (Krieger and Peacock, 2014) shows the regional geoelectric strike when analyzing the data containing all periods (0.001-1000 s) of sites from area A (Figure 3.15a). It exhibits an average strike direction of $N100^\circ E$ that is consistent with nearly the E-W or WNW-ESE trending regional structural style dominated by the Gediz Graben, GDF and active normal faults of the area (Oner and Dilek, 2013), and the N-S oriented regional direction of extension as being perpendicular to that direction (Çiftçi and Bozkurt, 2007). Figure 3.15b also provides information about the geoelectric strike direction for different period bands. At long periods (>10 s), rose diagrams show more obvious and uniform directions, which is compatible with the overall WNW-

ESE direction obtained for all periods and sites. At periods lower than 10 s, rose diagrams do not exhibit a clear direction of the geoelectric strike (except the period range 0.01-0.1 s), which represents local structure instead of regional resistivity structure.

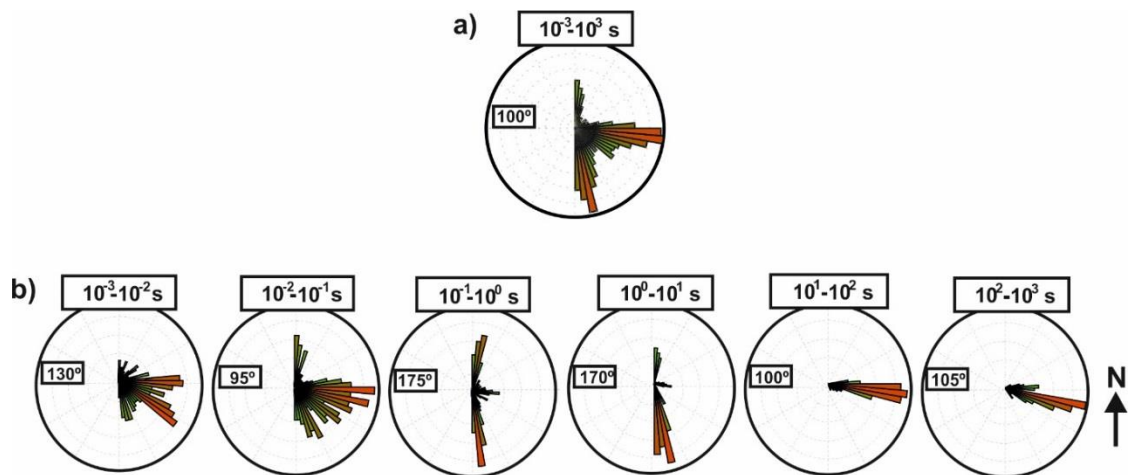


Figure 3.15. Rose diagram representation of regional geoelectric strike angles showing strike estimated from the azimuth of phase tensor for the data from area A for the full period range (a) and different period ranges (b) shown on each subfigures. Red sectors illustrate dominant direction of strike. Strike values change between 0° and 180° . 0° is north and 90° is east. The resolution of the rose diagrams is 5° .

The rose diagram in Figure 3.16a displays the regional geoelectric strike as analyzing the data including all periods (0.001-1000 s) of sites from area B. It shows an average strike direction of N145°E. This direction is probably corresponding to the direction of the GDF and near surface normal faults and their extensions. Figure 3.16b shows rose diagrams of geoelectric strike angles for different period bands. The data also exhibits a consistent strike direction with the period ranges from 0.001 to 100 s, as shown in Figure 3.16b.

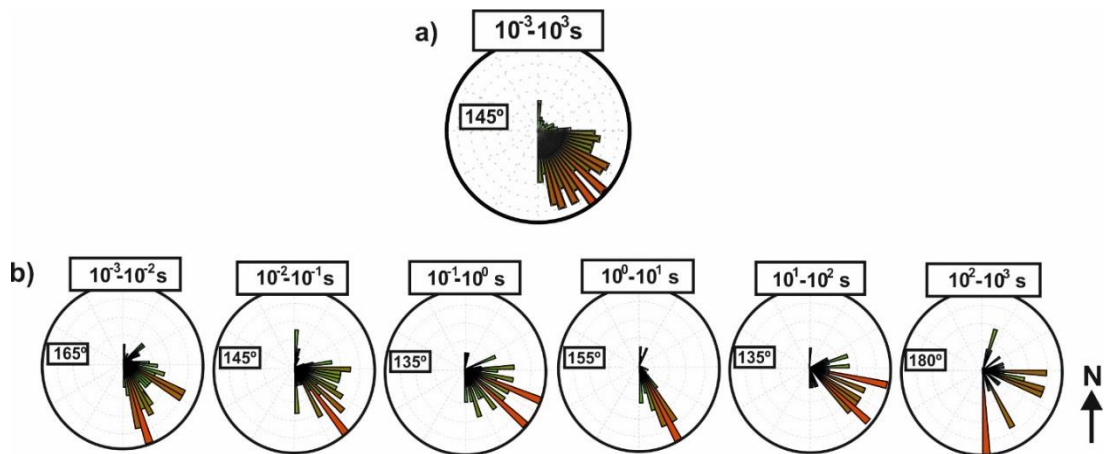


Figure 3.16. Rose diagram representation of regional geoelectric strike angles showing strike estimated from the azimuth of phase tensor for the data from area B for the full period range (a) and different period ranges (b) shown on each subfigures. Red sectors illustrate dominant direction of strike. Strike values change between 0° and 180° . 0° is north and 90° is east. The resolution of the rose diagrams is 5° .

The rose diagrams in Figure 3.17a and b show the regional geoelectric strike for all data points of MT sites from area C. The geoelectric strike directions were computed for sites located at the northern (a) and southern part of the study area (b). It depicts an average strike direction of $N115^{\circ}E$ for northern part and $N125^{\circ}E$ for the southern parts. The geoelectric strike directions for two sub-regions are coincident with the NNW-SSE trending regional strike direction. Figure 3.17c and d exhibit rose diagrams of geoelectric strike angles for different period bands for the northern and southern parts of the study area, respectively. At short periods (<1 s), rose diagrams show a messy pattern of which may result from the dominant 1D character of the data at corresponding periods. At long periods (>1 s), the direction of geoelectric strikes is simple and represent regional resistivity structure of the study area.

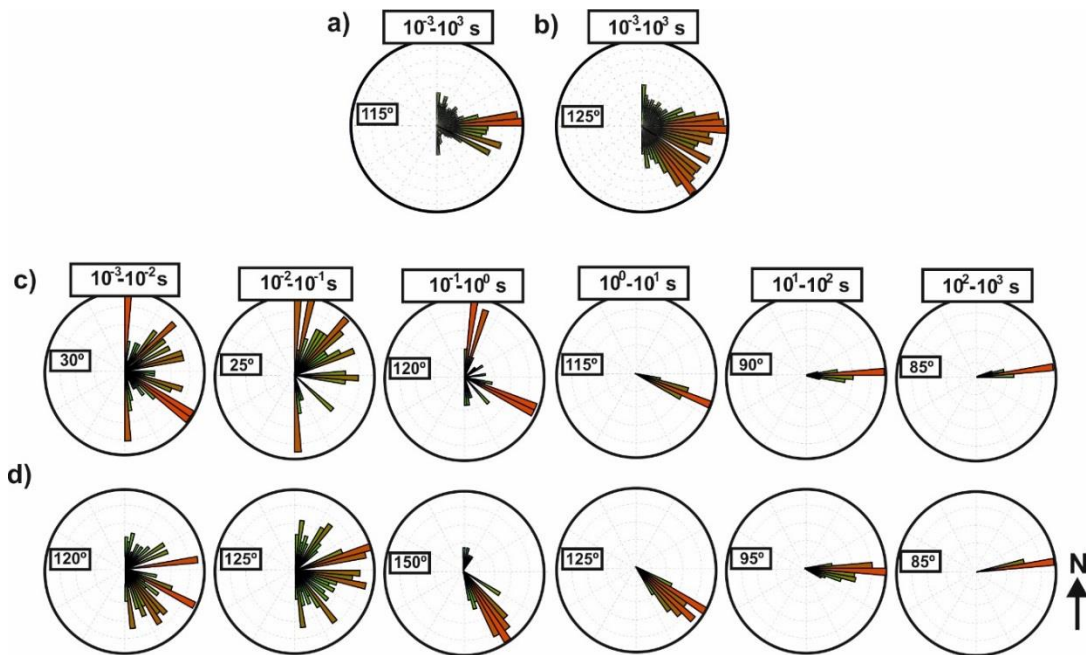


Figure 3.17. Rose diagram representation of regional geoelectric strike angles showing strike estimated from the azimuth of phase tensor for the data from area C for the full (a and b) and different period ranges (c and d) shown on each subfigures. a and c show strike directions computed for sites located at the northern part of the area C while b and d show strike directions computed for sites located at the southern part of the area C. Red sectors illustrate dominant direction of strike. Strike values change between 0° and 180° . 0° is north and 90° is east. The resolution of the rose diagrams is 5° .

Figure 3.18a, b and c show the rose diagrams of geoelectric strike angles for all data points of sites located at the northern part of the Gediz Graben, at the Gediz Graben, and at the southern part of the Gediz Graben, respectively. It exhibits an average strike direction of $N85^\circ E$, $N80^\circ E$ and $N105^\circ E$ for three different sub-regions, successively. The geoelectric strike directions are coincident with the NW-SE trending regional structural style of the eastern end of the Gediz Graben, namely the direction of the GDF and active normal faults of the area C. Figure 3.18d, e and f also give information about the geoelectric strike directions for different period bands for three sub-regions. At long periods (>10 s), rose diagrams exhibit a clear image of geoelectric strike directions, which is consistent with the overall NW-SE direction obtained for all periods and sites. At short periods (<1 s), rose diagrams show a messy pattern due to local inhomogeneities, as shown in Figure 3.18d, e, and f.

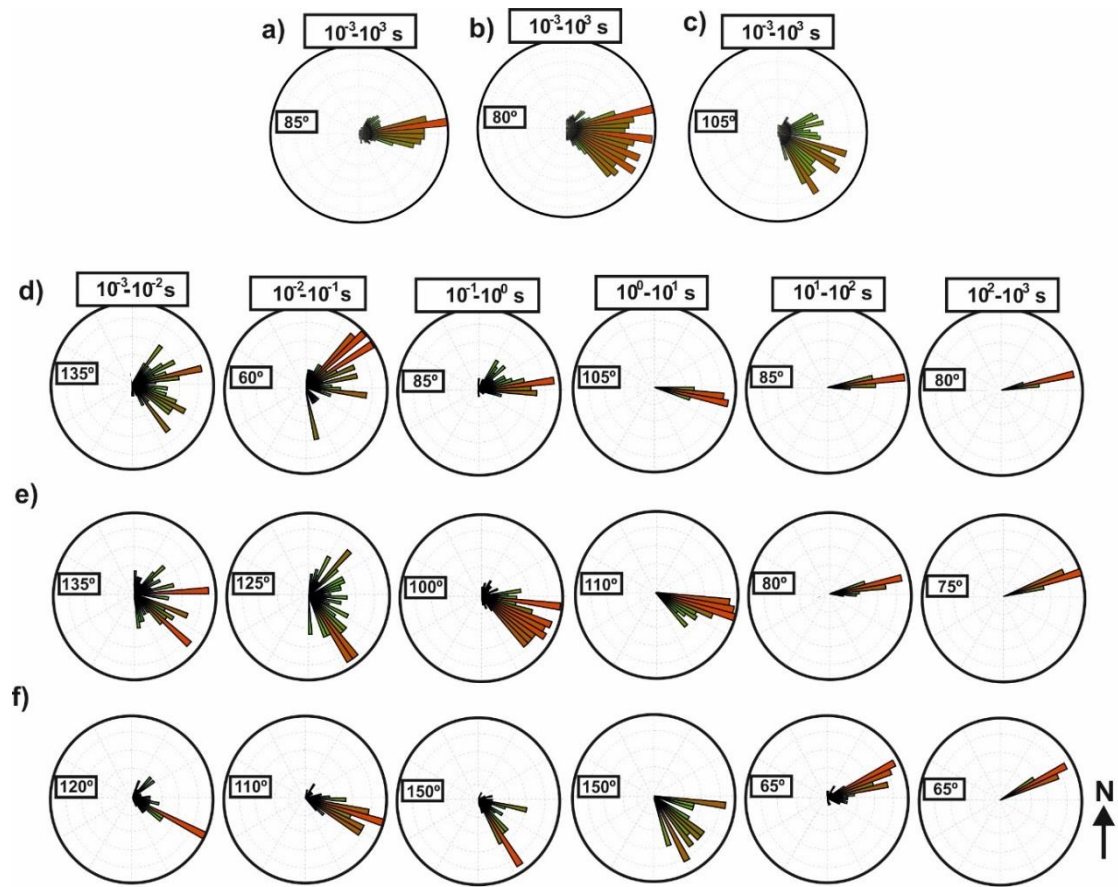


Figure 3.18. Rose diagram representation of regional geoelectric strike angles showing strike estimated from the azimuth of phase tensor for the data from area D for the full (a, b and c) and different period ranges (d, e and f) shown on each subfigures. a and d show strike directions computed for sites located at the northern part of the Gediz Graben, b and d show strike directions computed for sites located at the graben, and c and f show strike directions computed for sites located at the southern part of the graben. Red sectors illustrate dominant direction of strike. Strike values change between 0° and 180° . 0° is north and 90° is east. The resolution of the rose diagrams is 5° .

According to phase tensor analysis, numerous 3D effects, which are shown by the large number of data points where the phase tensor skew values are significantly high ($|\beta| > 3^\circ$) (Figures 3.11, 3.12, 3.13 and 3.14), are characteristic on the data set. The dominant 3D behavior of the Gediz Graben data set proves the need to do a 3D interpretation. The data set exhibits a predominant regional geoelectric strike direction of N100°E for area A, N145°E for area B, N115°E and N125°E for two sub-regions of area C, and N85°E, N80°E and N105°E

for three sub-regions of area D, respectively, which confirms the direction of regional structural style of the study areas (Figures 3.15a, 3.16a and b, 3.17a, b and c, and 3.18a).

4. MODELING OF MAGNETOTELLURIC DATA

4.1. Magnetotelluric Modeling

The crucial step of MT data processing is to convert the frequency domain impedance data into a resistivity model as a function of depth. In this way, we relate our models to geology and Earth processes in order to explain the current state of subsurface, which is ideally achieved by forward modeling and inversion of MT responses.

Forward modeling is a procedure controlling the generation of synthetic transfer functions for a given resistivity structure whereas inversion is an automated procedure that iteratively updates the resistivity model in order to fit its response to the observed data. Most modelling schemes discretize the Earth model (2D and 3D) into cells, and allows us to decide the resistivity within each individual cell. Based on the chosen Earth model, Maxwell's equations are solved within each cell by applying appropriate boundary conditions. The differential equation (finite difference and finite element), integral equation and hybrid methods can be used for setting equation systems and thus finding unknown fields. When knowing the field components (one field component can be calculated from the other one with the help of the relation between them), the transfer functions can be calculated. Therefore, these calculated synthetic responses can be compared with the measured data, and the differences between them describes RMS (Root Mean Square) misfit. Obviously, finding a model representing the observed data is a trial and error process. Until a satisfactory fit to the measured data is succeeded, the responses are calculated as continuously changing the input data, which is a time consuming process. In the inversion, that is automatically achieved by a combination of forward modeling and minimization of the misfit between observed data and model responses (i.e., predicted data) (Simpson and Bahr, 2005).

Any general inverse problem can be stated as

$$\mathbf{d} = \mathbf{f}(\mathbf{m}) \quad (4.1)$$

where $\mathbf{d} = d_1, d_2, \dots, d_N$ is the data vector (N -dimensional impedances in MT), \mathbf{f} is the forward operator, and $\mathbf{m} = m_1, m_2, \dots, m_M$ is the model parameter vector (M -dimensional Earth's conductivity in MT) (Egbert and Kelbert, 2012). The ultimate aim of solving this inverse problem is finding a model whose forward responses best fit the observed data with a tolerable error, which is achieved by minimizing the penalty function which controls the discrepancy between the observed (\mathbf{d}) and predicted data ($\mathbf{f}(\mathbf{m})$) (Chave and Jones, 2012). Then, the inverse problem can be written in a form of

$$\mathbf{f}(\mathbf{d}, \mathbf{m}) = \mathbf{d} - \mathbf{f}(\mathbf{m}) + \epsilon \quad (4.2)$$

where ϵ represents error.

The conceptual model consisting of a number of cells could resolves the resistivity or conductivity gradients rather than sharp boundaries. Moreover, the nonlinearity between the MT data and the resistivity model is also commonly approximated as linear with respect to a starting model (Simpson and Bahr, 2005). Therefore, due to physical assumptions, model parameterization (i.e., $M > N$), data errors and a limited frequency band, more than one model responses corresponding to the distinct models can be fitted to the measured data (non-uniqueness). In this situation, a regularization or a smoothness constraint is essential to impose the stability of the inversion as searching a regularized solution when increasing spatial smoothness and minimizing error (Tikhonov and Arsenin, 1977; Bedrosian, 2007). In this thesis, within the 3D inversion process, the Modular Electromagnetic Inversion System (ModEM) (Meqbel, 2009; Egbert and Kelbert, 2012; Kelbert *et al.*, 2014), a linearized inversion through gradient-based minimization of the penalty function Θ containing data and model regularization terms seeks an adequate fit to the data vector \mathbf{d} (Egbert and Kelbert, 2012):

$$\Theta(\mathbf{m}, \mathbf{d}) = (\mathbf{d} - \mathbf{f}(\mathbf{m}))^T \mathbf{C}_d^{-1} (\mathbf{d} - \mathbf{f}(\mathbf{m})) + v(\mathbf{m} - \mathbf{m}_0)^T \mathbf{C}_m^{-1} (\mathbf{m} - \mathbf{m}_0) \quad (4.3)$$

where \mathbf{C}_d is the covariance of data errors, \mathbf{C}_m is the model covariance or regularization term, \mathbf{m}_0 is a priori or initial guess model, and v is a trade-off parameter. In practice, \mathbf{C}_d is always chosen as being diagonal matrix in case of a simple rescaling of the data and forward

response and consists of the inverse of the squared data errors e_i for each data point ($\text{diag}(1/\hat{e}_i^2)$). \mathbf{C}_m is a scaling and smoothing operator for regularization and applied to the deviation from the current model \mathbf{m} to priori model \mathbf{m}_0 .

The ModEM inversion algorithm employs non-linear conjugate gradients (NLCG) to minimize the penalty function. The algorithm, which uses the finite difference approximations to solve Maxwell's equations on a staggered grid (Yee, 1966; Wang and Hohmann, 1993), discretizes the governing differential equations for numerical solutions. The NLCG solutions in ModEM provide to use memory more efficiently and allow dealing with a huge number of data and model parameters. The program distributes the computation of the blocks among several processors (i.e., parallel computing of forward responses), and thus reduces the computation time and memory needed to save the sensitivity matrix by using memories of different processors. This is applied by using calls of the standard Message Passing Interface (MPI) communication library that provides to communicate between processors and to exchange messages between them (Meqbel, 2009; Kelbert *et al.*, 2014). Therefore, the algorithm is recently used in many studies (e.g., Tietze and Ritter, 2013; Kiyan *et al.*, 2014; Sass *et al.*, 2014; Pina-Varas *et al.*, 2014; Meqbel *et al.*, 2014; Yin *et al.*, 2016, 2017; Didana *et al.*, 2015; Erdođan and Candansayar, 2017; Campanya *et al.*, 2018).

The discrete formulation of the forward problem is essential for numerical solutions since all spaces, which are EM fields, measured data and model parameters, are defined in finite dimensions (Egbert and Kelbert, 2012). The finite difference method is an effective and easy tool to numerically solve the EM boundary-value problem (Zhdanov, 2015 and references therein). The second-order system of partial differential equations in terms of electric fields (magnetic fields are eliminated) in the frequency domain can be expressed as

$$\nabla \times \nabla \times \mathbf{E} + i\omega\mu\sigma\mathbf{E} = 0 \quad (4.4)$$

where the tangential components of \mathbf{E} are defined on all boundaries (Egbert and Kelbert, 2012). The Equation (4.4) for the field components can be written as below

$$\begin{aligned}
-i\omega\mu\sigma E_x &= \frac{\partial}{\partial z} \left(\frac{\partial E_x}{\partial z} + \frac{\partial E_z}{\partial x} \right) + \frac{\partial}{\partial y} \left(\frac{\partial E_x}{\partial y} + \frac{\partial E_y}{\partial x} \right) = \frac{\partial E_x}{\partial z \partial z} + \frac{\partial E_z}{\partial x \partial z} + \frac{\partial E_x}{\partial y \partial y} + \frac{\partial E_y}{\partial x \partial y} \\
-i\omega\mu\sigma E_y &= \frac{\partial}{\partial z} \left(\frac{\partial E_y}{\partial z} + \frac{\partial E_z}{\partial y} \right) + \frac{\partial}{\partial x} \left(\frac{\partial E_x}{\partial y} + \frac{\partial E_y}{\partial x} \right) = \frac{\partial E_y}{\partial z \partial z} + \frac{\partial E_z}{\partial y \partial z} + \frac{\partial E_x}{\partial y \partial x} + \frac{\partial E_y}{\partial x \partial x} \\
-i\omega\mu\sigma E_z &= \frac{\partial}{\partial y} \left(\frac{\partial E_y}{\partial z} + \frac{\partial E_z}{\partial y} \right) + \frac{\partial}{\partial x} \left(\frac{\partial E_x}{\partial z} + \frac{\partial E_z}{\partial x} \right) = \frac{\partial E_y}{\partial z \partial y} + \frac{\partial E_z}{\partial y \partial y} + \frac{\partial E_x}{\partial z \partial x} + \frac{\partial E_z}{\partial x \partial x} \quad (4.5)
\end{aligned}$$

In order to solve above equations numerically, a finite difference approximation on a 3D staggered-grid (Yee, 1966) is utilized. On a staggered grid of dimensions $N_x \times N_y \times N_z$, the discretized tangential electric field vector components are specified on the cell edges (Figure 4.1). Accordingly, \mathbf{E} components that are parallel to the corresponding edges are defined at the centers of the cell edges, and the \mathbf{H} components that are orthogonal to corresponding faces are defined at the centers of the cell faces (Zhdanov, 2015). The superiority of the staggered grid formulation is that the corresponding electric and magnetic field components are continuous on the edges and faces of the homogenous cells, and therefore the staggered grid consists of two elementary loops: (1) the electric loop composed of four \mathbf{E} components parallel to the edges of one face of a cell and (2) the magnetic loop composed of four adjacent \mathbf{H} components (Figure 4.2) (Zhdanov, 2015).

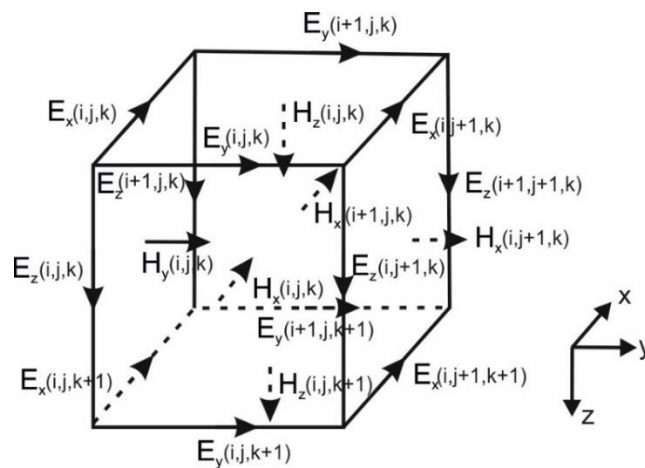


Figure 4.1. Staggered finite difference grid for the 3D MT forward problem. The partial differential equation is formulated in terms of \mathbf{E} specified on cell edges, which is the primary EM field component. The \mathbf{H} components that can be specified naturally on the cell faces are the secondary EM field in this numerical formulation (modified from Egbert and Kelbert, 2012; Kelbert *et al.*, 2014). The indices i, j and k are used to number the grid point in x, y and z directions, successively.

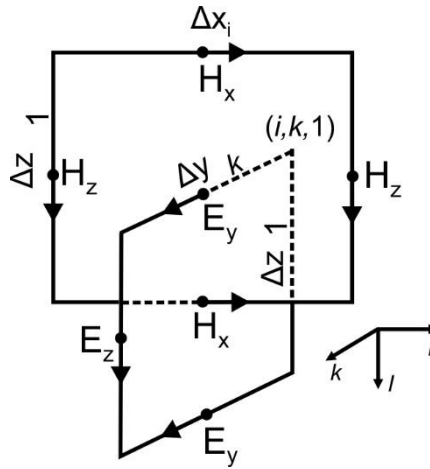


Figure 4.2. The electric and magnetic loops in a staggered grid in discretizing Maxwell's equations (modified from Zhdanov, 2015).

For instance, from the Faraday's law (2.30), we have

$$\mathbf{H} = \frac{1}{i\omega\mu} \nabla \times \mathbf{E} \quad (4.6)$$

Integrating the equation over a face S of the cell, bounded by a rectangular contour L , and utilizing Stokes' theorem, we obtain

$$\iint_S \mathbf{H} \cdot \mathbf{n} \, ds = \frac{1}{i\omega\mu} \iint_S (\nabla \times \mathbf{E}) \cdot \mathbf{n} \, ds = \frac{1}{i\omega\mu} \int_L \mathbf{E} \cdot \mathbf{t} \, dl \quad (4.7)$$

where \mathbf{n} is a unit vector normal to the cell face S , and \mathbf{t} is the corresponding unit vector tangential to the cell edges. L is the direction of \mathbf{n} and \mathbf{t} that are accordant with the corkscrew rule (i.e., with a corkscrew rotating in the direction \mathbf{t} , the point moves in the direction \mathbf{n}). The integrals in the Equation (4.7) can be evaluated approximately with respect to the discretized functions of the \mathbf{E} and \mathbf{H} . For node (i, k, l) , the x , y and z components of \mathbf{E} are specified at $(i + \frac{1}{2}, k, l)$, $(i, k + \frac{1}{2}, l)$ and $(i, k, l + \frac{1}{2})$, successively, and x , y and z components of \mathbf{H} are specified at $(i, k + \frac{1}{2}, l + \frac{1}{2})$, $(i + \frac{1}{2}, k, l + \frac{1}{2})$ and $(i + \frac{1}{2}, k + \frac{1}{2}, l)$, successively. For instance, at a cell that is parallel to the vertical plane- xz (Figure 4.2), the discrete form of the Equation (4.7) is

$$\begin{aligned}
i\omega\mu H_x \left(i, k + \frac{1}{2}, l + \frac{1}{2} \right) \Delta_{yk} \Delta_{zl} = & \left[E_y \left(i, k + \frac{1}{2}, l \right) - E_y \left(i, k + \frac{1}{2}, l + 1 \right) \Delta_{yk} \right] \\
& + \left[E_z \left(i, k + 1, l + \frac{1}{2} \right) - E_z \left(i, k, l + \frac{1}{2} \right) \Delta_{zl} \right] \quad (4.8)
\end{aligned}$$

Similarly, for other faces of an elementary cell, the discrete form of the equations can be obtained, and therefore, for the discretized values of the EM fields, a full system of equations can be set (Zhdanov, 2015).

In the staggered grid formulation, the primary field space S_P is described as the space of finite-dimensional cell edge vector fields. A typical element is represented by \mathbf{e} in this space. On the other hand, as shown in Figure 4.1, the magnetic fields, which provides the Equation 4.6 in continuous form, are specified on the cell faces. The dual field space S_D describes the discrete vector field space specified on cell faces. A typical element of that space is represented by \mathbf{h} . Then, the relation between \mathbf{E} and \mathbf{H} fields can be established in the staggered grid finite difference discretization that is utilized for the Equation 4.4 through

$$\mathbf{h} = (-i\omega\mu)^{-1} \mathbf{C} \mathbf{e} \quad (4.9)$$

where $\mathbf{C}: S_P \rightarrow S_D$ is the discrete approximation of the curl of cell edge vectors, and thus the Equation 4.4 in discrete form can be shown as below

$$[\mathbf{C}^\dagger \mathbf{C} + \text{diag}(i\omega\mu\sigma(\mathbf{m}))] \mathbf{e} = 0 \quad (4.10)$$

In Equation (4.10), $\text{diag}(\mathbf{v})$ represents a diagonal matrix with components of the vector \mathbf{v} on the diagonal. $\mathbf{C}^\dagger: S_D \rightarrow S_P$ is the discrete curl mapping interior cell face vectors to interior cell edges, and it is the adjoint of \mathbf{C} , which is related to appropriate inner products on the space S_D and S_P . The above equation derives equation systems only for the interior nodes although \mathbf{e} is the full solution vector that also contains boundary components. In order to define \mathbf{e} on the boundary and thus to complete determination of the discrete forward operator \mathbf{S}_m , additional equations are needed (Egbert and Kelbert, 2012).

The EM forward operator $\mathbf{f}(\mathbf{m})$ commonly includes two steps, solving Maxwell's equations numerically as constructing the appropriate boundary conditions and sources (where conductivity defined by the model parameter \mathbf{m}), and utilizing the resulted solutions to compute predicted data such as transfer functions. For the first, the numerical discretization of the frequency domain partial differential equation can be shown as

$$\mathbf{S}_m \mathbf{e} = \mathbf{b} \quad (4.11)$$

where \mathbf{b} defines boundary conditions and source terms for a specific EM problem. \mathbf{e} is the N_e -dimensional vector representing the discretized \mathbf{E} and/or \mathbf{H} fields. \mathbf{S}_m is an $N_e \times N_e$ coefficient matrix depending on the M -dimensional model parameter \mathbf{m} . \mathbf{e} represents interior and boundary components of the discrete solution vector, and \mathbf{b} involves boundary conditions needed for the solution and/or source terms (Egbert and Kelbert, 2012; Kelbert *et al.*, 2014). Then, the Equation (4.4) can be shown as below

$$\begin{bmatrix} \left(\frac{\partial}{\partial z \partial z} + \frac{\partial}{\partial y \partial y} \right) & \frac{\partial}{\partial x \partial y} & \frac{\partial}{\partial x \partial z} \\ \frac{\partial}{\partial y \partial x} & \left(\frac{\partial}{\partial z \partial z} + \frac{\partial}{\partial x \partial x} \right) & \frac{\partial}{\partial y \partial z} \\ \frac{\partial}{\partial z \partial x} & \frac{\partial}{\partial z \partial y} & \left(\frac{\partial}{\partial y \partial y} + \frac{\partial}{\partial x \partial x} \right) \end{bmatrix} \begin{bmatrix} E_x(x, y, z) \\ E_y(x, y, z) \\ E_z(x, y, z) \end{bmatrix} = \begin{bmatrix} b_x(x, y, z) \\ b_y(x, y, z) \\ b_z(x, y, z) \end{bmatrix} \quad (4.12)$$

Therefore, for the second step, the solution for the equation (4.10) can also be written as

$$\mathbf{e} = (\mathbf{S}_m)^{-1} \mathbf{b} \quad (4.13)$$

where \mathbf{S}_m is symmetric on a uniform grid. For more general case, because the EM operator is self-adjoint, we can express as

$$\mathbf{S}_m^T = \mathbf{V} \mathbf{S}_m \mathbf{V}^{-1} \quad (4.14)$$

where \mathbf{V} describes a diagonal matrix of integration volume elements for the discrete representation of the L_2 integral inner product on the model domain, and the equation $\mathbf{S}_m^T \mathbf{V} = \mathbf{V} \mathbf{S}_m$ is symmetric (not Hermitian). Thus, the forward solutions are generally computed as $\mathbf{e} = (\mathbf{V} \mathbf{S}_m)^{-1} \mathbf{V} \mathbf{b}$, and for the adjoint problem, it can be expressed with respect to the symmetrized inverse operator as $\mathbf{e} = (\mathbf{S}_m^T)^{-1} \mathbf{b} = \mathbf{V} (\mathbf{V} \mathbf{S}_m)^{-1} \mathbf{b}$ (Egbert and Kelbert, 2012). Accordingly, the \mathbf{e} describing the discrete field solution represents only the primary field (electric field). Then, the other dual field (magnetic field) is obtained from the primary field, and thus the EM impedances are computed from the relationship between two fields.

The predicted data are computed from the solution \mathbf{e} through

$$d_j = f_j(\mathbf{m}) = \psi_j(\mathbf{e}(\mathbf{m}), \mathbf{m}) \quad (4.15)$$

where ψ_j is function of the components of \mathbf{e} (and \mathbf{m}) (Kelbert *et al.*, 2014), and the derivative of the Equation (4.15) with respect to the model parameters gives the Jacobian (first-order derivative or Frechét derivative) matrix \mathbf{J} :

$$\mathbf{J}_{jk} = \frac{\partial f_j}{\partial m_k} \quad (4.16)$$

The computation of the first variation of the EM field is very important in inversion. For example, when we perturb the conductivity distribution $\sigma(x, y, z)$ within a volume of a 3D space, the perturbed electric field δE can be computed by perturbing the Equation (2.38) (Zhdanov, 2015):

$$\nabla^2 \delta E + i\omega\mu_0 \sigma \delta E = \begin{cases} -i\omega\mu_0 \sigma \delta E, & \mathbf{r} \in V \\ 0, & \mathbf{r} \notin V \end{cases} \quad (4.17)$$

Here, we describe the Green's function G_σ of the geoelectric model with conductivity $\sigma = \sigma(x, y, z)$. The Green's function depending upon the position of the points $\mathbf{r} = (x, y, z)$ and $\mathbf{r}' = (x', y', z')$ is characterized by the below equation

$$\nabla^2 G_\sigma(\mathbf{r}'|\mathbf{r}) + i\omega\mu_0\sigma G_\sigma(\mathbf{r}'|\mathbf{r}) = i\omega\mu_0\sigma\delta(\mathbf{r}' - \mathbf{r}) \quad (4.18)$$

which tends to zero at infinity. δ is the Dirac delta-function (Zhdanov, 2015).

The equations for the sensitivity matrix by differentiating the corresponding EM field can be found through the Faraday's and Ampere's laws:

$$\nabla \times \delta \mathbf{E} = -i\omega \mu \delta \mathbf{H} \quad (4.19)$$

$$\nabla \times \delta \mathbf{H} = \sigma \delta \mathbf{E} + \mathbf{J}^\delta \quad (4.20)$$

where $\delta\sigma$, is the conductivity variation, and $\delta\mathbf{E}$ and $\delta\mathbf{H}$ are the corresponding \mathbf{E} and \mathbf{H} field variations, respectively. $\mathbf{J}^\delta = \delta\sigma\mathbf{E}$ is the excess electric current within a domain of the perturbed conductivity (Zhdanov, 2015).

Thus, the Equation (4.4) can be written as

$$\nabla \times \nabla \times \delta \mathbf{E} + i\omega \mu \sigma \delta \mathbf{E} = i\omega \mu \delta \sigma \mathbf{E} \quad (4.21)$$

The numerical discretization of the equation can be shown as follows

$$(\mathbf{D}_s + i\omega \mu \boldsymbol{\sigma}) \delta \mathbf{e} = i\omega \mu \delta \boldsymbol{\sigma} \mathbf{e} \quad (4.22)$$

Where $\delta\boldsymbol{\sigma}$ is the diagonal matrix of the perturbed conductivities in the cells of the grid. \mathbf{e} is the $3N$ vector (N is the number of the mesh nodes) of the electric field. \mathbf{D}_s is the complex symmetric $3N \times 3N$ matrix of coefficients for the system, which is independent of frequency (ω) and a sparse matrix having 13 nonzero entries per row. $\boldsymbol{\sigma}$ and $\boldsymbol{\mu}$ are the diagonal matrices of the conductivities and permeabilities in the cells of the grid, respectively. It is assumed that perturbations of magnetic permeability μ is zero (Zhdanov, 2015).

Accordingly, the Equation (4.5) can be written as follows

$$\begin{bmatrix} \left(\frac{\partial}{\partial z \partial z} + \frac{\partial}{\partial y \partial y}\right) & \frac{\partial}{\partial x \partial y} & \frac{\partial}{\partial x \partial z} \\ \frac{\partial}{\partial y \partial x} & \left(\frac{\partial}{\partial z \partial z} + \frac{\partial}{\partial x \partial x}\right) & \frac{\partial}{\partial y \partial z} \\ \frac{\partial}{\partial z \partial x} & \frac{\partial}{\partial z \partial y} & \left(\frac{\partial}{\partial y \partial y} + \frac{\partial}{\partial x \partial x}\right) \end{bmatrix} \begin{bmatrix} \frac{\partial E_x(x,y,z)}{\partial \sigma} \\ \frac{\partial E_y(x,y,z)}{\partial \sigma} \\ \frac{\partial E_z(x,y,z)}{\partial \sigma} \end{bmatrix} = \begin{bmatrix} i\omega\mu\delta\sigma E_x \\ i\omega\mu\delta\sigma E_y \\ i\omega\mu\delta\sigma E_z \end{bmatrix} \quad (4.23)$$

When we try to calculate the sensitivity of the \mathbf{E} to the perturbation of the conductivity $\delta\sigma$ in one cell V_q , we need to substitute for \mathbf{e} a vector \mathbf{e}_q having only three non-zero components, which are $E_{i+\frac{1}{2},k+\frac{1}{2},l+\frac{1}{2}}^x, E_{i+\frac{1}{2},k+\frac{1}{2},l+\frac{1}{2}}^y, E_{i+\frac{1}{2},k+\frac{1}{2},l+\frac{1}{2}}^z$, in cell V_q :

$$(\mathbf{D}_s + i\omega\mu\sigma)\delta\mathbf{e}^{(q)} = i\omega\mu\delta\sigma\mathbf{e}_q \quad (4.24)$$

We express by $\delta\mathbf{e}_j^{(q)}$ the element of the vector $\delta\mathbf{e}^{(q)}$ related to the j th receiver position. It can be described that an electric field which is generated by an electric source $\delta\sigma\mathbf{e}_q$ situated in the cell V_q . The Jacobian matrix \mathbf{J} is composed of the components $\frac{\delta\mathbf{e}_j^{(q)}}{\delta\sigma}$, thus computing the matrix requires forward modeling solutions for each parameter (Zhdanov, 2015).

The calculation of the first variation (Jacobian) is also important to solve the minimization problem. Search for a minimizer of penalty function utilizing \mathbf{J} is iterative. With the NLCG scheme, the gradient of the Equation (4.3) in terms of variations in model parameters \mathbf{m} must be evaluated:

$$\left. \frac{\partial\theta}{\partial\mathbf{m}} \right|_{\mathbf{m}_n} = -2\mathbf{J}^T\mathbf{r} + 2\mathbf{v} + \mathbf{m}_n \quad (4.25)$$

where \mathbf{m}_n is the model parameter at the n th iteration, and $\mathbf{r} = \mathbf{d} - \mathbf{f}(\mathbf{m}_n)$ is the data residual. Then, the gradient in the model space is utilized to find a new conjugate search direction. The penalty function along this direction that utilizes a line search requiring at most a few evaluations of the forward operator is minimized, and then the gradient is

recomputed. The same computational steps needed for solving the linearized equations are essentially used again (Egbert and Kelbert, 2012; Başokur, 2015).

4.2. Three-Dimensional Inversion of the Gediz Graben Data Set

As shown by the phase tensor analyses, most of the Gediz Graben data set shows a dominant 3D character. Thus, a 3D inversion was carried out for the data set. The 3D electrical resistivity models were computed with the 3D MT code ModEM (Meqbel 2009; Egbert and Kelbert, 2012; Kelbert *et al.*, 2014). In total, 253 MT sites have been taken into account from the different areas (A, B, C and D) of the Gediz Graben. Full impedance tensor data in the period range of 0.001-1000 s were inverted. The data set was reduced to five periods per decade, resulting thirty-one periods. All inversions were penalized against a homogenous half-space of 100 Ωm . The topography obtained from a digital elevation model, the SRTM (Shuttle Radar Topography Mission, NASA) data with 90 m resolution were included into the 3D inversion mesh. The initial models (piori models as well) were constructed via the commercial 3D-Grid software provided by Lemnis Geoscience. Multiple inversion runs, which includes all components of impedance tensor with different initial models, grid discretization, smoothing parameters and error floors, were conducted in order to get plausible resistivity models for the Gediz Graben geothermal areas. In the following section, the details of inversions and preferred 3D models will be presented.

4.3. Three-Dimensional Inversion Results

4.3.1. Area A

Area A is located in the western part of the Gediz Graben, which covers an area containing the Salihli geothermal field (Figure 3.6). MT data from 74 sites in this area were used for 3D modeling. The model consists of 84x66x55 cells in the x, y and z directions, resulting in a total cell number of 304920. Taking into account the distance between two closest sites (238 m), the core area of the initial model was divided into 119 m blocks in the horizontal directions. 8 blocks were added to the boundary of the mesh. The lateral size of padding cells was increased logarithmically by a factor of 1.3. In the vertical direction, 21 layers having a thickness of 100 m each and followed by 34 layers with logarithmically increasing thicknesses by a factor of 1.2 to the bottom of the model at 297 km were used, and the topography varying between 595 m above sea level at the central Menderes Massif and 89 m at the Gediz Garben were adopted in 3D inversion. Isotropic covariance matrix was used with 0.2 at every direction. The error floor was set as 5% value of $|Z_{xy}Z_{yx}|^{1/2}$. After 75 iterations, an acceptable overall RMS misfit of 2.45 was achieved. In order to demonstrate the spatial extents of main conductivity anomalies, the final 3D model in Figure 4.3 is shown in perspective view.

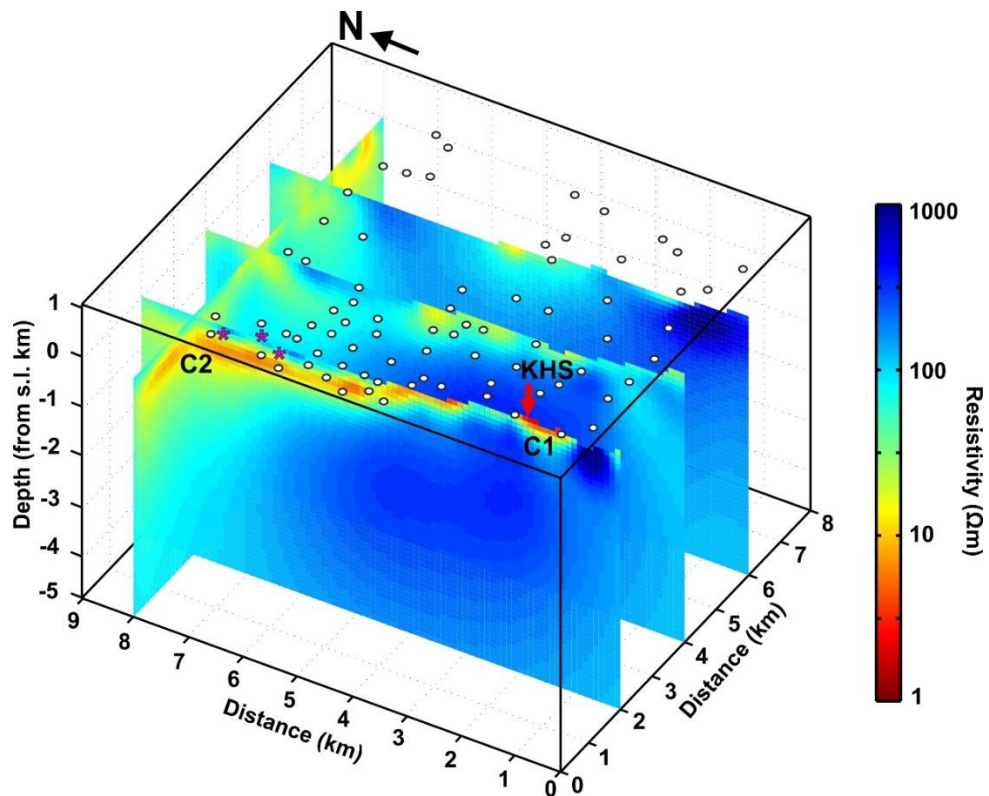


Figure 4.3. 3D perspective view displaying vertical north-south slices through the model and site locations (white dots) at surface. The red arrow shows the location of the Kurşunlu hot spring (KHS). The pink asterisks represent hot water wells. Conductive features are labelled with C.

Figures 4.4 and 4.5 show preferred 3D inversion results in plain view at four selected depths 0.25, 0.5, 1 and 2 km and cross-sections along preferred profiles, respectively. A shallow conductive zone (C1) ($\sim 10 \Omega\text{m}$) is present beneath the KHS at a depth of 0.3 km, which is attributed to the reservoir of the hot spring. Another conductive zone (C2) with a resistivity lower than $10 \Omega\text{m}$ also imaged beneath the Gediz Graben. The most striking aspect of this conductive structure is the fact that its morphology follows the topography (Figure 4.3). This conductive structure has been associated with the hydrothermal clay alteration zone that occurs in the conventional geothermal systems. Apart from these low resistivity anomalies, in the deepest part of the model, a structure of high resistivity ($>250 \Omega\text{m}$) is imaged. This resistive basement is explained by high-grade metamorphic rocks of the Menderes core complex (Menderes Massif), and its thickness and resistivity value decreases towards the graben (Figure 4.5). Furthermore, it is evident from cross sections that the GDF is a lateral boundary between the resistive basement and conductive sedimentary cover.

Similarly, the MGBF flanking the graben to the south is a clear boundary between metamorphic basement and lithological units of the graben.

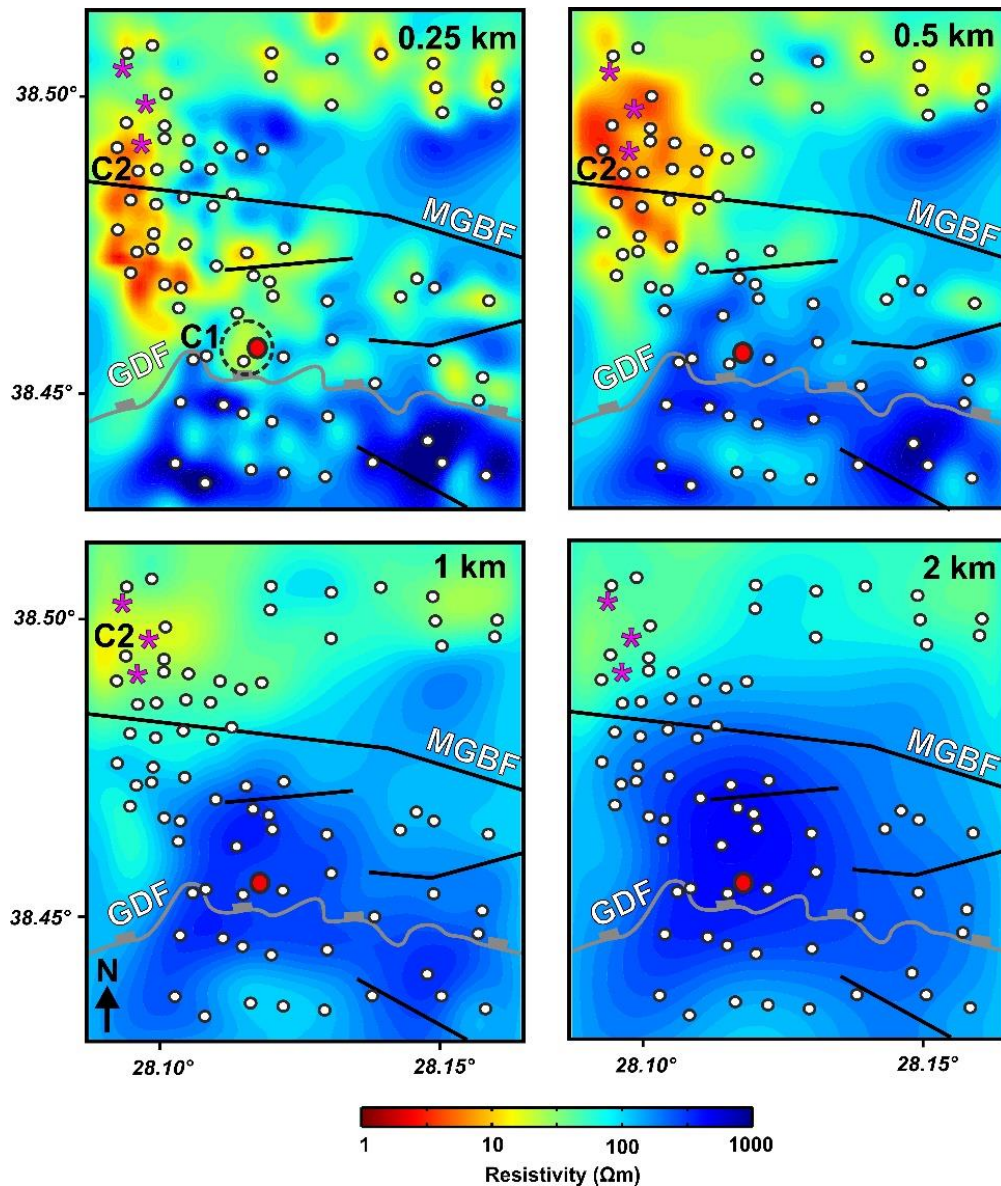


Figure 4.4. Resistivity depth sections derived from 3D model for 0.25, 0.5, 1 and 2 km. The white dots show the site locations. The pink asterisks show the location of hot water wells. The red dot marks the location of the KHS. The gray lines mark the GDF, and black lines indicate surface trace of normal faults. Conductive features are labelled with C. Dashed circle (C1) represents reservoir of the KHS. MGBF: Main Graben-Bounding Fault.

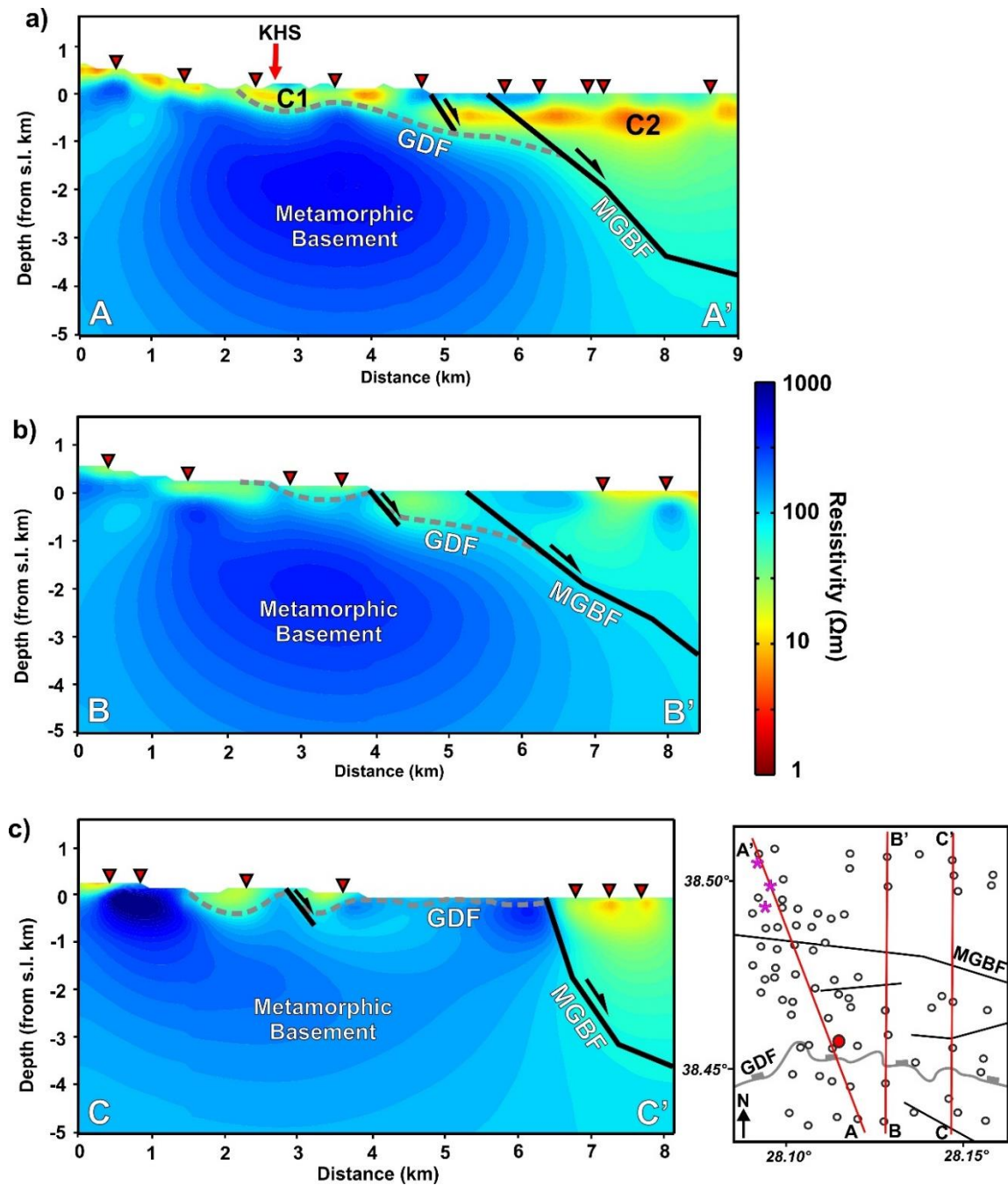


Figure 4.5. Resistivity distribution with depth along preferred profiles A-A', B-B' and C-C'. The location map of the preferred profiles is shown at the bottom right corner. The location of KHS is shown as red arrow. Red triangles show the location of MT sites. The gray dashed lines mark the GDF, and black lines represent normal faults existing in the study area (modified from Çiftçi and Bozkurt, 2009a; 2009b). Conductive features are labelled with C.

Figure 4.6 shows observed data and 3D model responses of all used data components for representative sites A1100 and A1500. Site S1100 is situated near the MGBF, and A1500 is located near the production well (SAN-3) shown as pink asterisk in the insert. The data fits of on-diagonal components of impedance tensor is poor due to scattering nature of the data.

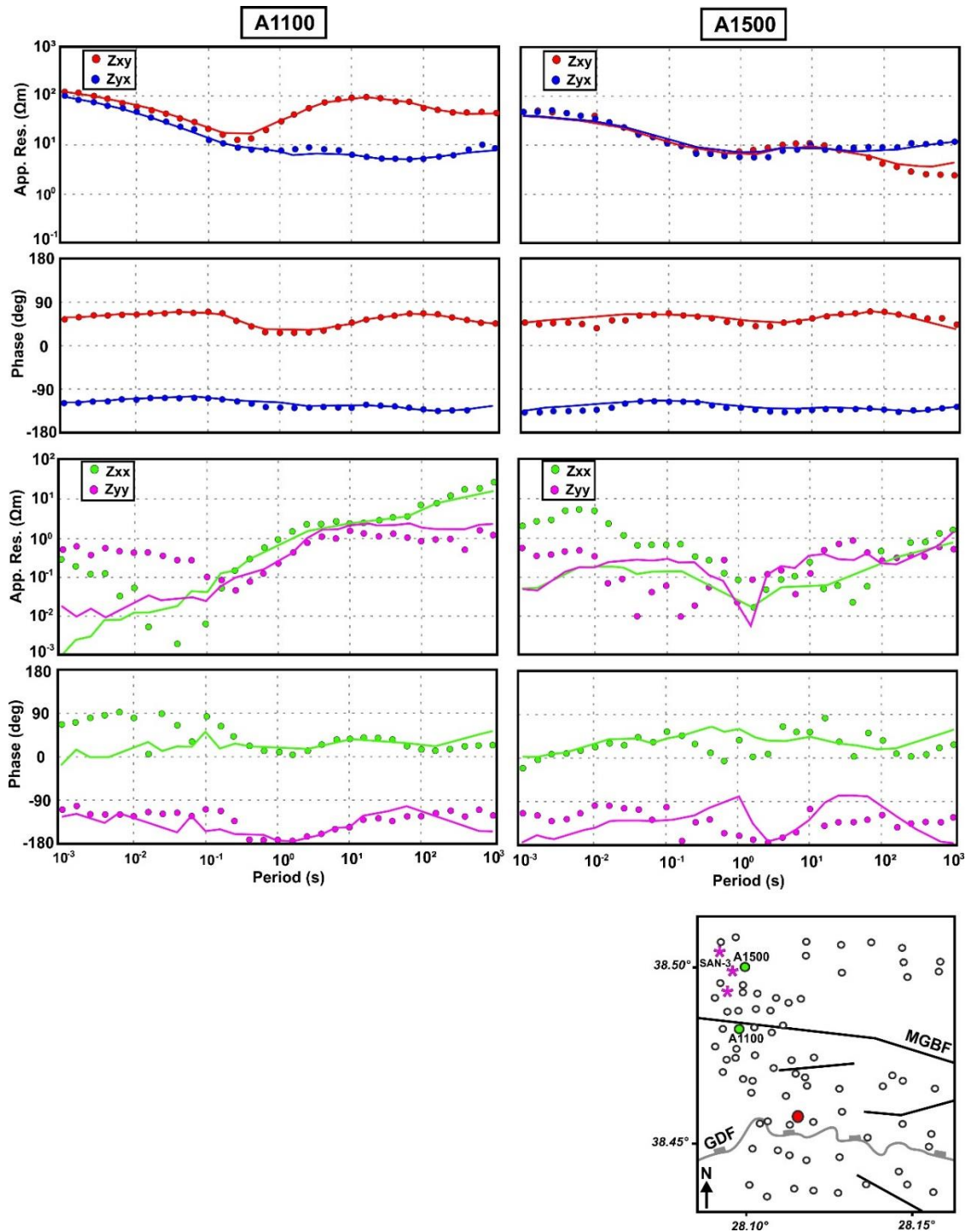


Figure 4.6. Measured data (dots) and 3D responses (lines) for two representative sites shown as green dots in the insert. Apparent resistivity and phase derived from off-diagonal (XY and YX) and diagonal (XX and YY) components of impedance tensor.

Figure 4.7 displays normalized Root Mean Square (nRMS) values for all components of the impedance tensor in order to describe the quality of the 3D models produced for

investigation area A. While achieved RMS values at each site for four components of impedance tensor are acceptable, they show higher values for off-diagonal components of the impedance tensor when compared with the on-diagonal components.

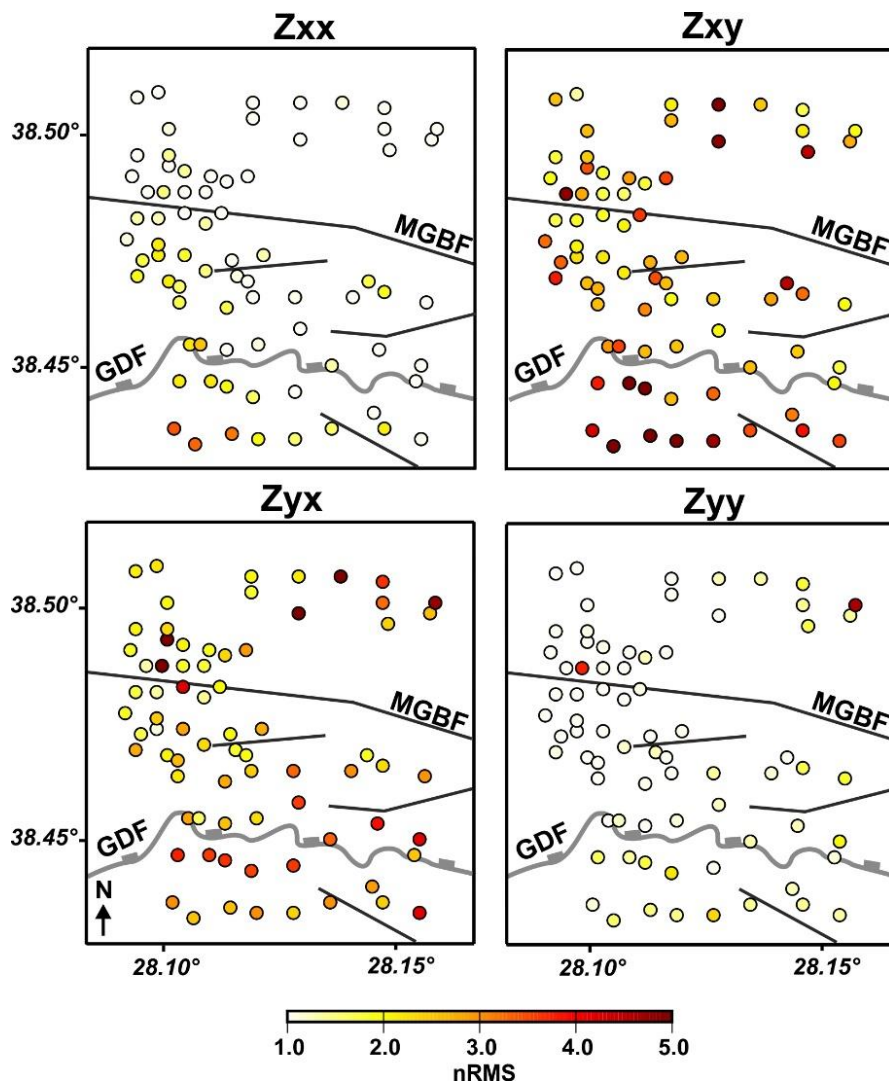


Figure 4.7. Data misfits at each site for four components of the impedance tensor (Z_{xx} , Z_{xy} , Z_{yx} , Z_{yy}). MT sites are marked by circles with color representing the nRMS misfit.

4.3.2. Area B

Area B close to the Alaşehir geothermal field is located in the southern part of the Gediz Graben (Figure 3.6). MT data from 27 sites in this area were used for 3D modeling. The model consists of 68x68x55 cells in the x, y and z directions, respectively. Taking into account the distance between two closest sites (339 m), the core area of the initial model was divided into 169.5 m blocks in the horizontal directions. 20 blocks were added to the boundary of the mesh. The lateral size of padding cells was increased logarithmically by a factor of 1.3. In the vertical direction, the thickness of the first layer was selected as 25 m and the cell sizes were set with logarithmically increasing thicknesses by a factor of 1.2 to the bottom of the model at 222 km. The topography varying between 822 m and 281 m above sea level at the central Mendere Massif were considered. Isotropic covariance matrix was used with 0.3 at every direction. The error floor was set as 5% value of $|Z_{xy}Z_{yx}|^{1/2}$. After 72 iterations, an acceptable overall RMS misfit of 1.86 was achieved. The final 3D model in Figure 4.8 is shown in perspective view.

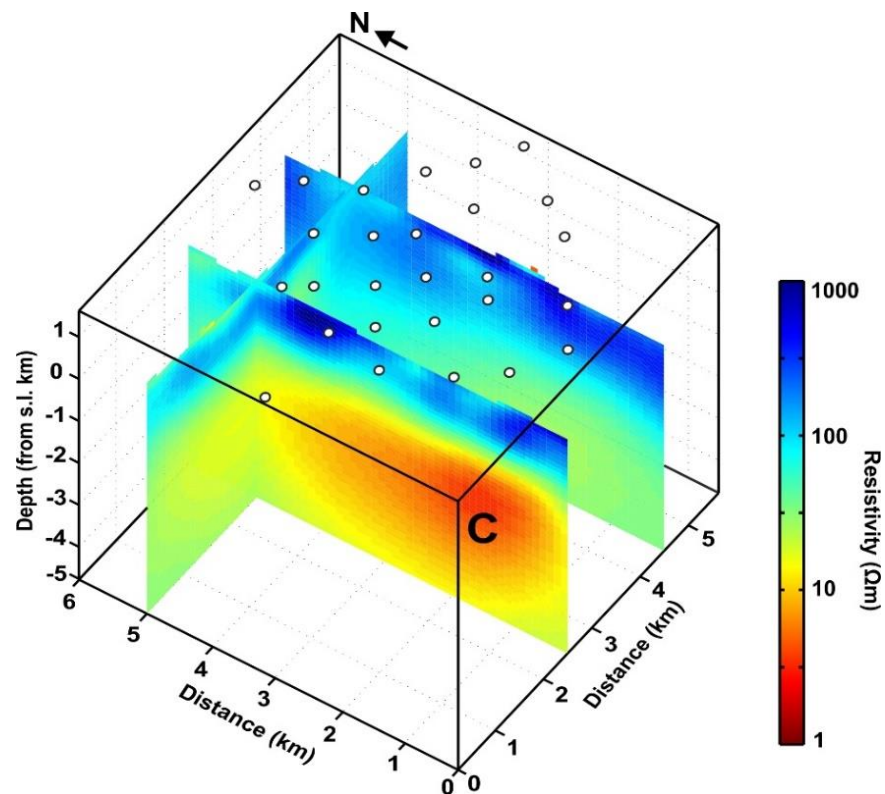


Figure 4.8. 3D perspective view displaying conductor C through the model and site locations (white dots) at surface.

Figures 4.9 and 4.10 show preferred 3D inversion results in plain view at four selected depths 0.25, 0.5, 2 and 4 km and cross-sections along preferred profiles, respectively. The most striking feature in the model is the existence of the NE-SW directed low resistivity zone (C) interpreted as a fractured hydrothermal system carrying geothermal fluids, buried at a depth range of 2-2.5 km and disappeared below at a depth range of 4-4.5 km. The very high resistivities ($>250 \Omega\text{m}$) above this conductive zone can be explained by metamorphic rocks of the Menderes Massif. The contrast between the conductive and resistive zones characterizes the orientation of the north dipping low-angle GDF that controls structural features of the area. Moreover, the Girelli segment of the GDF (named as Girelli Fault) shows a good correlation between electrical resistivity distribution of the area. The uppermost shallow conductive zones are also associated with the lower Miocene-Plio-Pleistocene sedimentary rocks of the Gediz Graben basin.

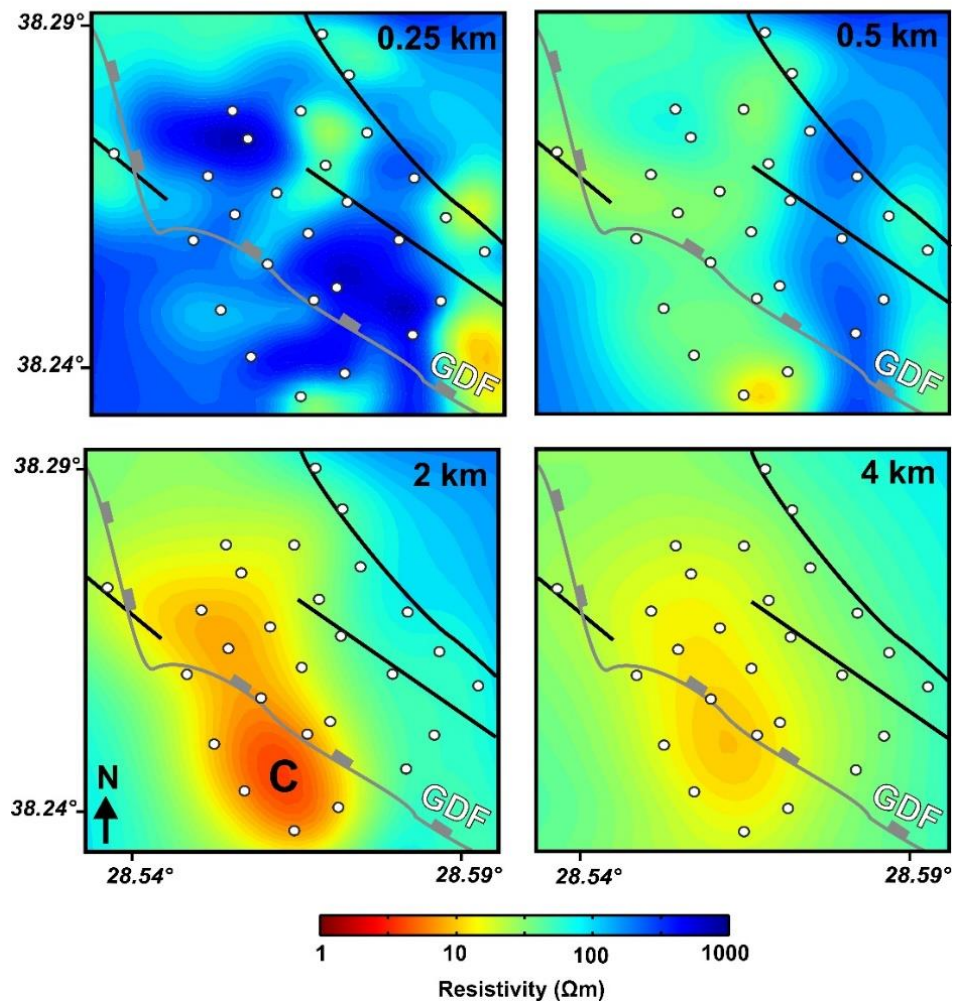


Figure 4.9. Resistivity depth sections derived from 3D model for 0.25, 0.5, 2 and 4 km. The white dots show the site locations. The gray lines mark the GDF, and black lines represent normal faults. Conductive feature is labelled with C.

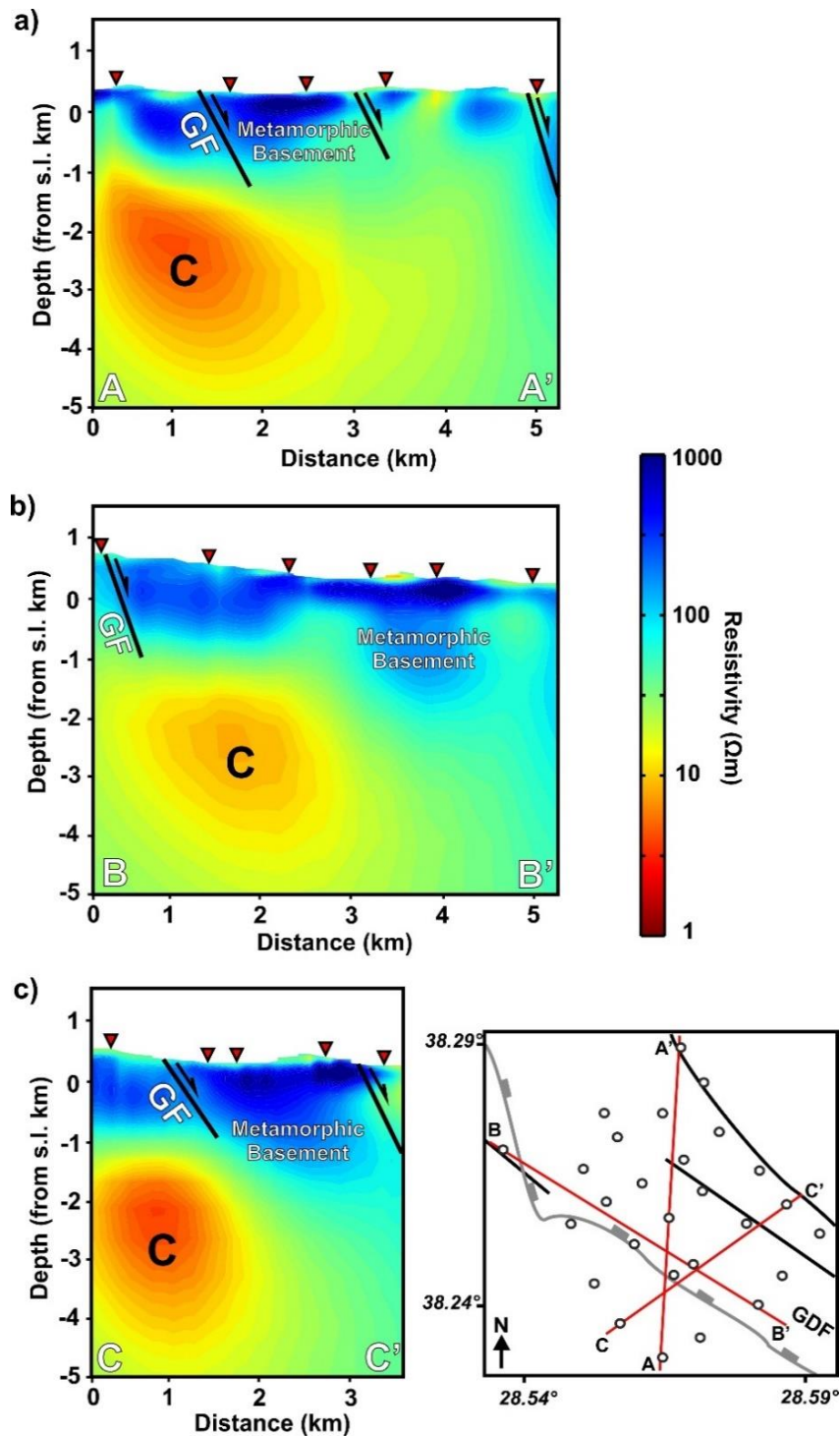


Figure 4.10. Resistivity distribution with depth along preferred profiles A-A', B-B' and C-C'. The location map of the preferred profiles is shown at the bottom right corner. Red triangles show the location of MT sites. The gray lines mark the GDF, and black lines represent normal faults existing in the study area (modified from Çiftçi and Bozkurt, 2009b). Conductive feature is labelled with C.

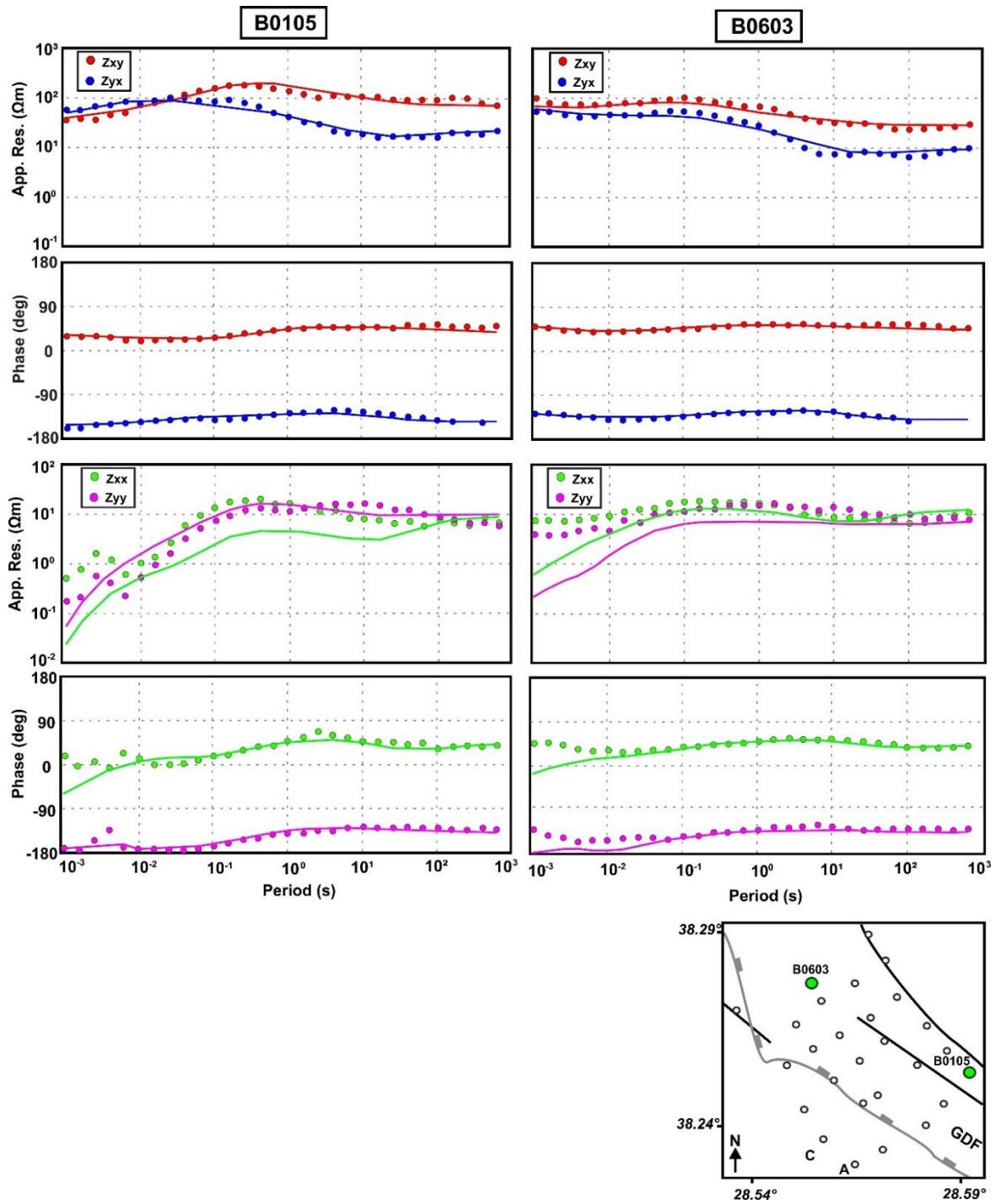


Figure 4.11. Measured data (dots) and 3D responses (lines) for two representative sites shown as green dots in the insert. Apparent resistivity and phase derived from off-diagonal (XY and YX) and diagonal (XX and YY) components of impedance tensor.

Figure 4.11 shows observed data and 3D model responses of all used data components for representative sites B0105 and B0603. The response of 3D model at all components of the impedance tensor show good agreement with observed data. However, data fits get worse for apparent resistivity of on-diagonal components. Figure 4.12 displays nRMS values of individual sites for all components of the impedance tensor. Overall, the corresponding data misfits at each site for all components of the impedance tensor are acceptable.

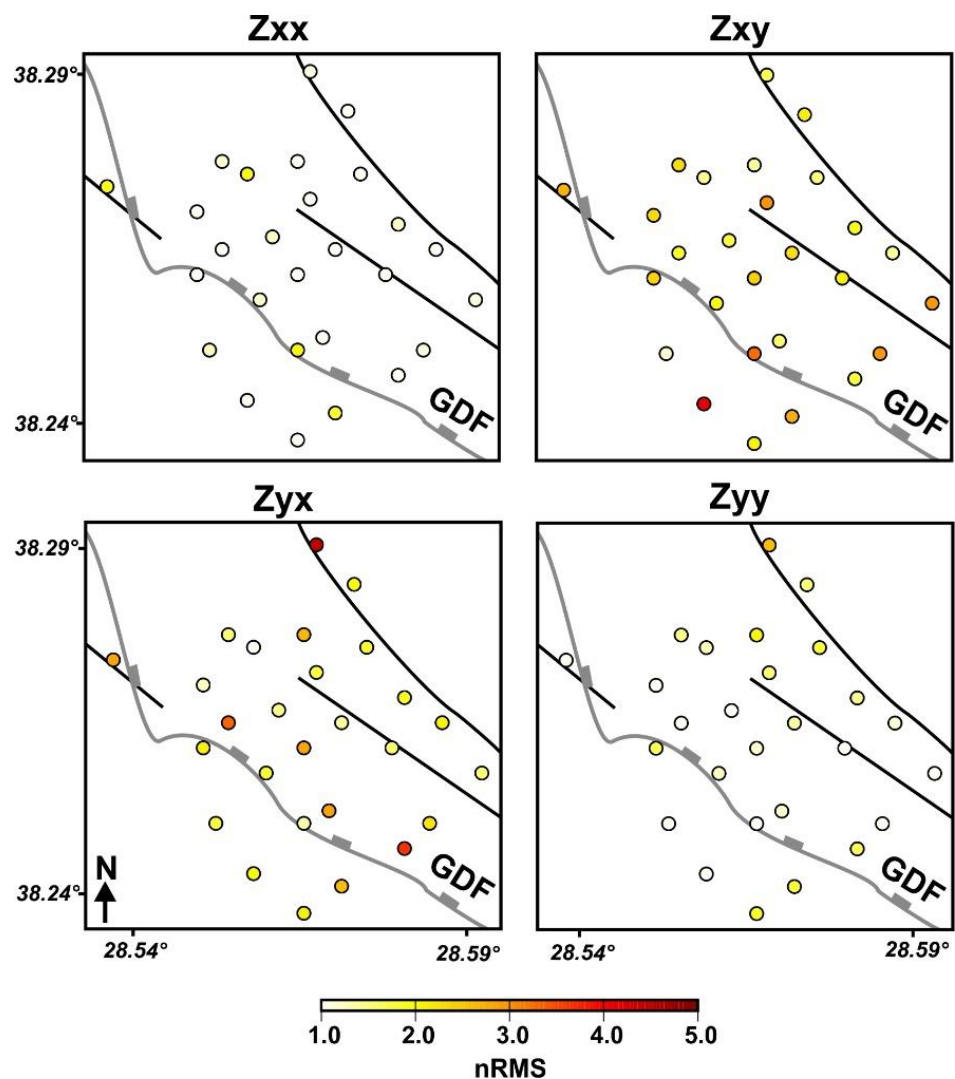


Figure 4.12. Data misfits at each site for four components of the impedance tensor (Z_{xx} , Z_{xy} , Z_{yx} , Z_{yy}). MT sites are marked by circles with color representing the nRMS misfit.

4.3.3. Area C

Area C located inside the Gediz Graben, which possesses the largest alluvial area in the Gediz Basin, and contains data from 78 MT sites. Model core of area C consists of 94x66x55 cells with a horizontal size of 150x150 m. 10 padding cells were also appended to the boundary of the mesh in horizontal directions, and the size of the padding cells were increased logarithmically by a factor of 1.3. 21 layers having a thickness of 100 m each and followed by 34 layers with logarithmically increasing thicknesses by a factor of 1.2 to the bottom of the model 297 km were used in the vertical direction, and the topography (from 216 m to 143 m above sea level) was considered. Isotropic covariance matrix was used with 0.2 at every direction. The error floor was set as 5% value of $|Z_{xy}Z_{yx}|^{1/2}$. An acceptable overall RMS misfit of 1.39 was achieved after 40 iterations. The final 3D model in Figure 4.13 is shown in perspective view.

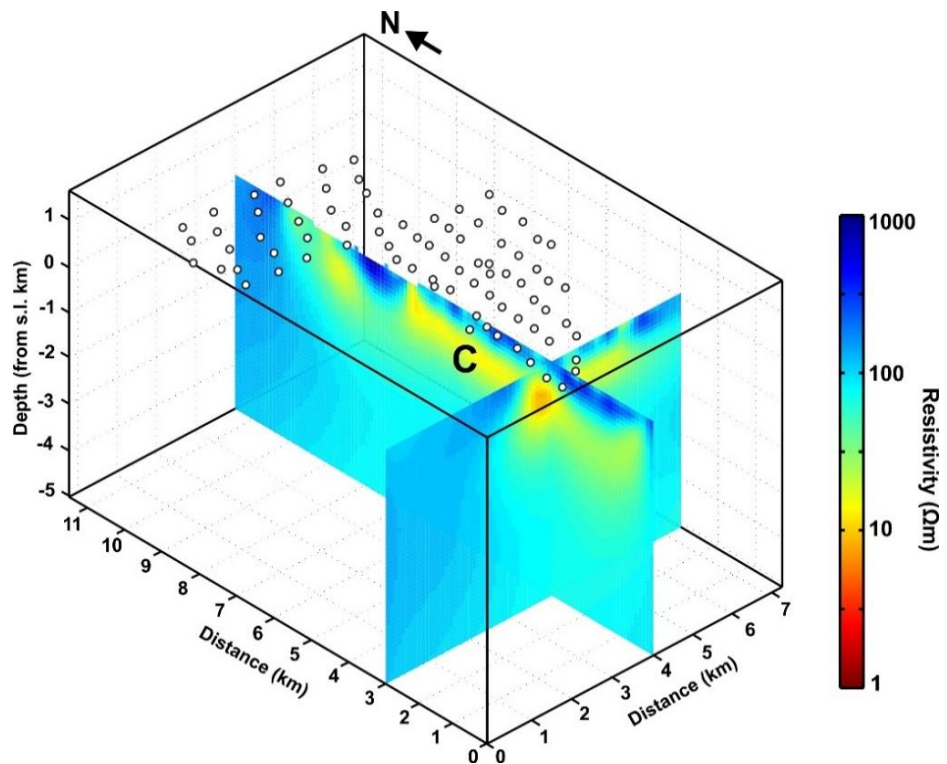


Figure 4.13. 3D perspective view displaying conductor C through the model and site locations (white dots) at surface. Conductive layer is labelled with C.

Figures 4.14 and 4.15 show preferred 3D inversion results in plain view at four selected depths 0.25, 0.5, 1 and 3 km and cross-sections along preferred profiles, successively. The most striking feature in the 3D model is the existence of a conductive structure (C) imaged beneath the Gediz Graben. This conductive structure ($\sim 20 \Omega\text{m}$) may be attributed to an existing reservoir or directly associated with the sedimentary fill of the graben, and below 2.5-3 km begins to disappear. A resistivity structure ($>100 \Omega\text{m}$) in the eastern part of the model is also obvious, which is associated with high-grade metamorphic rocks of the Menderes core complex. The most superficial part of the model has high resistivity values (250-500 Ωm) associated with alluviums containing basalts and conglomerates while very low resistivities at shallow depths corresponds to unconsolidated Quaternary alluvial deposits of the Gediz Graben.

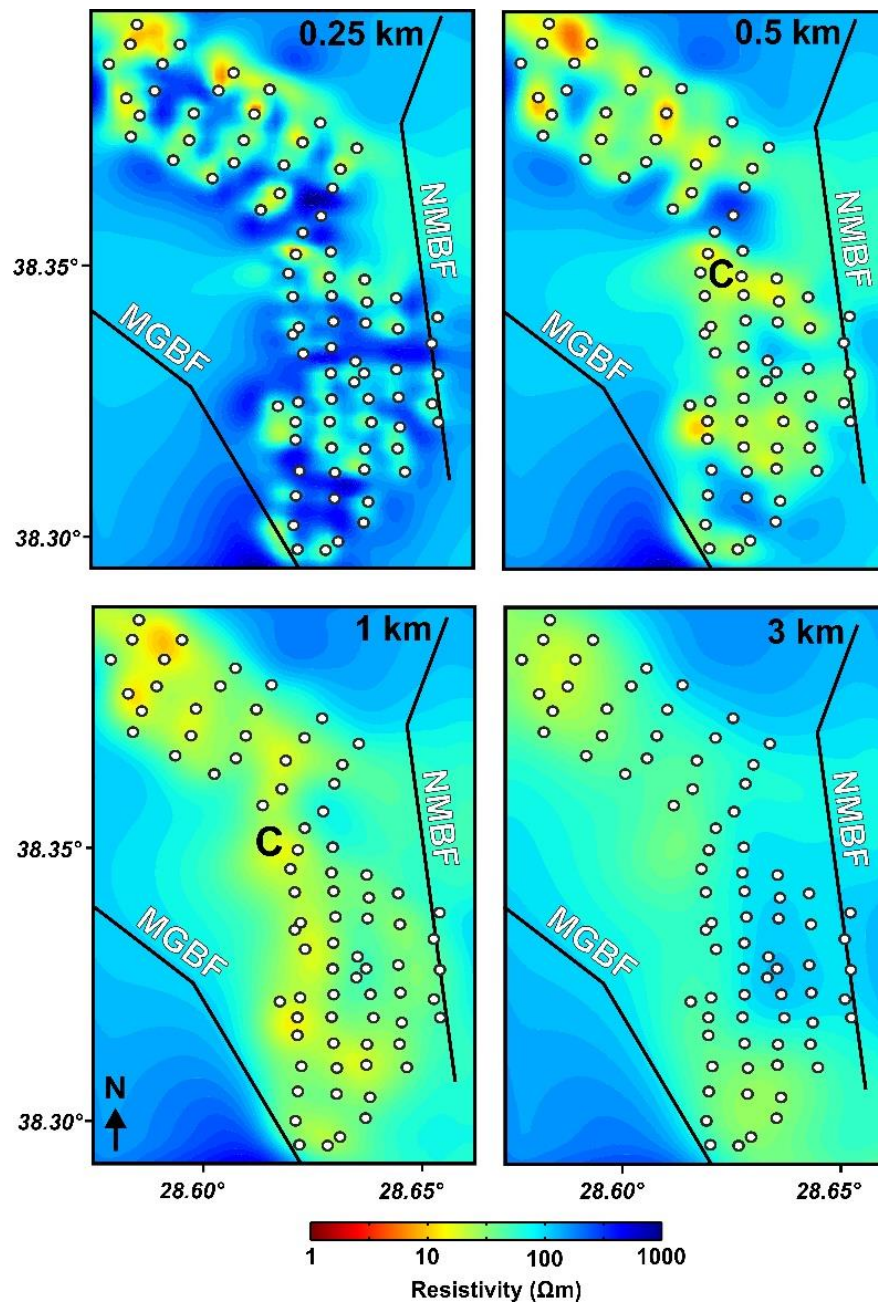


Figure 4.14. Resistivity depth sections derived from 3D model for 0.25, 0.5, 1 and 3 km. The white dots show the site locations. The black lines indicate surface trace of normal faults. Conductive features are labelled with C. MGBF: Main Graben-Bounding Fault, NMBF: Northern Margin Bounding Fault.

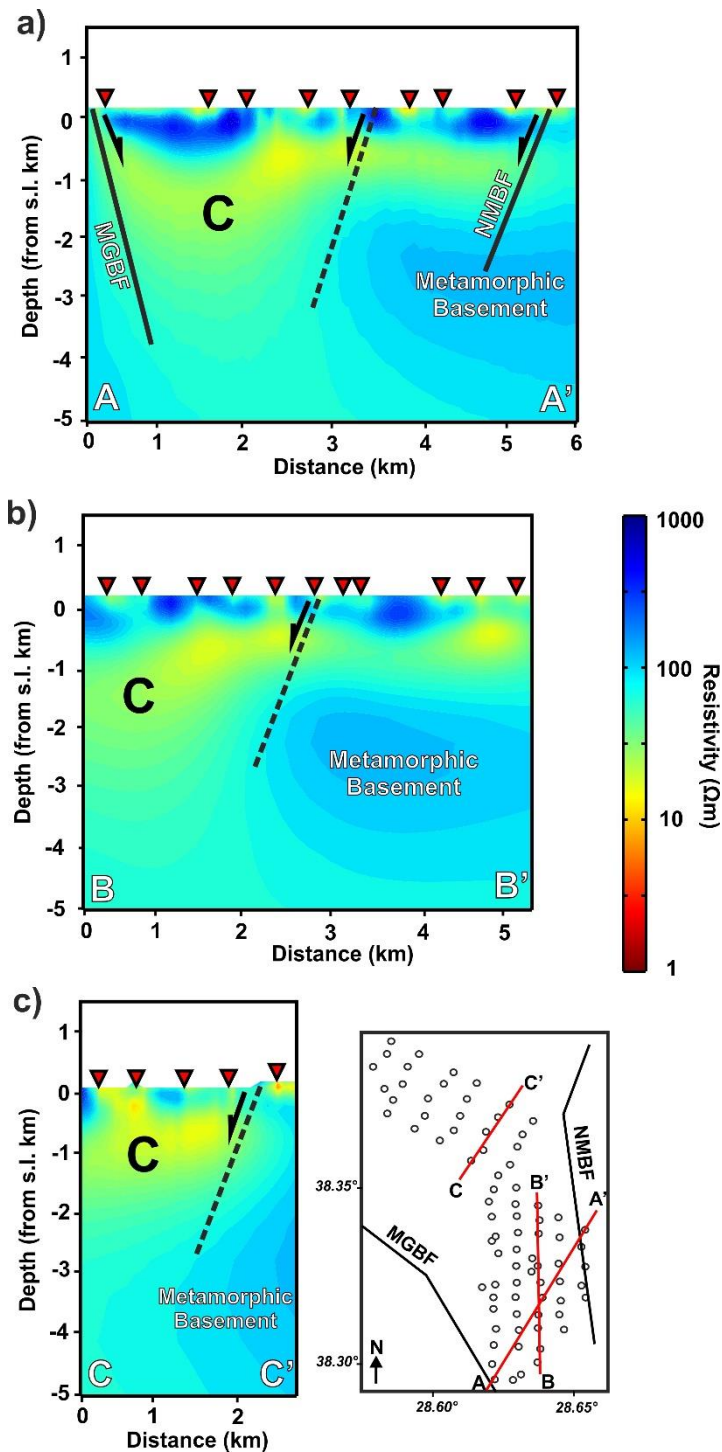


Figure 4.15. Resistivity distribution with depth along preferred profiles A-A', B-B' and C-C'. The location map of the preferred profiles is shown at the bottom right corner. Red triangles show the location of MT sites. The black lines represent normal faults existing in the study area (modified from Çiftçi and Bozkurt, 2009a; 2009b). Conductive features are labelled with C.

Figure 4.16 shows observed data and 3D model responses of all used data components for representative sites B8722 and B9122. The impedance phase for the Z_{yy} component at site B8722 leaves the quadrant at 0.1 s. The response of 3D model at all components of the impedance tensor shows good agreement with observed data.

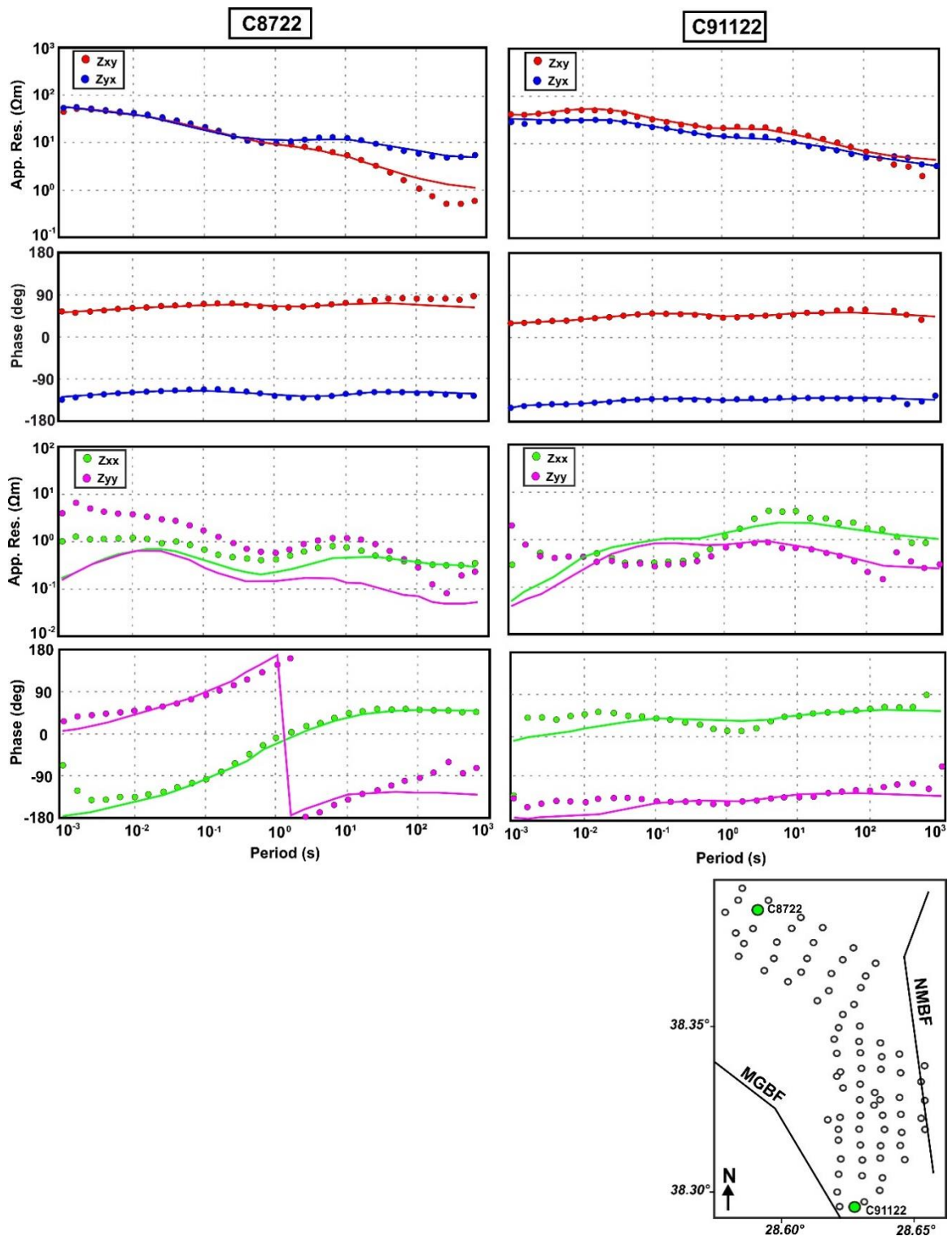


Figure 4.16. Measured data (dots) and 3D responses (lines) for two representative sites shown as green dots in the insert. Apparent resistivity and phase derived from off-diagonal (XY and YX) and diagonal (XX and YY) components of impedance tensor.

Figure 4.17 displays nRMS values of individual sites for all components of the impedance tensor. Overall, the corresponding data misfits at each site for all components of the impedance tensor are acceptable. The nRMS distribution at individual sites demonstrates that sites located at the southern side of the investigation area B are generally well fitted.

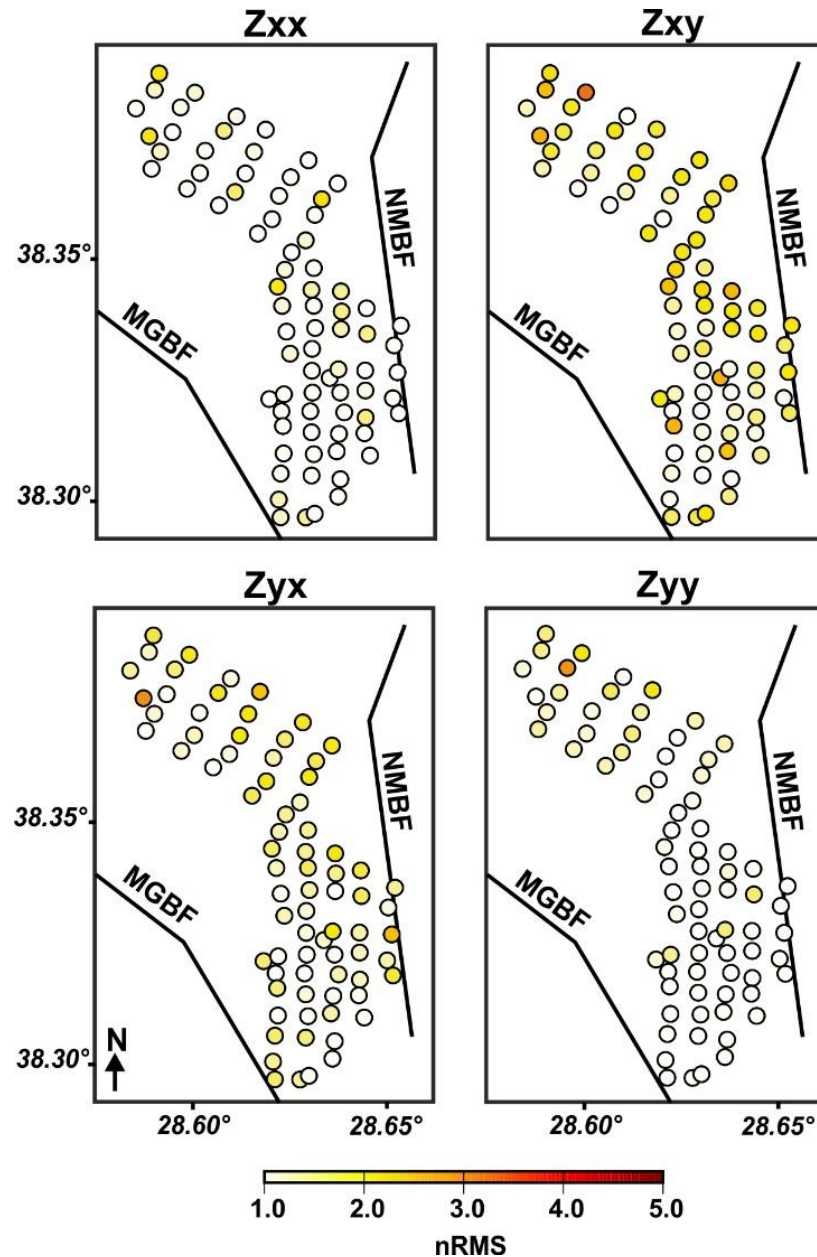


Figure 4.17. Data misfits at each site for four components of the impedance tensor (Z_{xx} , Z_{xy} , Z_{yx} , Z_{yy}). MT sites are marked by circles with color representing the nRMS misfit.

4.3.4. Area D

Area D is located in the eastern end of the Gediz Graben (Figure 3.6). MT data from 74 sites in this area were used for 3D modeling. The model contains $90 \times 72 \times 55$ cells in the x, y and z directions, successively. The core area of the initial model was divided into 200 m blocks in the horizontal directions. 10 blocks were added to the boundary of the mesh. The lateral size of padding cells was increased logarithmically by a factor of 1.3. In the vertical direction, 21 layers having a thickness of 100 m each and followed by 34 layers with logarithmically increasing thicknesses by a factor of 1.2 to the bottom of the model 297 km were utilized, and the topography (from 375 m to 179 m above sea level) was considered. Isotropic covariance matrix was used with 0.2 at every direction. The error floor was set as 5% value of $|Z_{xy}Z_{yx}|^{1/2}$. After 43 iterations, an acceptable overall RMS misfit of 1.58 was achieved. The final model in Figure 4.18 is shown in perspective view.

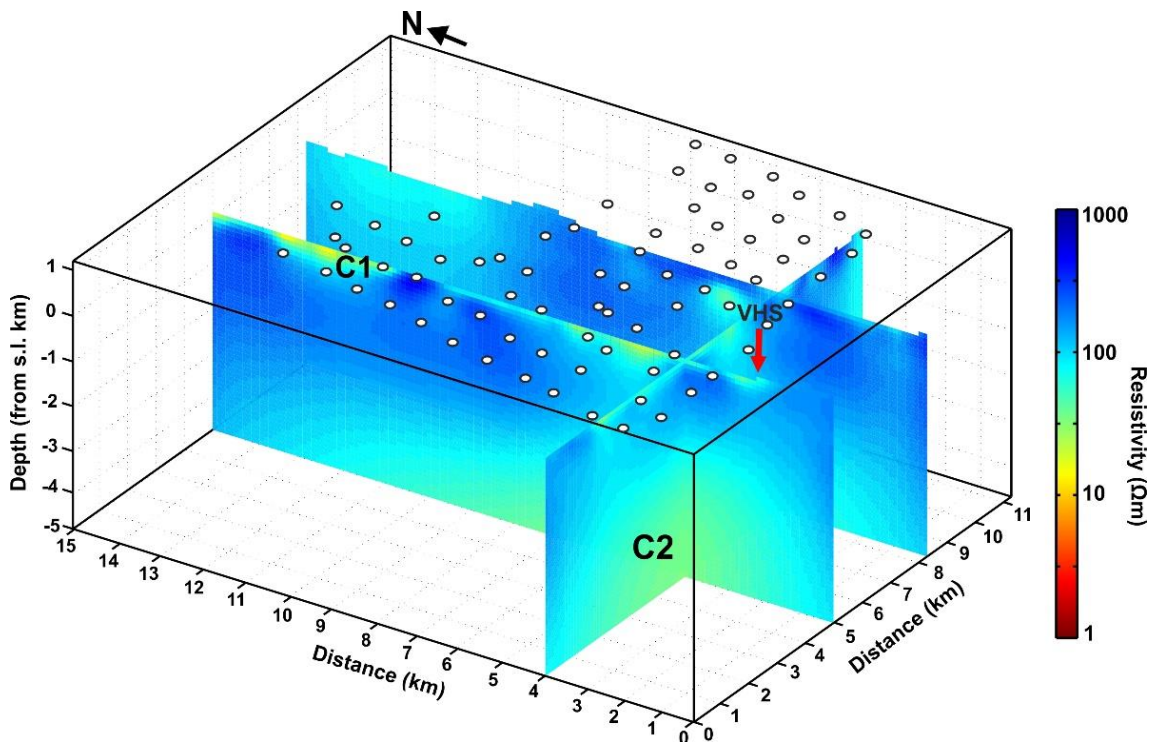


Figure 4.18. 3D perspective view displaying conductors C1 and C2 through the model and site locations (white dots) at surface. The red arrow shows the location of the Veli Çeşmesi hot spring (VHS). Conductive features are labelled with C.

Figures 4.19 and 4.20 demonstrate preferred 3D inversion results in plain view at four selected depths 0.25, 0.5, 1 and 3 km and cross-sections along preferred profiles, respectively. A shallow conductive structure (C1) ($\sim 20 \Omega\text{m}$) presents beneath the Gediz Graben, which has been associated with Quaternary alluviums existing in the eastern end of the graben and the lower Miocene-Plio-Pleistocene sedimentary rocks of the graben basin. Another structure (C2) having low-medium values of resistivity (30-50 Ωm) at 3 km begins to appear in the southern margin of the graben. This conductive structure may be attributed to a zone of hydrothermal fluid circulation existing in the southern margin of the Gediz Graben. The very high resistivities beneath the shallow conductive zones are also explained by metamorphic rocks of the Menderes Massif.

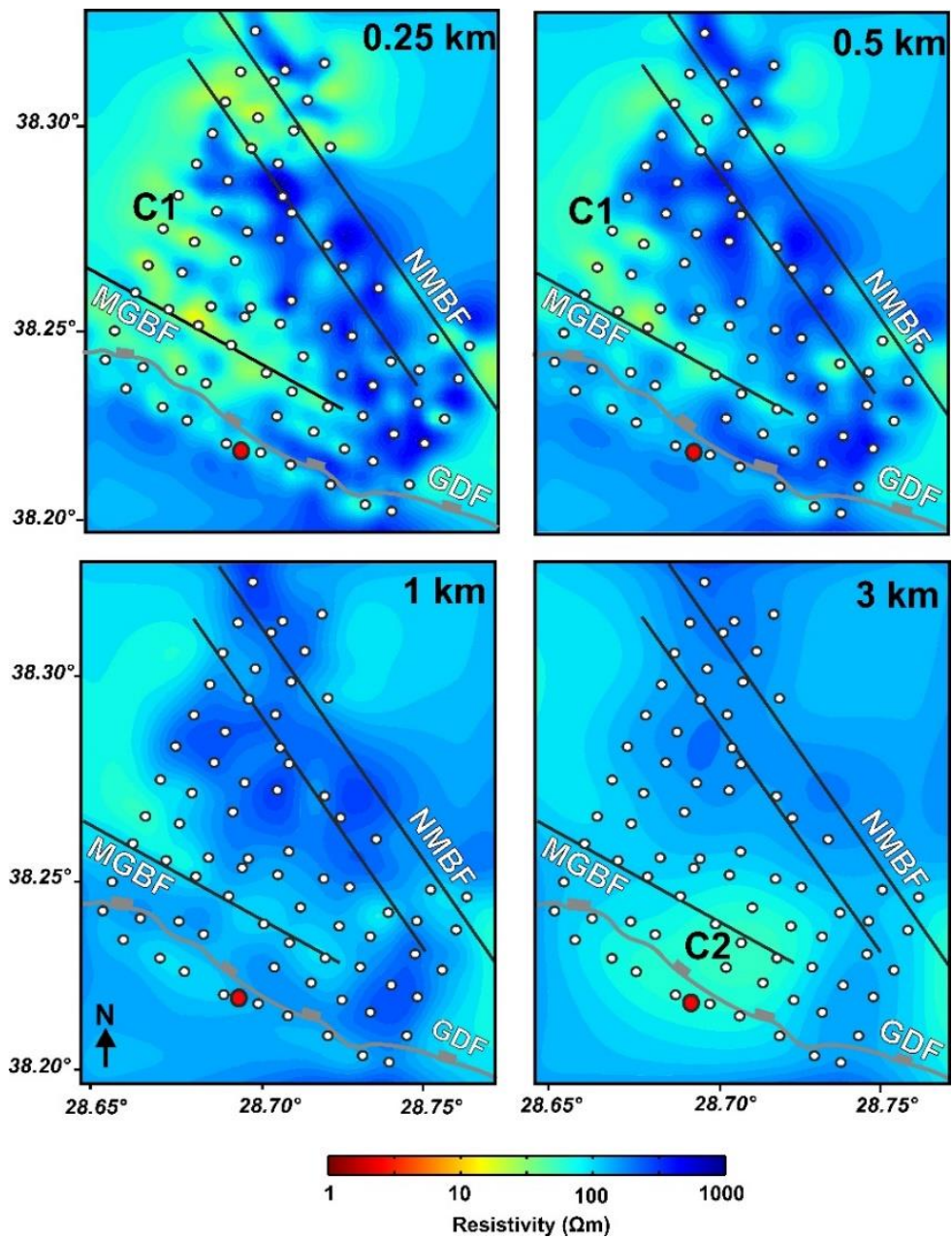


Figure 4.19. Resistivity depth sections derived from 3D model for 0.25, 0.5, 1 and 3 km. The white dots show the site locations. The red dot marks the location of the VHS. The gray lines mark the GDF, and black lines represent normal faults. Conductive features are labelled with C. MGBF: Main Graben-Bounding Fault, NMBF: Northern Margin Bounding Fault.

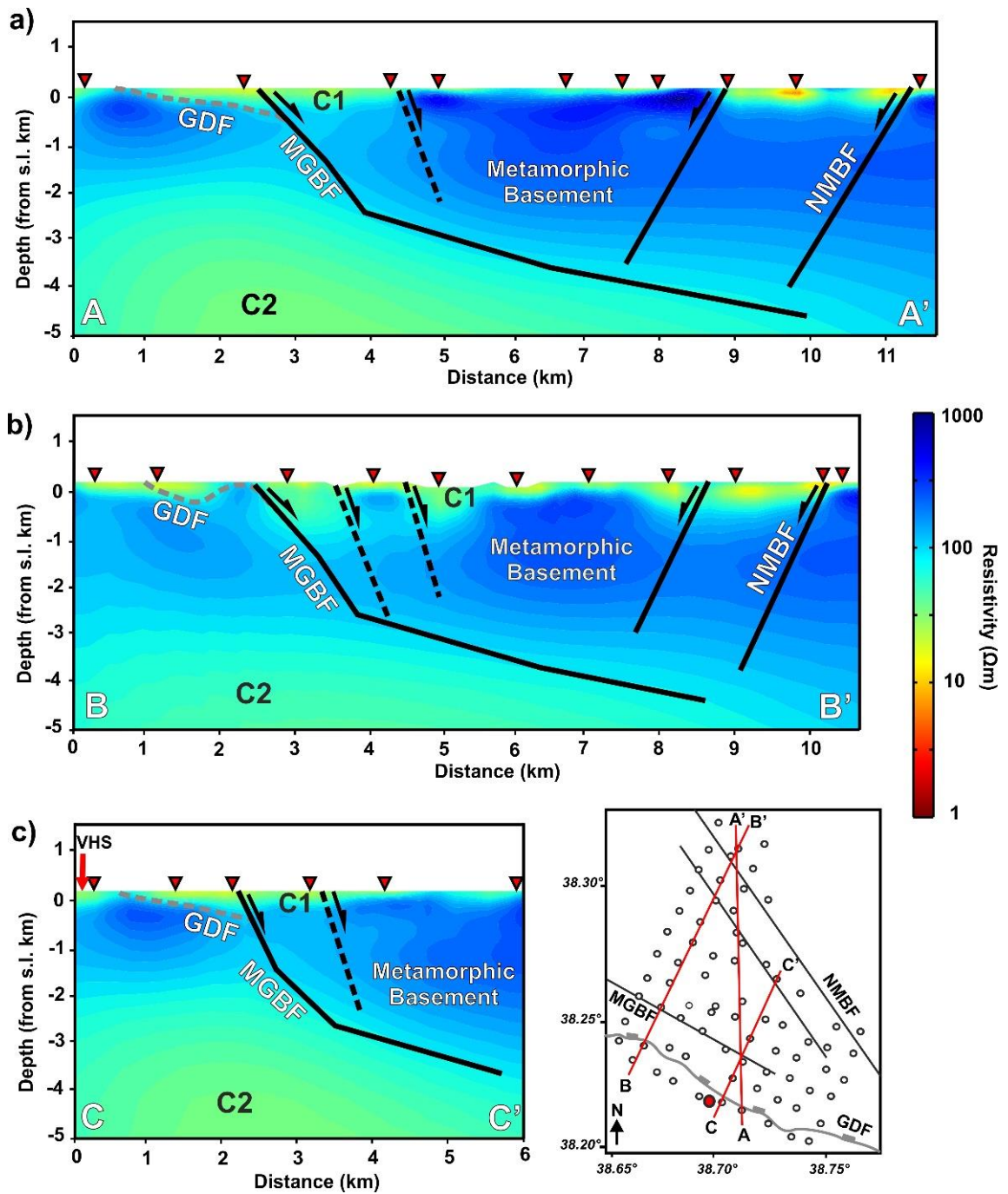


Figure 4.20. Resistivity distribution with depth along preferred profiles A-A', B-B' and C-C'. The location map of the preferred profiles is shown at the bottom right corner. Red triangles show the location of MT sites. The gray lines mark the GDF, and black lines represent normal faults existing in the study area (modified from Çiftçi and Bozkurt, 2009a; 2009b). Conductive features are labelled with C.

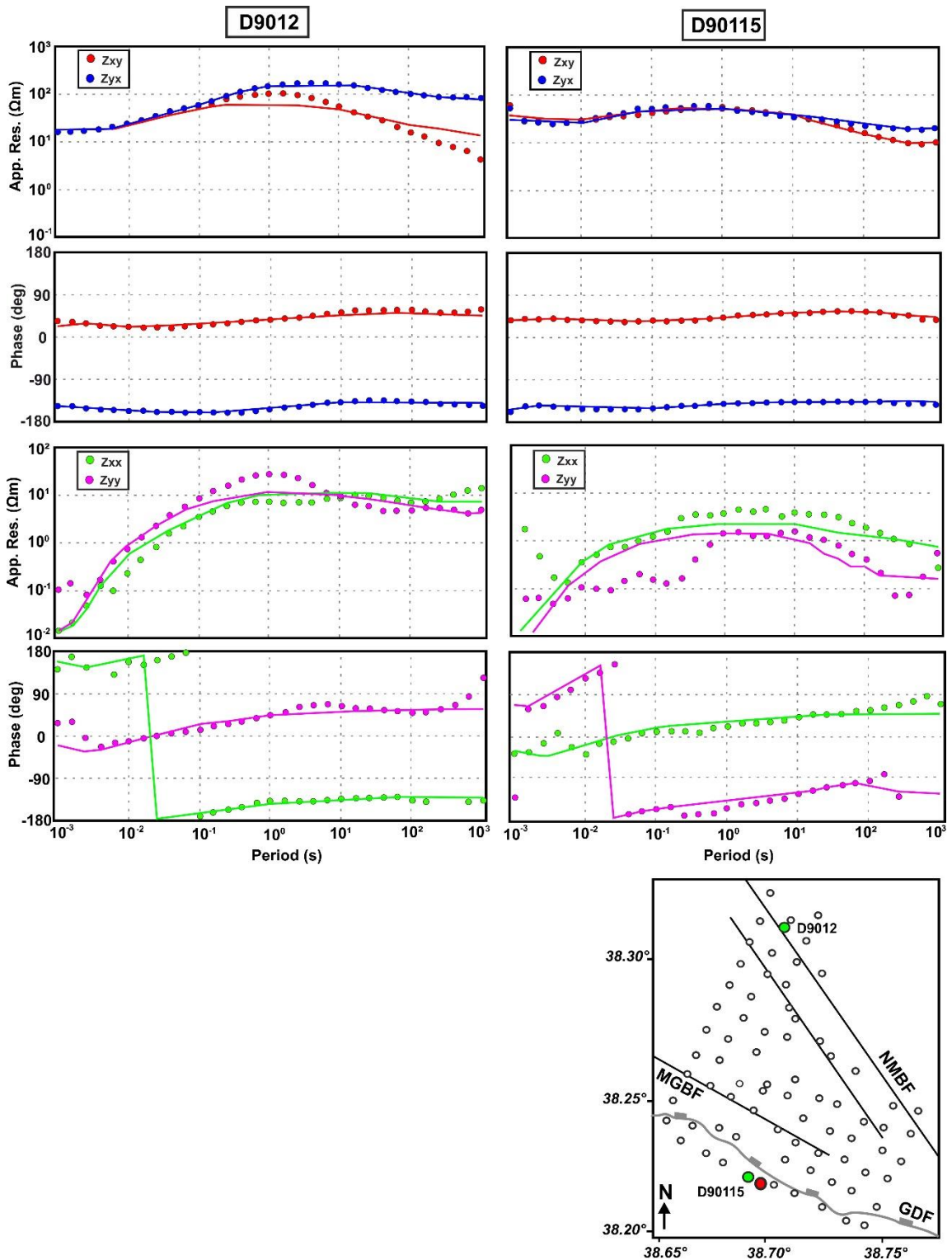


Figure 4.21. Measured data (dots) and 3D responses (lines) for two representative sites shown as green dots in the insert. Apparent resistivity and phase derived from off-diagonal (XY and YX) and diagonal (XX and YY) components of impedance tensor.

Figure 4.21 shows observed data and model responses of all used data components for representative sites D9012 and D90115. Sites D9012 and D90115 are located above the NMBF and near the GDF, respectively. The nRMS misfit of the inversion result at individual sites in the area C is also shown in Figure 4.22. Therefore, the response of 3D model at all components of the impedance tensor show good agreement with observed data.

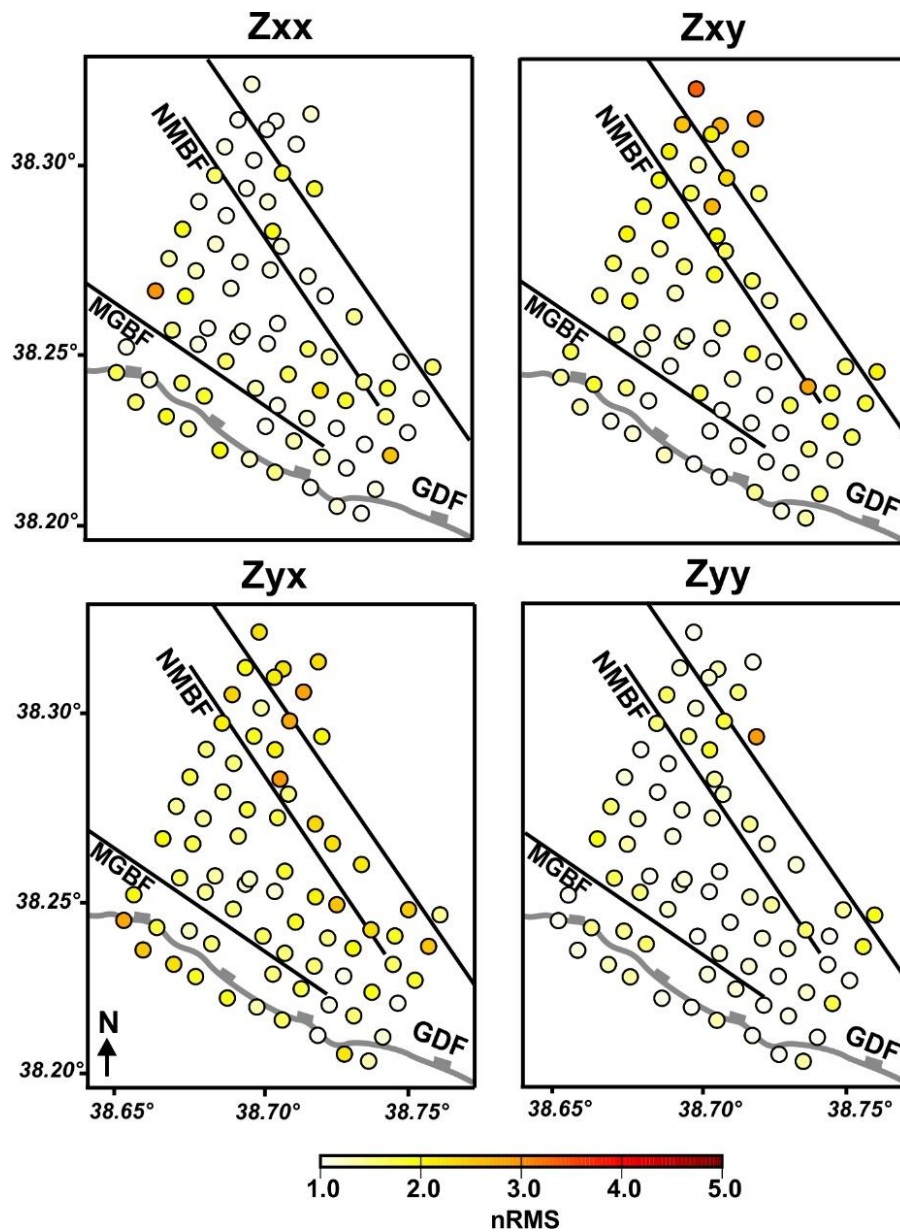


Figure 4.22. Data misfits at each site for four components of the impedance tensor (Z_{xx} , Z_{xy} , Z_{yx} , Z_{yy}). MT sites are marked by circles with color representing the nRMS misfit.

5. SENSITIVITY AND SYNTHETIC TESTS

5.1. Sensitivity Tests

In order to seek the validity and dimensions of the prominent conductivity anomalies characterized in 3D models for four different areas (A, B, C and D) of the Gediz Graben, several tests were made by utilizing forward and inverse modeling in addition to multiple inversion runs involving different starting models, data weighting, smoothing and grid discretization. Thus, the sensitivity of the conductive features was tested to verify that these zones are not artificially generated by inappropriate inverse modeling implementations.

5.1.1. Test for Area A

The first test in the investigation area A was made to examine the reservoir depth of the KHS, which is coincident with the conductive feature C1 shown in Figures 4.3, 4.4 and 4.5. To do this test, a block with constant resistivity of 500 Ωm starting at three different depths 30 m (test-3), 130 m (test-2) and 230 m (test-1) and terminating at the base of the model was introduced into the preferred 3D resistivity model (Figure 5.1a). In order to seek the sensitivity of data against these artificially inserted blocks, 3D forward modeling experiments was performed. The RMS values between data and forward responses in this test are 4.20 for test-3, 4.0 for test-2 and 4.0 for test-1. According to the forward responses shown in Figure 5.1b for an exemplary site (A0503) situated on top of the C1, the presence of the inserted resistive bodies has a strong impact on the data fits. The comparison of the MT responses of the preferred 3D model with the responses of modified model, it can be proposed that the MT data do not verify the presence of the inserted resistive bodies at corresponding depths. Thus, the base of the conductive zone C1 depicted in 3D model is valid as a value approximately 300 m.

Another test (test-4) was conducted to examine the sensitivity of the most significant high conductivity feature C2 that is nearly horizontal and slightly NW-SE trending beneath the Gediz Graben at a depth of 250-800 m (Figures 4.3, 4.4 and 4.5). To do this test, a moderately conductive (50 Ωm) block was introduced to the preferred 3D model (Figure

5.2a). Subsequently, a second inversion was performed using the modified model as starting model. The inserted block was fixed during the inversion. The test was performed taking into account the same error floor assigned during the original inversion previously described in Section 4.3.1. The overall misfit of the second inversion is 3.26. This is slightly larger than the original inversion (2.45) and indicates more data with different resolution capabilities. Additionally, based on the model responses of modified model shown in Figure 5.2b, the MT data cannot be fit in the inversion with the inserted moderately resistive block, and any model fitting the data with the same smoothing factor (0.2) of the original inversion cannot be found. Consequently, MT data are not compatible with this artificially inserted structure.

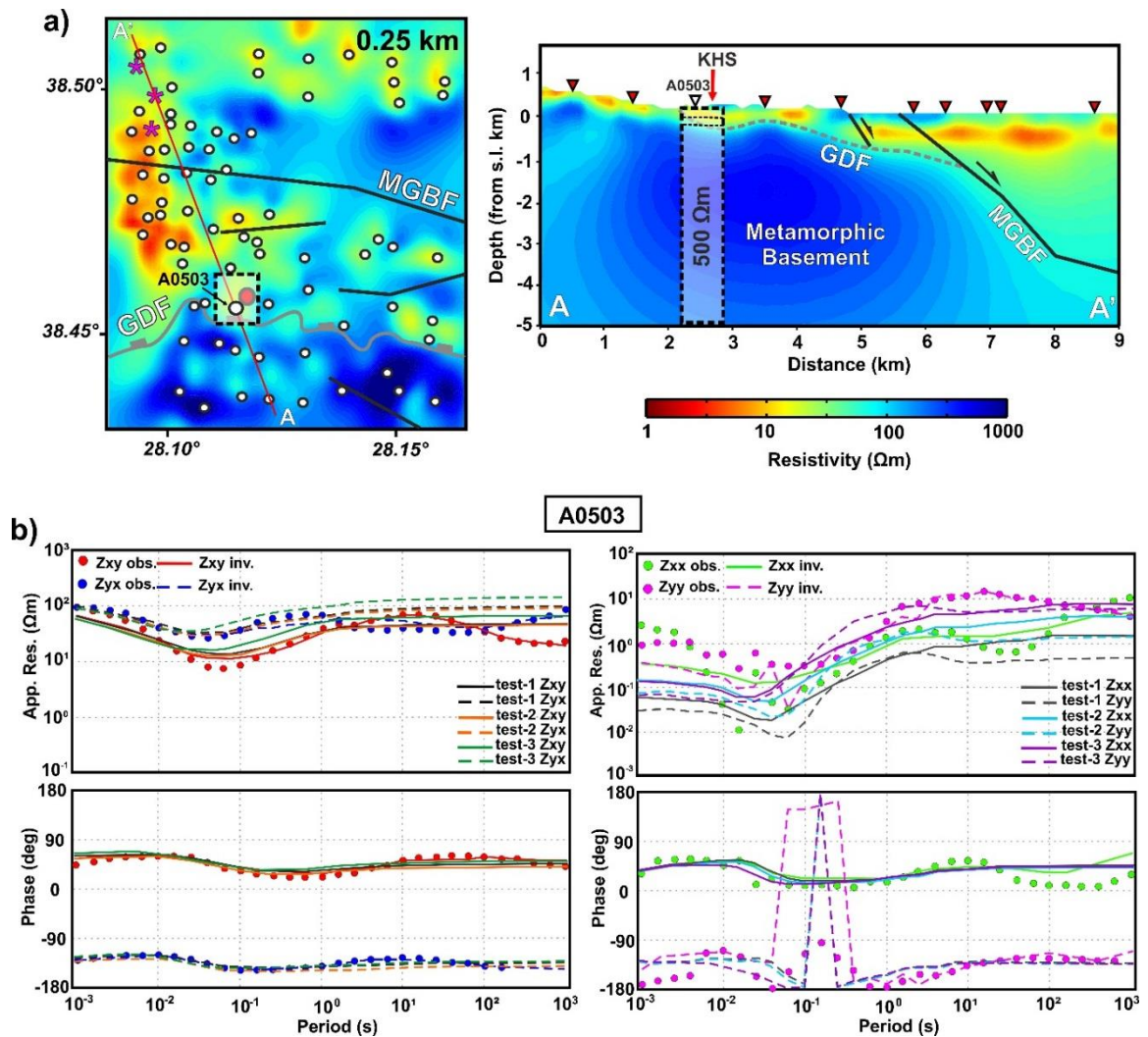


Figure 5.1. Sensitivity tests of the 3D inversion model obtained from Area A. (a) Schematic illustration of the tested 3D model together with modifications. The depth and cross sections with resistivity value of replacing blocks are shown in the corresponding model. (b) Comparison between responses of preferred inversion and tested models.

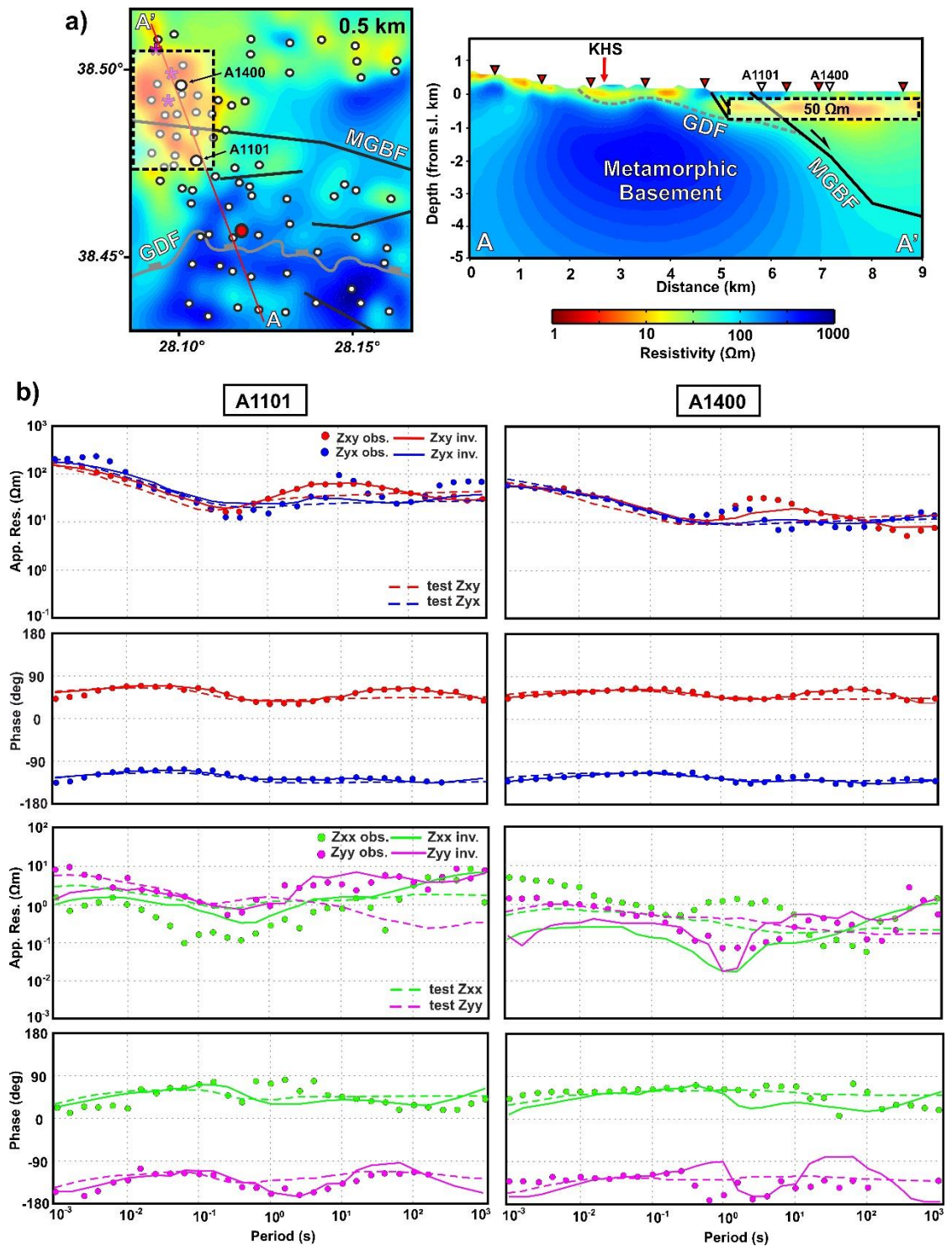


Figure 5.2. Sensitivity test of the 3D inversion model obtained from Area A. (a) Schematic illustration of the tested 3D model together with modifications. The depth and cross sections with resistivity value of replacing blocks are shown in the corresponding model.

(b) Comparison between responses of preferred inversion and tested models.

5.1.2. Test for Area B

In the investigation area B, a sensitivity test was conducted to examine the sensitivity of high conductivity feature C (Figures 4.8, 4.9 and 4.10). In order to perform this test, the conductive zone was replaced by a region with a unified resistivity value of 100 Ωm (test-1) and 500 Ωm (test-2). Subsequently, 3D forward modeling runs were carried out to examine whether the modified model could still fit the observed MT data. The RMS values between data and computed forward responses are obtained as 2.78 and 3.58 for test-1 and test-2, respectively. In Figure 5.3b, forward responses of the modified models are shown for two exemplary sites (B0201 and B0203) located on top of the artificially inserted blocks, which shows that replacing the conductive anomaly C with a resistive block lead to discrepancies between observed data and responses of the modified model. Therefore, the results of these tests testify the robustness of the highly conductive zone C.

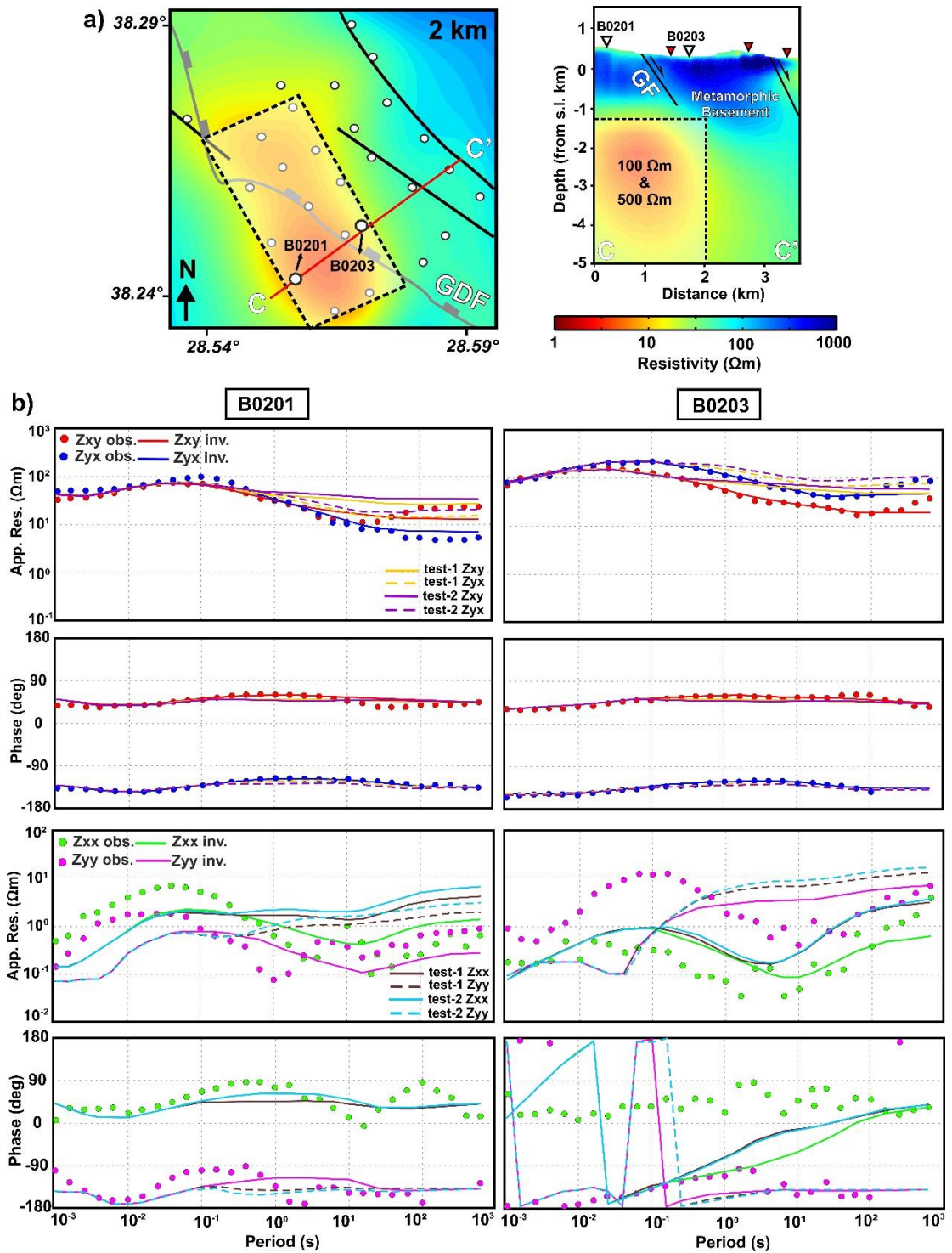


Figure 5.3. Sensitivity test of the 3D inversion model obtained from Area B. (a) Schematic illustration of the tested 3D model together with modifications. The depth and cross sections with resistivity value of replacing blocks are shown in the corresponding model. (b) Comparison between responses of preferred inversion and tested model.

5.1.3. Test for Area C

In the investigation area C, a sensitivity test was performed to verify the maximum thickness of the sedimentary cover of the Gediz Graben. This area is labeled as C in Figures 4.13, 4.14 and 4.15. In order to achieve that goal, a block with constant resistivity of 250 Ωm starting at three different depths 740 m (test-4), 1280 m (test-3), 1580 m (test-2) and 2220 m (test-1) and terminating at the base of the model was introduced into the preferred 3D resistivity model in order to mask the corresponding zone. The spatial extends and resistivity values of the inserted blocks are shown in Figure 5.4a. Subsequently, 3D forward modeling runs were performed to examine if the modified models still could fit the observed MT data. The RMS values between data and computed forward responses are 2.22 for test-4, 1.67 for test-3, 1.48 for test-2 and 1.45 for test-1, which indicates an increase in RMS values when inserted blocks are getting close to the surface. The comparison between the responses together with the observed data and the responses of preferred model are given in Figure 5.4b for two exemplary sites C91112 and C9193 situated on top of the inserted blocks. The results show that the change in spatial dimensions of the corresponding zone leads to discrepancies between the responses of the modified model and observed data, which may confirm that the base of the sedimentary fill in the Gediz Graben is approximately 2500-3000 m.

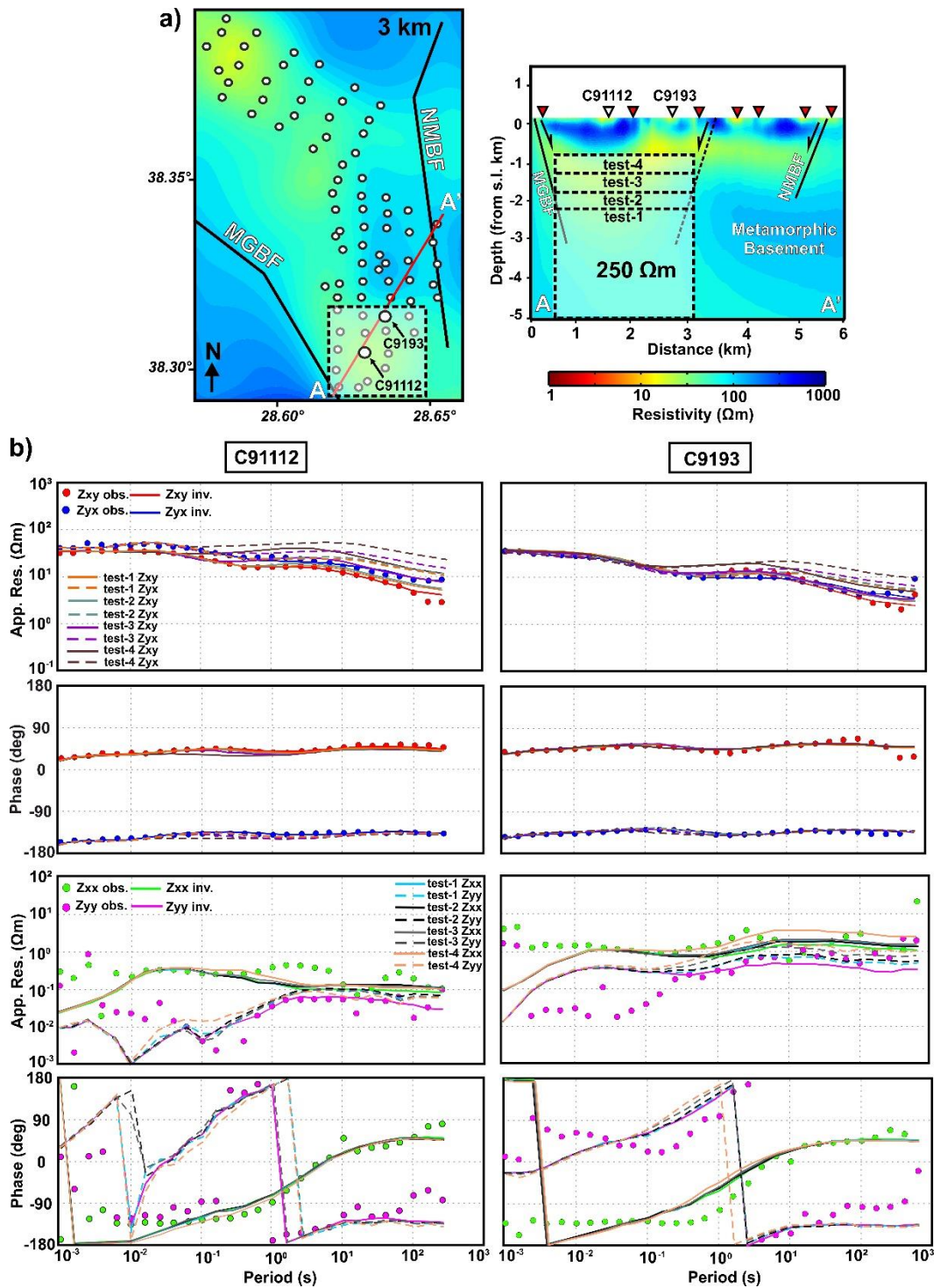


Figure 5.4. Sensitivity tests of the 3D inversion model obtained from Area C. (a) Schematic illustration of the tested 3D model together with modifications. The depth and cross sections with resistivity value of replacing blocks are shown in the corresponding model. (b) Comparison between responses of preferred inversion and tested models.

5.1.4. Test for Area D

In the investigation area D, a sensitivity test was conducted to examine the reliability of the deep reaching moderately conductive feature C2 shown in Figures 4.18, 4.19 and 4.20. To achieve that, a block with constant resistivity of 250 Ωm instead of C2 was introduced into the preferred 3D resistivity model (Figure 5.5a). A 3D forward modeling experiment was then carried out in order to examine if the modified model still could fit the observed data. The RMS values between data and forward responses in this test are 2.00. Forward responses of the modified model are shown in Figure 5.5b for two exemplary sites (D90117 and D9096) located on top of the inserted block. The results show that replacing the moderately conductive anomaly C2 with a resistive block leads to apparent discrepancies between observed data and responses of the modified model, which validates the robustness of the moderately conductive zone C2.

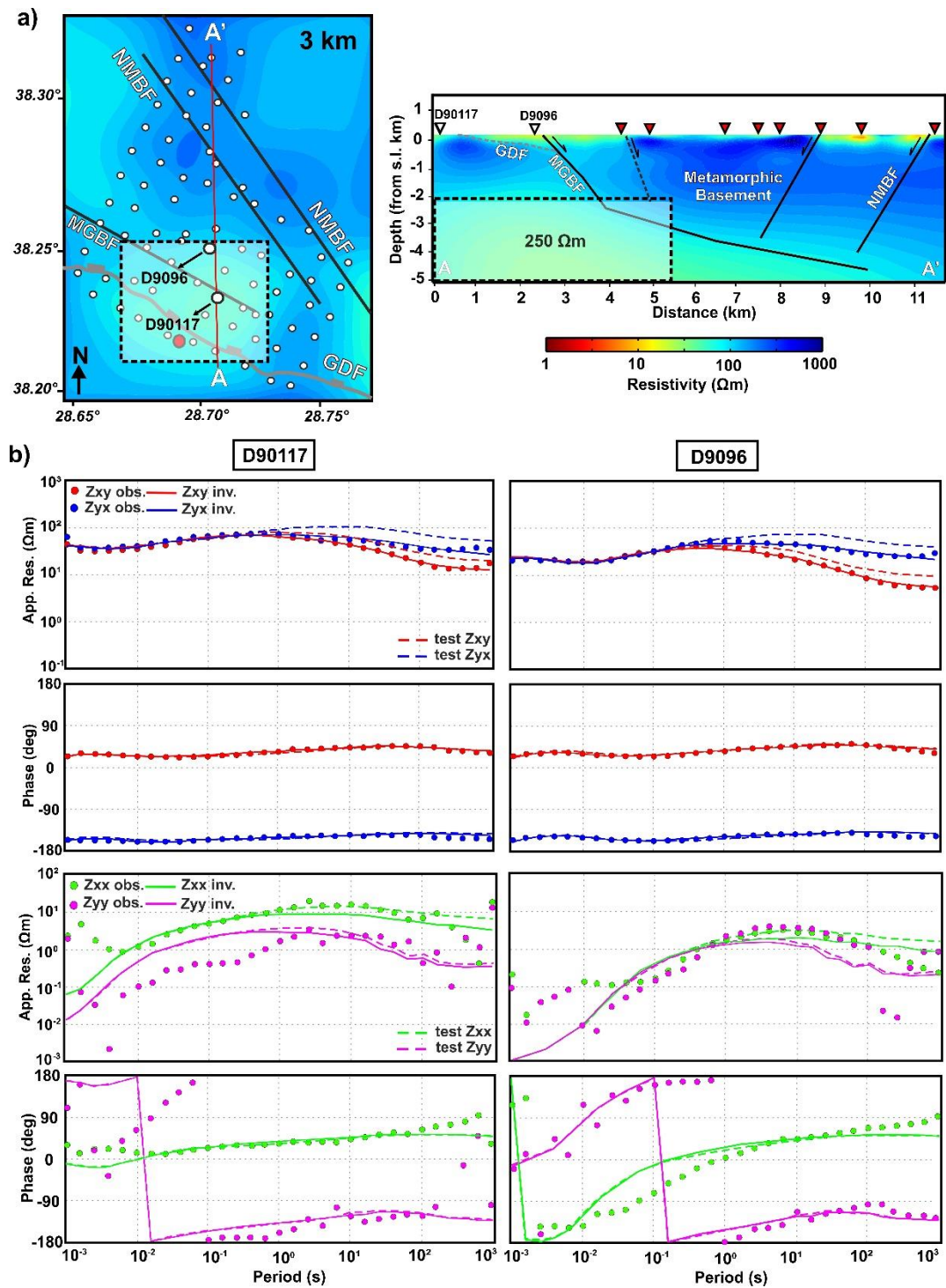


Figure 5.5. Sensitivity test of the 3D inversion model obtained from Area D. (a) Schematic illustration of the tested 3D model together with modifications. The depth and cross sections with resistivity value of replacing blocks are shown in the corresponding model. (b) Comparison between responses of preferred inversion and tested model.

Several tests were carried out to check the robustness of the 3D models obtained for the four different investigation areas A, B, C and D in the Gediz Graben. The responses of affected sites for all areas show significant differences between modified and inversion models. The overall RMS misfit values and misfit values for those affected sites also indicate a significant increase. Accordingly, the results of sensitivity tests confirm that the tested resistivity anomalies are required to represent observed MT data and thus subsurface electrical resistivity structure of the study area.

5.2. Synthetic Tests

To examine the effect of the areal site coverage, some synthetic model tests were conducted at each investigation area (A, B, C and D) of the Gediz Graben. The synthetic models representing the basic resistivity features of the four investigation areas were prepared. Forward modeling was then utilized to compute the predicted MT data at each area. Subsequently, the synthetic MT data were inverted using the same parameters used for the inversion of the MT field data, and then the results were compared with the synthetic models.

The background structure of the synthetic model which almost mimics the geoelectric model obtained from the investigation area A (Figure 5.6) is composed of three layers: (1) an electrical resistivity of 30 Ωm starting at 0 km (the surface) and terminating at 5 km depth; (2) a low electrical resistivity of 5 Ωm between 0.4 km and 0.9 km depth; and (3) a high electrical resistivity of 300 Ωm between 0 km and the base of the model. The forward response of the synthetic model at the 74 sites, which are chosen identical to the locations of sites existing in area A and covers a period range between 0.001 and 1000 s, was calculated using the ModEM code (Egbert and Kelbert, 2012; Kelbert *et al.*, 2014) with a 3D mesh consisting 84x66x110 cells in x, y and z directions, successively. The core area of the initial model was divided into 119 m blocks in the horizontal directions. The size of the padding cells in the horizontal directions was increased logarithmically by a factor of 1.3 outside the core region. 42 layers with thicknesses of 50 m, followed by 68 layers with logarithmically increasing thicknesses by a factor of 1.2 to the bottom of the model at 297 km were used in the vertical direction. In the 3D inversion, the same inversion parameters

with the parameters utilized in area A were used. Details of the 3D solution mesh used in inversion of the synthetic data are described in Section 4.3.1. 3D inversion results of the synthetic model are shown in Figure 5.7 as depth- and cross-sections. The resulting model obtained with full tensor components yields the subsurface model that is close to the synthetic model. In other words, the graben model composed of a conductive zone ($5 \Omega\text{m}$) that imitates an alteration zone in a resistive basement ($300 \Omega\text{m}$) and a relatively conductive zone ($30 \Omega\text{m}$) were correctly recovered.

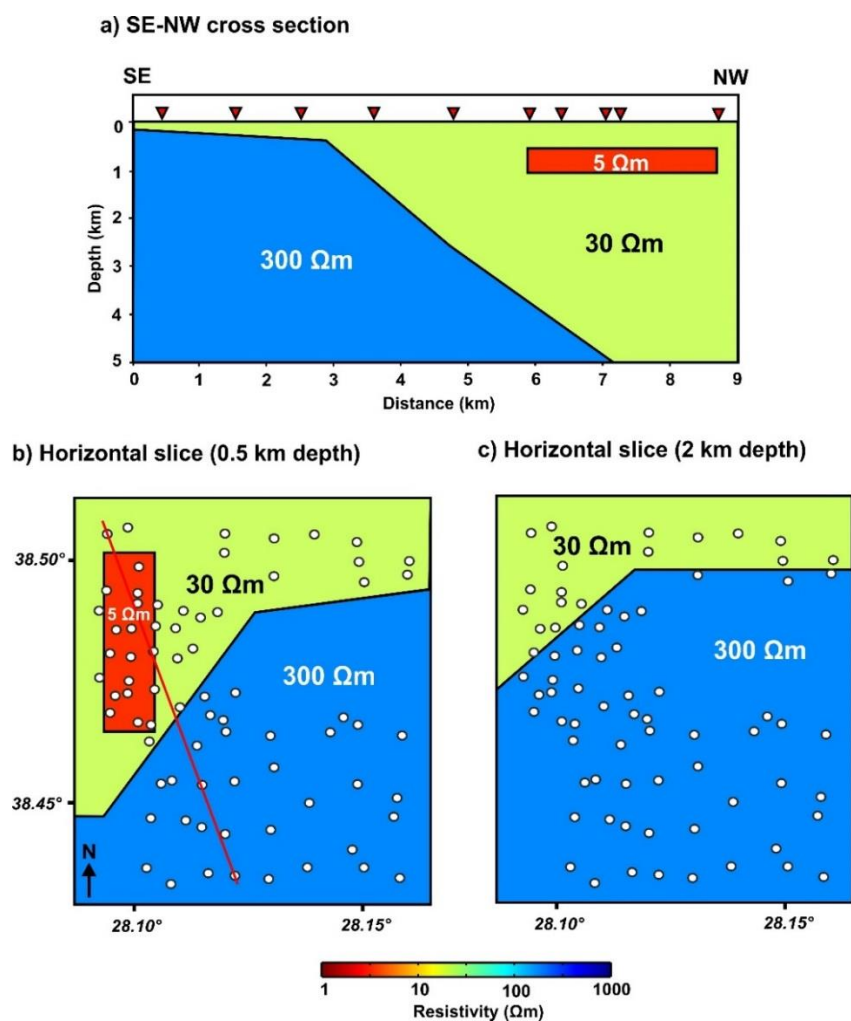


Figure 5.6. Synthetic geoelectric model mimics the geoelectric model obtained from the investigation area A. The model is composed of three zones having different resistivity values, namely an alteration zone with an electrical resistivity of $5 \Omega\text{m}$, a relatively conductive zone ($30 \Omega\text{m}$) and a highly resistive basement ($300 \Omega\text{m}$). The white dots represent the site locations chosen as similar to the locations of sites existing in area A.

The red line shows the location of the SE-NW cross section.

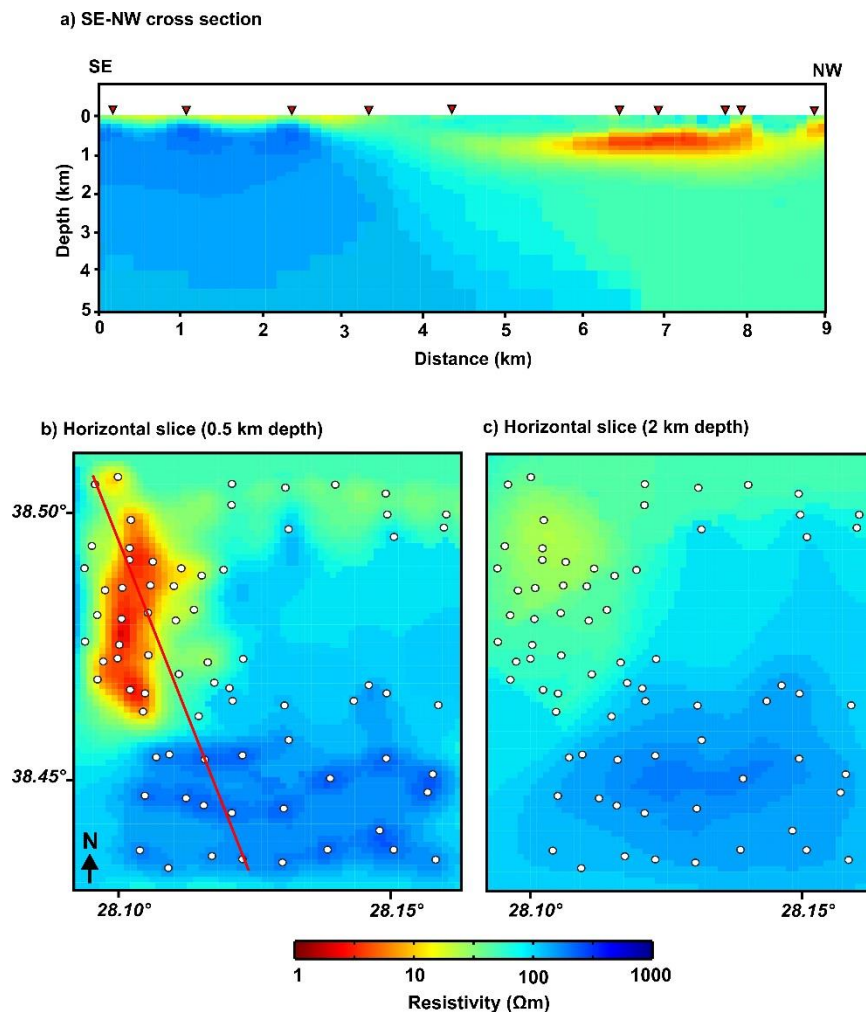


Figure 5.7. 3D inversion results of the test model. The model obtained by inverting full impedance tensor components. The starting model was a homogenous half-space of 100 Ωm , and the error floor were set as 5% value of $|Z_{xy}Z_{yx}|^{1/2}$. The total RMS misfit of 0.93 were achieved after 95 iterations. The white dots represent the site locations, and the red line marks the location of the SE-NW cross section.

The background structure of the synthetic model which almost mimics the geoelectric model obtained from the investigation area B (Figure 5.8) consists of four layers: (1) an electrical resistivity of 500 Ωm starting at 0 km (the surface) and terminating at 0.68 km depth; (2) an electrical resistivity of 250 Ωm between 0.68 km and 1.73 km depth; (3) an electrical resistivity of 30 Ωm between 0.68 km and the base of the model; and (4) a low

electrical resistivity of $10 \Omega\text{m}$ between 1.8 km and 4.13 km depth. The forward response of the synthetic model at the 27 sites, which are chosen identical to the locations of sites existing in area B and covers a period range between 0.001 and 1000 s, was calculated using the ModEM code (Egbert and Kelbert, 2012; Kelbert *et al.*, 2014) with a 3D mesh consisting $68 \times 68 \times 55$ cells in x, y and z directions, successively. The core area of the initial model was divided into 169.5 m blocks in the horizontal directions. The size of the padding cells in the horizontal directions was increased logarithmically by a factor of 1.3 outside the core region. In the vertical direction, the thickness of the first layer was selected as 25 m. The size of the cells were set with logarithmically increasing thicknesses by a factor of 1.2 to the bottom of the model at 222 km. In the 3D inversion, the same inversion parameters with the parameters utilized in area A were used. Details of the 3D solution mesh utilized in inversion of the synthetic data are described in Section 4.3.2. The results of the 3D inversion of the synthetic model are shown in Figure 5.9 as depth- and cross-sections. The resulting model obtained with full tensor components reveals the subsurface model that is close to the synthetic model. That is, a conductive zone having an electrical resistivity of $10 \Omega\text{m}$, a relatively conductive zone ($30 \Omega\text{m}$) and two resistive zones (250 and $500 \Omega\text{m}$) were correctly recovered.

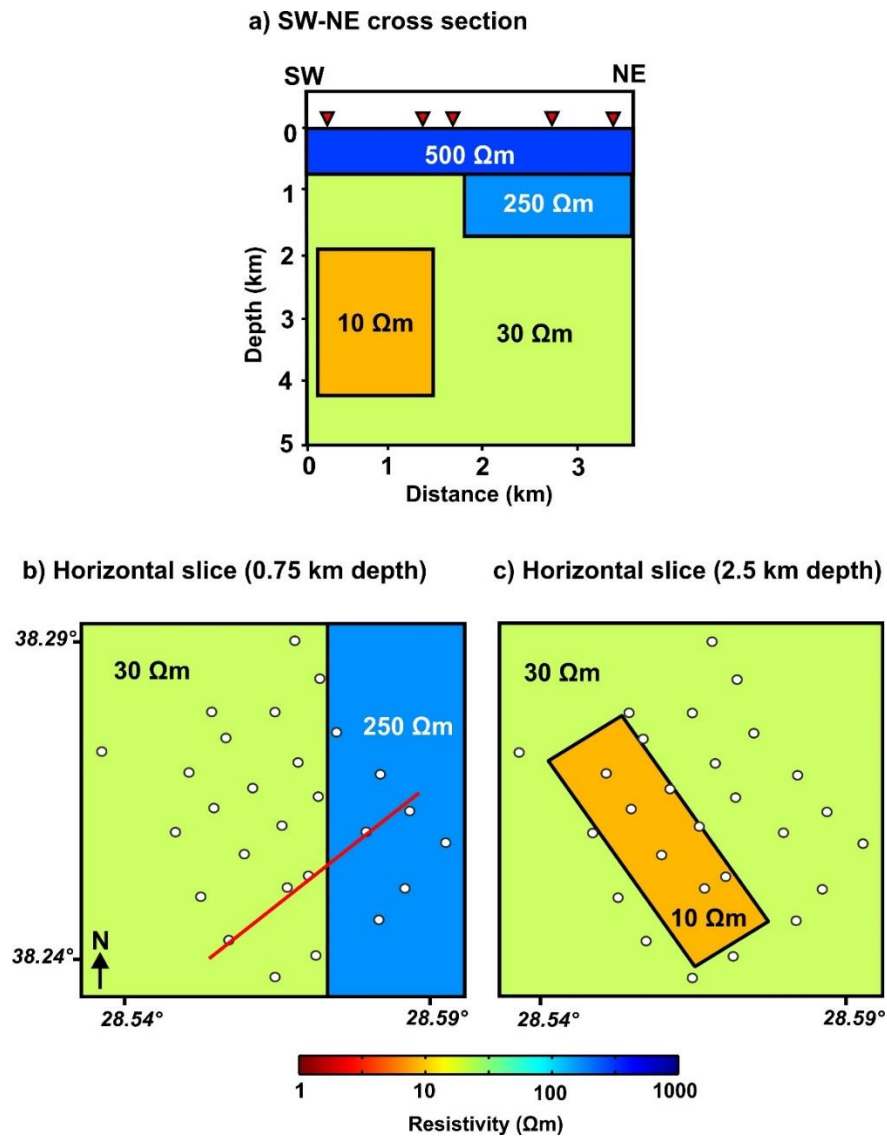


Figure 5.8. Synthetic geoelectric model mimics the geoelectric model obtained from the investigation area B. The model is composed of four zones having different resistivity values, namely a conductive zone with an electrical resistivity of 10 Ωm , a relatively conductive zone (30 Ωm) and two resistive zones (250 and 500 Ωm). The white dots represent the site locations chosen as similar to the locations of sites existing in area B. The red line shows the location of the SW-NE cross section.

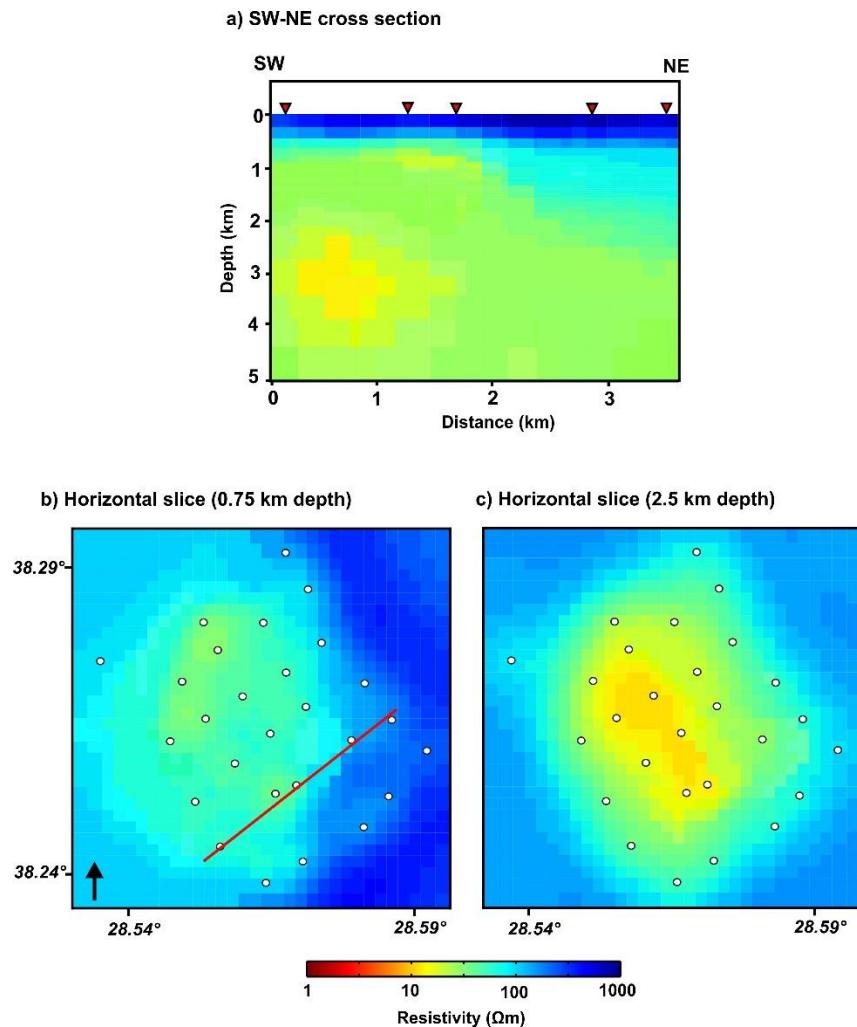


Figure 5.9. 3D inversion results of the test model. The model obtained by inverting full impedance tensor components. The starting model was a homogenous half-space of $100 \Omega\text{m}$, and the error floor were set as 5% value of $|Z_{xy}Z_{yx}|^{1/2}$. The total RMS misfit of 0.96 were achieved after 23 iterations. The white dots represent the site locations, and the red line marks the location of the SW-NE cross section.

The background structure of the synthetic model which almost mimics the geoelectric model obtained from the investigation area C (Figure 5.10) is composed of four layers: (1) an electrical resistivity of $500 \Omega\text{m}$ starting at 0 km (the surface) and terminating at 0.6 km depth (2) an electrical resistivity of $20 \Omega\text{m}$ starting at 0.6 km and terminating at 3 km depth; (3) an electrical resistivity of $100 \Omega\text{m}$ between 3 km and 5 km depth; and (4) an electrical resistivity of $250 \Omega\text{m}$ between 2.5 km and the base of the model. The forward

response of the synthetic model at the 78 sites, which are chosen identical to the locations of sites existing in area C and covers a period range between 0.001 and 1000 s, was calculated using the ModEM code (Egbert and Kelbert, 2012; Kelbert *et al.*, 2014) with a 3D mesh consisting 94x66x110 cells in x, y and z directions, successively. The core area of the initial model was divided into 150 m blocks in the horizontal directions. The size of the padding cells in the horizontal direction was increased logarithmically by a factor of 1.3 outside the core region. 42 layers with thicknesses of 50 m, followed by 68 layers with logarithmically increasing thicknesses by a factor of 1.2 to the bottom of the model at 297 km were used in the vertical direction. In the 3D inversion, the same inversion parameters with the parameters utilized in area C were used. Details of the 3D solution mesh utilized in inversion of the synthetic data are described in Section 4.3.3. The results of the 3D inversion of synthetic model are shown in Figure 5.11 as depth- and cross-sections. The resulting model obtained with full tensor components yields the subsurface model that is close to the synthetic model. A resistive zone (500 Ωm), a conductive zone (20 Ωm) and a zone of 100 Ωm and 250 Ωm were correctly recovered by 3D inversion. However, the conductive zone of 20 Ωm appears to be thinner in the 3D inversion model than the original model due to logarithmically increased thicknesses of the vertical cells beneath 2 km in contrast to linearly increased thicknesses above 2 km and the smooth transition to the deep resistive zones.

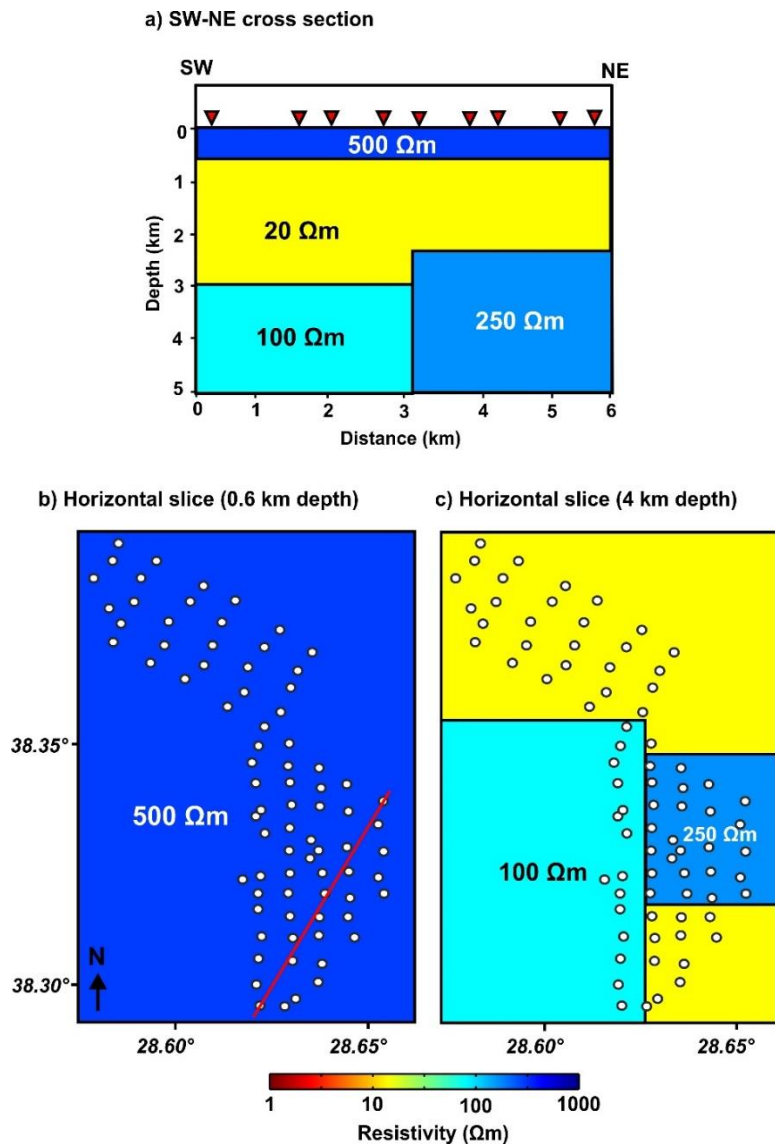


Figure 5.10. Synthetic geoelectric model mimics the geoelectric model obtained from the investigation area C. The model is composed of four zones having different resistivity values, namely a resistive zone (500 Ωm), a conductive zone (20 Ωm) and a zone of 100 Ωm and 250 Ωm . The white dots represent the site locations chosen as similar to the locations of sites existing in area C. The red line shows the location of the SW-NE cross section.

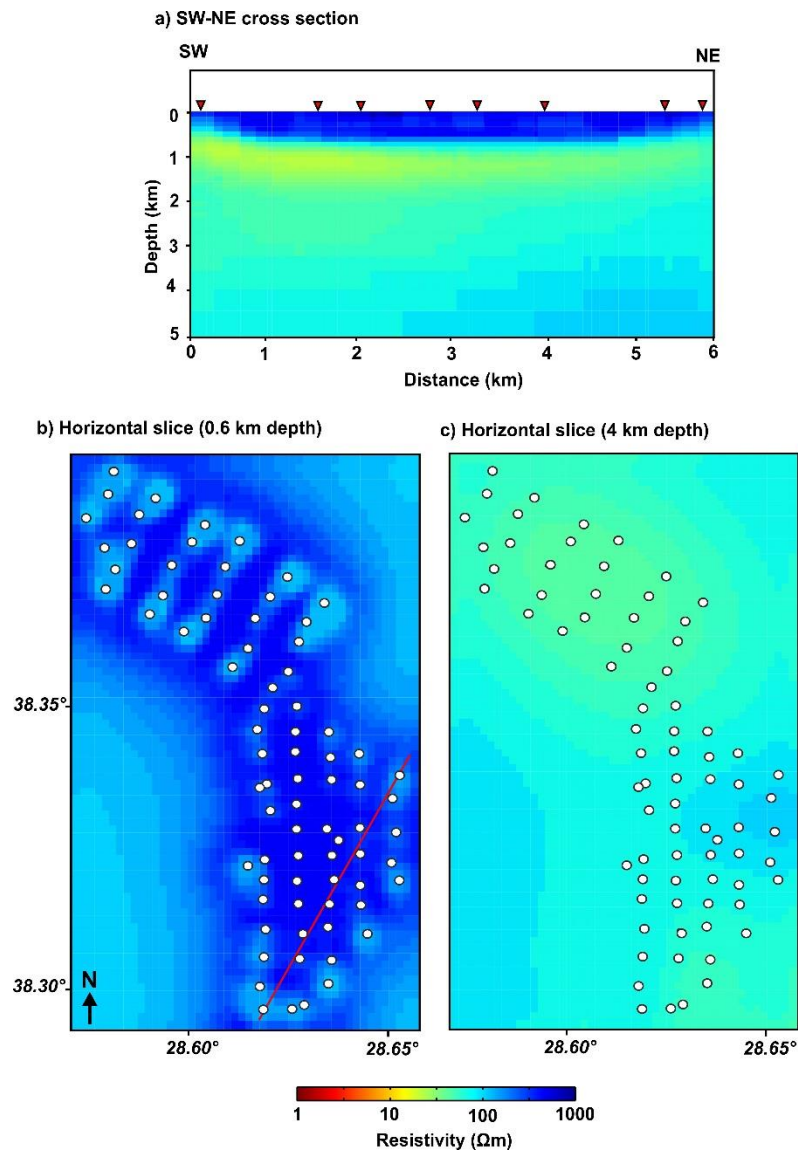


Figure 5.11. 3D inversion results of the test model. The model obtained by inverting full impedance tensor components. The starting model was a homogenous half-space of 100 Ωm , and the error floor were set as 5% value of $|Z_{xy}Z_{yx}|^{1/2}$. The total RMS misfit of 0.97 were achieved after 18 iterations. The white dots represent the site locations, and the red line marks the location of the SW-NE cross section.

The background structure of the synthetic model which almost mimics the geoelectric model obtained from the investigation area D (Figure 5.12) is composed of three layers: (1) an electrical resistivity of 20 Ωm starting at 0 km (the surface) and terminating at 0.4 km depth; (2) a high electrical resistivity of 250 Ωm between 0 km and 5 km depth; and (3) an electrical resistivity of 30 Ωm between 2.36 km and the base of the model. The forward

response of the synthetic model at the 74 sites, which are chosen identical to the locations of sites existing in area A and covers period range between 0.001 and 1000 s, was calculated using the ModEM code (Egbert and Kelbert, 2012; Kelbert *et al.*, 2014) with a 3D mesh consisting 84x66x110 cells in x, y and z directions, successively. The core area of the initial model was divided into 119 m blocks in horizontal directions. The size of the padding cells in the horizontal directions was increased logarithmically by a factor of 1.3 outside the core region. 42 layers with thicknesses of 50 m, followed by 68 layers with logarithmically increasing thicknesses by a factor of 1.2 to the bottom of the model at 297 km were used in the vertical direction. In the 3D inversion, the same inversion parameters with the parameters utilized in area D were used. Details of the 3D solution mesh utilized in inversion of the synthetic data are described in Section 4.3.4. The results of the 3D inversion of synthetic model are shown in Figure 5.13 as depth- and cross-sections. The resulting model obtained with full tensor components yields the subsurface model that is close to the synthetic model. In other words, a shallow conductive zone (20 Ωm), a resistive zone (250 Ωm) and a deep conductive zone (30 Ωm) were correctly recovered.

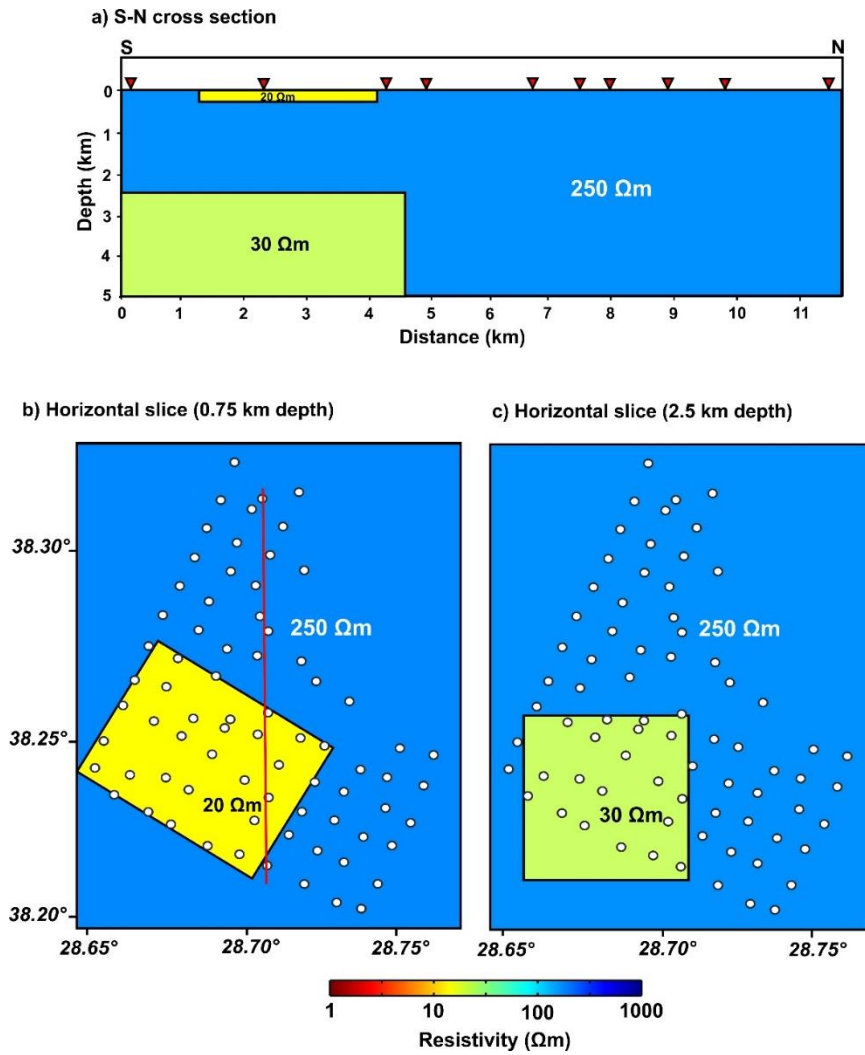


Figure 5.12. Synthetic geoelectric model mimics the geoelectric model obtained from the investigation area D. The model is composed of three zones having different resistivity values, namely a shallow conductive zone (20 Ωm), a resistive zone (250 Ωm) and a deep conductive zone (30 Ωm). The white dots represent the site locations chosen as similar to the locations of sites existing in area D. The red line shows the location of the S-N cross section.

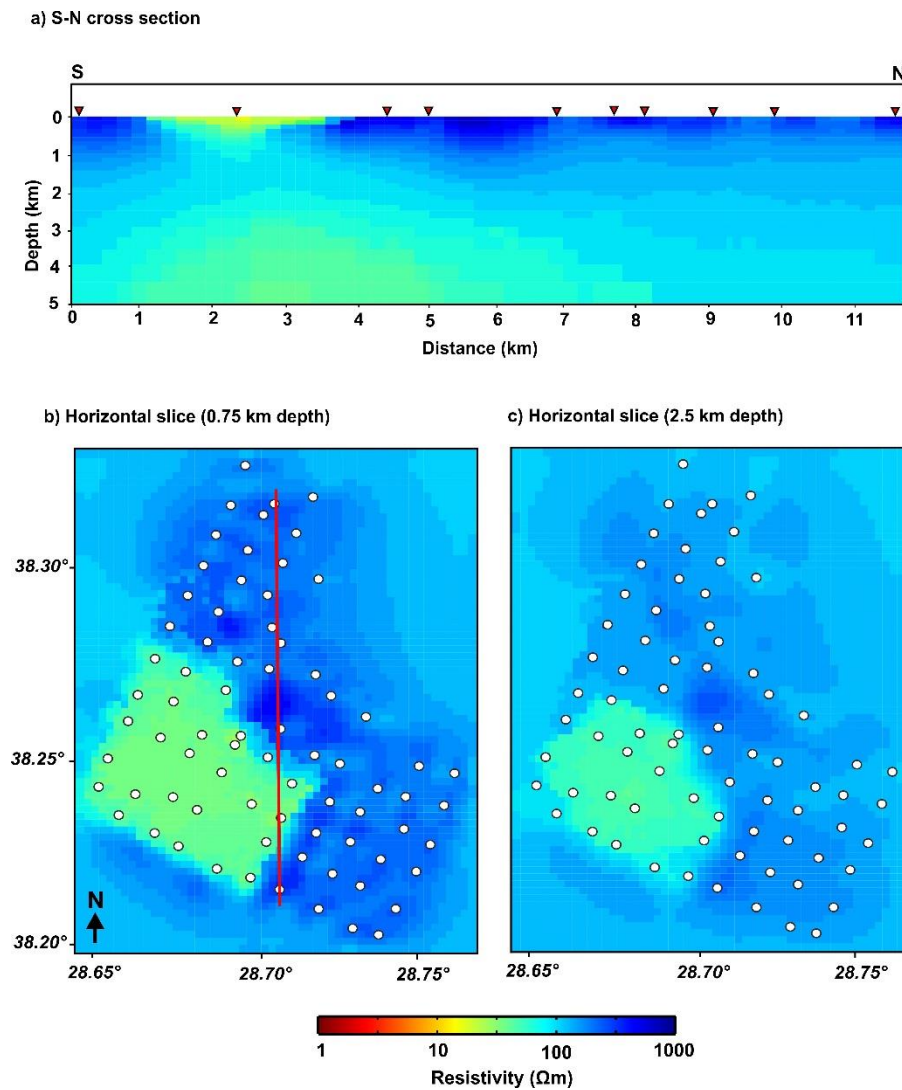


Figure 5.13. 3D inversion results of the test model. The model obtained by inverting full impedance tensor components. The starting model was a homogenous half-space of $100 \Omega\text{m}$, and the error floor were set as 5% value of $|Z_{xy}Z_{yx}|^{1/2}$. The total RMS misfit of 1.0 were achieved after 18 iterations. The white dots represent the site locations, and the red line marks the location of the S-N cross section.

6. DISCUSSION

In Chapter 4, the 3D preferred resistivity model of the Gediz Graben geothermal fields are presented as resistivity cross-sections and depth slices in addition to the 3D perspective view of the models. In the Salihli geothermal field, which includes the investigation area A, a cross section along the preferred profile and its interpretation based on the geothermal context are shown in Figure 6.1. The conductive zone ($<10 \Omega\text{m}$) interpreted as clay alteration zone is the most obvious feature in the resistivity cross-section. This zone continues along the whole section, and its morphology follows the topography. The area beneath this low resistivity zone is occupied by low-medium values of resistivity (50-100 Ωm). This zone is the deep reservoir of the geothermal system, which is confirmed by drilling of a deep geothermal well (SAN-3) to a depth ~ 2 km. The shallow conductive zone ($\sim 10 \Omega\text{m}$) coinciding with the Kurşunlu hot spring (KHS) can be attributed to sedimentary formation containing geothermal fluids at a maximum depth 300 m. Thus, the electrical resistivity model suggests two different types of reservoirs, a shallow reservoir (aquifer) corresponding to the KHS in the shallow sedimentary layer and a deep reservoir in the metamorphic basement. A typical high temperature geothermal system (temperature $>150\text{-}225$ °C) is characterized by an electrical resistivity structure describing the highest conductivity values often associated with the low temperature clay minerals (cap layer) overlying a more resistive reservoir zone generally having higher conductivity values than the surrounding non-geothermal areas due to its higher temperature than the host rocks (Pellerin *et al.*, 1996; Munoz, 2014; Patro, 2017). Therefore, as having a deep reservoir zone and a sedimentary layer acting both as a cap rock for geothermal system and a shallow reservoir to the KHS, the Salihli geothermal field has similar resistivity characteristics to other high enthalpy geothermal systems (e.g., the Coso geothermal field in southern California (Wannamaker *et al.*, 2004; Newman *et al.*, 2008), the Rotokawa geothermal field in New Zealand (Heise *et al.*, 2008), the Yanaizu-Nishiyama geothermal field in northeastern Japan (Uchida *et al.*, 2011) and the Tendaho geothermal field in northeastern Ethiopia (Didana *et al.*, 2015)). Assessment of empirical chemical geothermometers and mixing models applied to thermomineral waters suggest a discharge temperatures ranging from 37 °C to 155 °C in the Salihli geothermal fields, which implies a reservoir temperatures varying

between 150 °C and 230 °C (Tarcan *et al.*, 2000). Furthermore, the third highest temperature (182 °C) aquifer, Kavaklıdere-Sazdere in Turkey after Kızıldere (242 °C) and Germencik (232 °C) geothermal fields is also discovered in the graben (Tarcan *et al.*, 2005). The surface temperatures of up to 100 °C and the reservoir temperatures varying from 120 to 287 °C of thermal water are observed in Gediz Graben (Baba and Sözbilir, 2012). Additionally, the reservoir temperatures reaching 287 °C at a depth of 2954 m have also been measured in the graben (Baba *et al.*, 2015). The high heat flow values (125-170 mW/m²) obtained from airborne magnetic data (Akın *et al.*, 2014) also indicate high temperature geothermal systems in the Gediz Graben.

The heat source for the geothermal systems existing in the Gediz Graben could be a magma intrusion heating up the water in reservoir rocks at shallow depths (<10 km) since high temperature geothermal systems mostly occur when magma intrudes into shallow crustal levels in tectonically active regions (Munoz, 2014; Patro, 2017). The deep seismic tomography results for the Anatolian region indicates several segments which are separated by tears attributed to upwelling hot asthenosphere of the northward subducting African lithosphere beneath Anatolia, and the upwelling hot asthenosphere that is spatially coincident with the Mendere Massif in the tomographic section (E-E') is clearly imaged beneath the Kula volcanic field located on the northern flank of the Gediz Graben (Biryol *et al.*, 2011), which shows agreement with that the highest heat flow values in western Anatolia (>100 mW/m²) has been measured at shallow (~100 m) boreholes in this volcanic area (Erkan, 2015). Gessner *et al.*, (2013) and Uzel *et al.*, (2015) also proposed that the İzmir-Balıkesir Transfer Zone is a surface expression of a tear in the subducting African slab, and thus the mantle lithosphere has directly settled under the continental crust in a region including Mendere Massif, indicating high geothermal gradients at shallow depths. Ten Dam and Khrebtov (1970) also suggested the thermal gradients up to 1.5 °C/10 m and locally up to 2.5-3 °C/10 m (five-ten times the normal average geothermal gradient) by measuring the gradient at geothermal wells in the Gediz Graben. The high content of the boron in thermomineral waters of the Gediz Graben associated with the degassing of the magma intrusions in the area also indicates a magma chamber (Gemici and Tarcan, 2002; Tarcan *et al.*, 2005). Moreover, helium isotope composition of the geothermal fluids proposes that both heat and helium are transferred via mantle melting which is either transported to surface

forming the volcanics or emplaced at crustal level (Güleç and Hilton, 2006). High V_p/V_s ratio (>1.85) also indicates partial melt at lower crustal depths (Vanacore *et al.*, 2013). The magnetotelluric study carried out in western Anatolia suggests a shallow lithosphere-asthenosphere boundary undulating between 30 and 50 km and a conductive lower crust ($< 75 \Omega\text{m}$) associated with the existence of partial melting (Bayrak and Nalbant, 2001). A highly conductive partially melted (viscoelastic) lower crust ($10 \Omega\text{m}$) at an average depth of 10 km has been also identified in the Gediz Graben (Gürer *et al.*, 2001; 2002). Consequently, tectonic activities accompanied by magma intrusions into crust and by volcanism in western Anatolia may lead to heat transfer from the interior of the Earth to the upper crust, and thus the geothermal gradient and also heat flow is increased regionally. This can be considered as the heat source of the geothermal systems in the Gediz Graben.

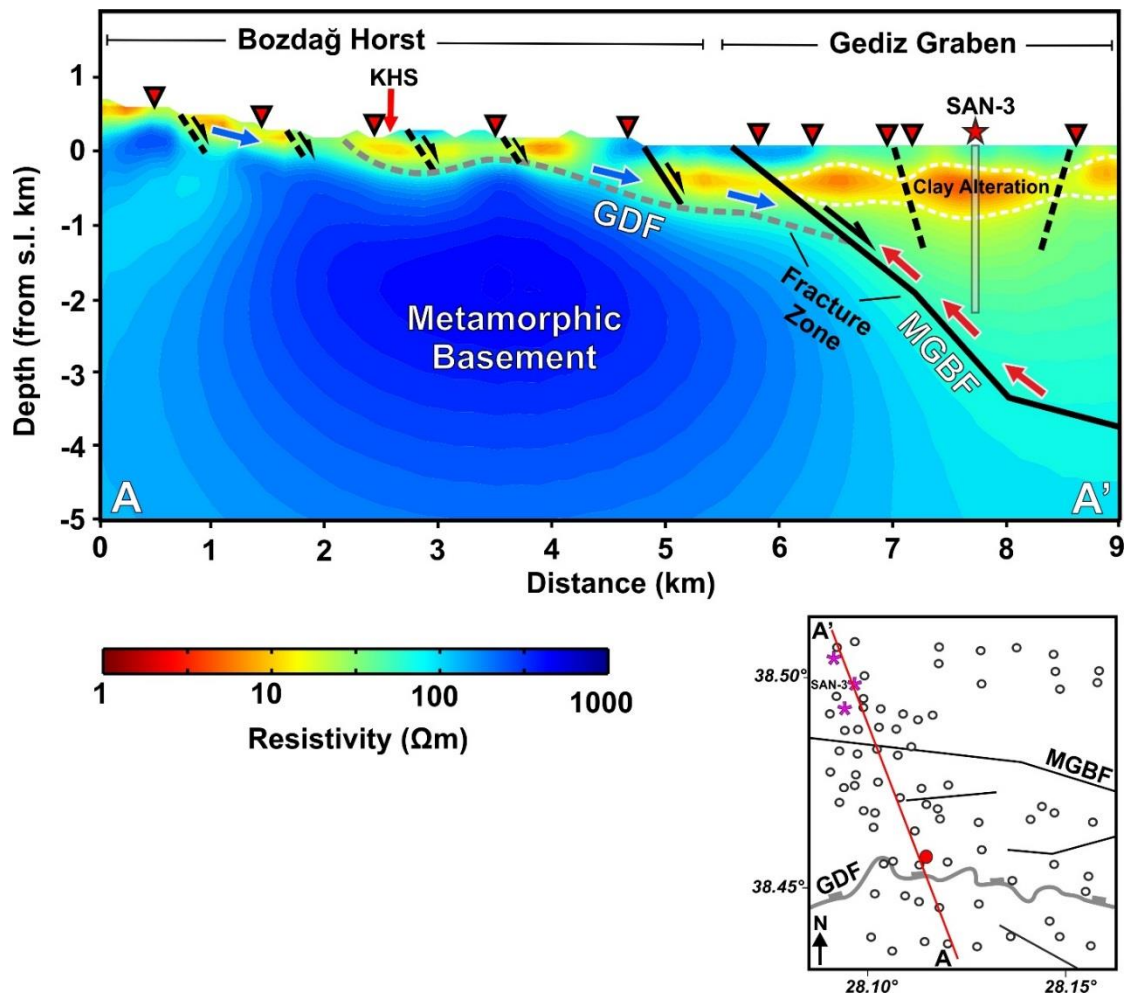


Figure 6.1. Cross section derived from the preferred 3D inverse model and the corresponding interpretation for Area A. The location map of the preferred profile is shown at the bottom right corner. The dashed white line corresponds to the area with a resistivity lower than 10 Ωm , which has been attributed to the hydrothermal alteration of clay minerals. Solid black lines indicate normal faults, and dashed black lines mark the interpreted faults. The dashed gray line marks the GDF. The blue and red arrows deduce flows of cold and geothermal fluids. The partial transparent gray line indicates production well (SAN-3).

One of the most important elements of the geothermal systems located in the Gediz Graben is the existence of a system of faults filled with geothermal fluids and altered rocks, which suggests the presence of a fracture zone (Figures 6.1). The high angle normal faults and particularly the low angle Gediz detachment fault (GDF) probably accommodating the deep circulation of hydrothermal fluids dominantly control the geothermal systems in the area. The mineral compositions obtained from K-Ar ages of cataclasites and gouges from the GDF indicate smectite-illite alteration mineralogy, and hydrogen isotope analysis of rock samples collected from the GDF and normal faults show that the normal faults above the GDF provides pathways for downward flow of meteoric waters into and along the GDF (Hetzl *et al.*, 2013). Mineral alterations and intense veining (Işık *et al.*, 2013) indicate extensive fluid circulation occurring along the detachment zone. The analyses of isotopic and hydrochemical data in the Gediz Graben geothermal fields propose that the geothermal fluids are of meteoric origin (Tarcan *et al.*, 2005; Özen *et al.*, 2012) while isotopic analysis of carbon dioxide (CO₂) in the thermomineral waters indicates a magmatic origin (Ercan *et al.*, 1994). Furthermore, the electrical resistivity model shown in Figure 6.1 characterizes an upflow zone beneath the graben, which is also mainly controlled by the intersection of the GDF and main graben-bounding fault (MGBF). The deep-reaching MGBF in particular acts as a conduit through which fluids, heat and also mantle gasses are transported from the deeper parts of the crust to near the surface. The outflow of geothermal fluids on the other hand is predominantly controlled by lower bounding sub-horizontal GDF, and the base of the high conductivity anomaly in this area gets closer to the surface. According to this model, it can be suggested that the pathways for both cold meteoric waters and geothermal fluids are the highly permeable normal faults and the sub-horizontal GDF. In other words, meteoric waters infiltrating into deep reservoir through the north dipping faults and GDF are heated up by a hot water circulation into the deep, and then some of waters containing meteoric and magmatic fluids rise up to surface through the permeable upper part of the MGBF and GDF. This results in geothermal manifestations such as shallow reservoirs or hot springs in the junctions of the faults (e.g., KHS (Figure 6.1)). The meteoric waters also recharge the sedimentary sequence and deep reservoir of the Gediz Graben through the normal faults terminating on the detachment fault, and the reservoir rocks (marbles and fractured metamorphic rocks of the Menderes Massif) bounded by impermeable or low permeability rocks or faults store the fluids inside its pores. The recharge area of the geothermal system

is high levels of the southern part of the study area, namely the stepping topography of the Bozdağ Horst (2159 m). Although the MGBF flanks the graben to the south, the northern boundary of the graben is not resolved with the present MT data in the investigation area A. To construct additional MT sites to the north of the study area would help to gain further insights into understanding the subsurface configuration of the reservoir. The geothermal elements are also summarized in Figure 6.1.

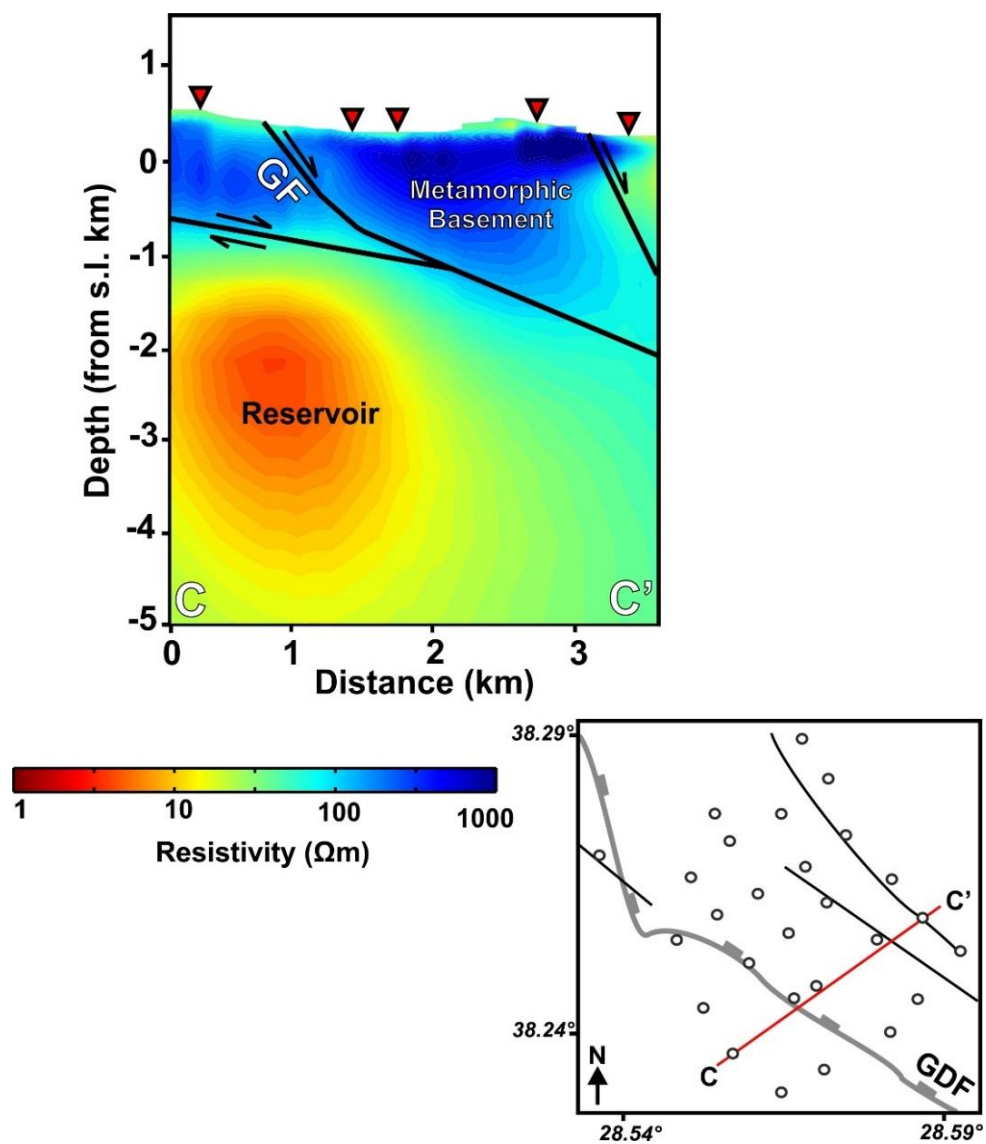


Figure 6.2. Cross section derived from the preferred 3D inverse model and the corresponding interpretation for Area B. The location map of the preferred profile is shown at the bottom right corner. Solid black lines indicate normal faults. GF: Girelli segment of the GDF.

A deep reservoir characterized by fractures within metamorphic rocks at a depth of about 1.5 km have been delineated in investigation area B (Figure 6.2). This geothermal system does not resemble the classical electrical resistivity structure describing a highly conductive clay cap overlying a relatively less conductive reservoir zone of a conventional geothermal system, presenting a different type of reservoir characteristic than the investigation area A for the Gediz Graben. The intrusive rocks of the reservoir are mainly granites in this investigation area. These rocks are hot enough to provide the required thermal energy to the reservoir but they cannot produce low resistivities in compact form. However, when these rocks are fractured and filled with fluids, they may lead to a decrease in bulk resistivity due to enhanced hydraulic permeability. In the area, faulting that results in fracturing of the basement rock facilitates the migration and supplementation of heat and geothermal fluids within a high permeability host. The pattern of the fault systems controlling the southern margin of the Gediz Graben where investigation area B is located suggests a complex structure with discrete fault segments and with generally WNW-ESE oriented fractures (Çiftçi, 2013). The Girelli segment of the GDF, which is named as the Girelli Fault (GF), with its low permeability, acting as a boundary for the geothermal activity and plays a significant role in locally confinement of heat and geothermal fluids. The fault plane solutions of the mainshocks and subevents of the Alaşehir and Gediz earthquakes occurred in the Gediz Graben indicate 6-10 km focal depths, and are attributed to the normal faults breaking the crust from surface to the uppermost part of the lower crust (Eyidoğan and Jackson, 1985). The corresponding normal faults for the Alaşehir earthquake ($M_s=6.5$) are associated with the deep low angle segment of the MGBF (Çiftçi and Bozkurt, 2010), indicating that the crustal scale MGBF is the main agent of fluids and heat transferred from the ductile lower crust to the brittle upper crust. Çiftçi (2013) reported that temperatures increase exponentially with depth when an exploration well drilled in the Gediz Graben gets closer to the MGBF, and it reaches to 140 °C around 1600 m. The geothermal gradient measured in the deeper sections of the well also indicates significantly higher values than the graben average of 4.5 °C/100 m. Furthermore, the depth of the Moho in the study area is approximately 30 km (Mutlu and Karabulut, 2011; Vanacore *et al.*, 2013), which implies a comparatively thin crust facilitating the outflow of heat outward.

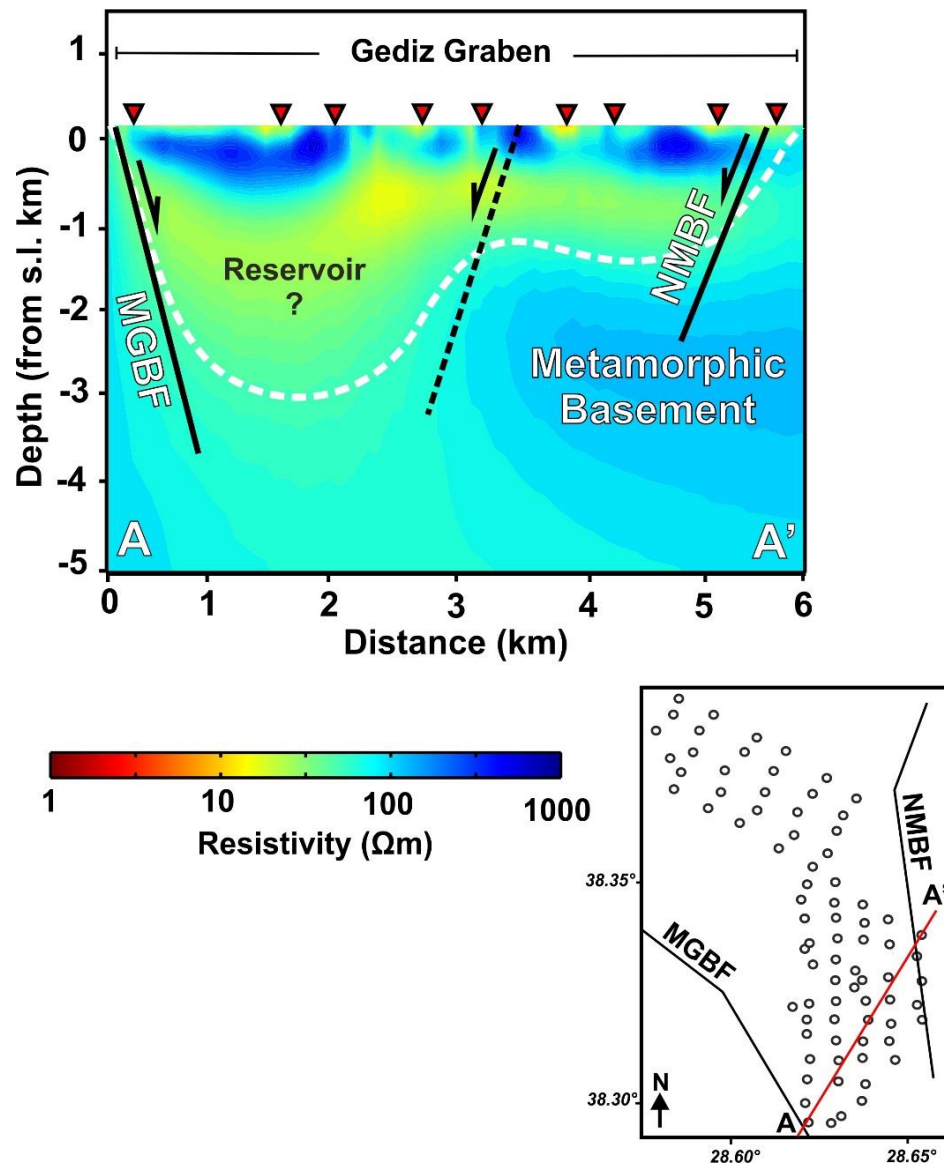


Figure 6.3. Cross section derived from the preferred 3D inverse model and the corresponding interpretation for Area C. The location map of the preferred profile is shown at the bottom right corner. The dashed white line corresponds to the area representing undulating graben floor, which has been associated with the sedimentary fill of the Gediz Graben. Solid black lines indicate normal faults, and dashed black lines mark the interpreted faults.

In the middle part of the Gediz Graben basin, a sedimentary fill bearing reservoir characteristic for geothermal fluids is delineated in the investigation area C (Figure 6.3). The natural permeability of this sedimentary fill is probably controlled by faults bounding the graben. The salinity of water samples taken from sedimentary layer in the graben is below

7000 ppm (Çiftçi, 2013), implying that fresh water is situated in sedimentary reservoir. The thickness of the sedimentary layer reaches 2500-3000 m in the middle part of the graben basin (Figure 6.3). 2D seismic surveys and wells drilled in the vicinity of the Alaşehir also suggest that the thickest sedimentary fill is approximately 3000 m in the Gediz Graben (Çiftçi and Bozkurt, 2010), which is spatially coincident with the middle part of the graben. On the other hand, Sari and Şalk (2006) by analyzing the Bouguer gravity data speculated the maximum thickness of the sedimentary layer as more than 2000 m in the graben. The thickness of the sedimentary fill decreases gradually on the northern and southern margins of the graben (Figure 6.3). Sedimentary rocks form a very thin layer above the metamorphic basement in area D, and the corresponding thickness becomes roughly 300 m at the easternmost end of the graben (Figure 6.4). Gürer *et al.*, (2002) also proposed changing sedimentary thicknesses between 950 and 3800 m along the graben as a result of 1D interpretation of MT data. Moreover, as shown in Figure 6.3, graben floor shows undulations. 2D gravity and MT modeling also promote undulating basement topography under the conductive sedimentary fill along the graben (Gürer *et al.*, 2001; 2002).

A deep moderately conductive (30-50 Ωm) dome-shaped feature which may be attributed to a zone of hydrothermal fluid circulation exists in the southern margin of the Gediz Graben in area D (Figure 6.4). The conductive zone in the basement may represent a potential geothermal fluid reservoir, and fractured rocks, particularly faults facilitates to convectively transport heat through the basement. Within the convective regime, the pressure regime is dominantly hydrostatic in the area. The hydrostatic pressure gradient of 9.8 MPa/km was computed in the graben fill, and measured values of pore pressures characterize overpressure zones that is associated with the sealing of faults (Çiftçi, 2013). Porosity and permeability measurements of potential reservoir rock facies obtained from outcrop exposures also bring out large porosity variations from tight to 35 % and permeability values in the range of 0.02 to 40 md (Çiftçi *et al.*, 2010). Accordingly, high value of porosity and permeability facilitate the flow of hot waters and strongly control the efficiency of geothermal energy extraction from reservoirs in the Gediz Graben.

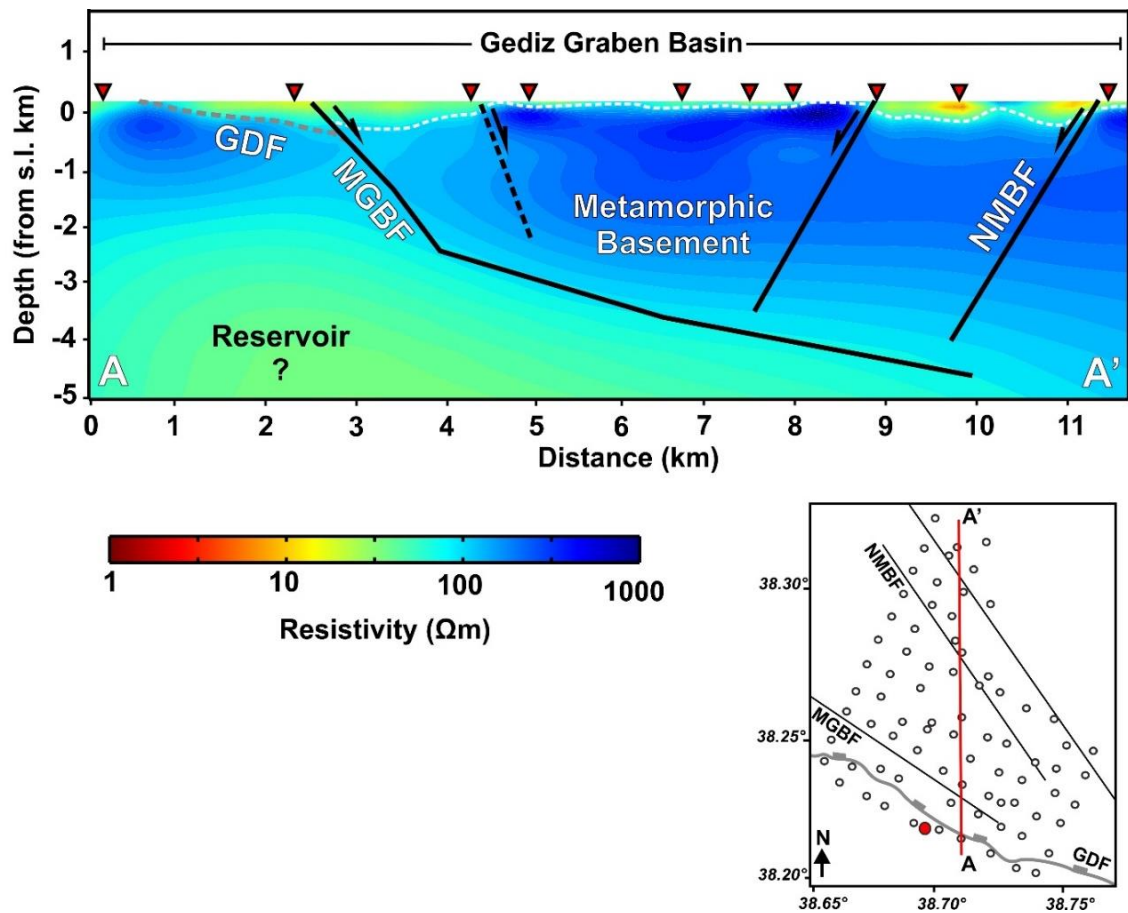


Figure 6.4. Cross section derived from the preferred 3D inverse model and the corresponding interpretation for Area D. The location map of the preferred profile is shown at the bottom right corner. The dashed white line corresponds to the area with a resistivity lower than $30 \Omega m$, which has been attributed to shallow sediments of the Gediz Graben. Solid black lines indicate normal faults, and dashed black lines mark the interpreted faults. The dashed gray line marks the GDF.

7. CONCLUSION

This study is an attempt to contribute to the understanding of the reservoir types, heat sources and structural controls of the geothermal fields situated in the Gediz Graben. In this context, it is the most comprehensive study carried out in various geothermal areas of the graben by utilizing magnetotelluric (MT) method, and it also provides the opportunity to discuss the electrical conductivity distribution with the structural controls and geothermal system characteristics of this tectonically active region.

The wide-band MT data (0.001-1000 s) recorded by 253 sites at four different investigation areas of the graben were analyzed and modeled in the study. The 3D resistivity models of the geothermal fields resolve three different reservoir types at different geothermal fields of the Gediz Graben. In area A, a classical geoelectrical distribution of a high temperature geothermal system, with a prominent highly conductive hydrothermal alteration zone sitting above a more resistive reservoir zone are delineated. A deep reservoir zone characterized by fractures within metamorphic rocks in the highly resistive basement is depicted in area B. A shallow reservoir (aquifer) corresponding to the hot spring (KHS) in the shallow sedimentary layer of the Gediz Graben basin is also revealed in area A.

The extensional tectonics accompanied by magma intrusions into crust in western Anatolia may lead to heat transfer from the interior of the Earth to the upper crust by thinning crust, which is associated with the heat source of the geothermal systems in the graben. The geothermal fields occurring along the southern margin of the graben are structurally controlled, and the circulation of geothermal fluids in reservoirs are closely related to major faults and fractured zones hosting geothermal fluids and generally extending to deeper levels of the crust. The crustal scale main graben-bounding fault (MGBF) specifically plays a significant role in heat transfer. It acts as a conduit through which fluids and heat are transported from deeper parts of the crust to near surface, which is perfectly characterized in Area A. The meteoric waters that infiltrate deep into the crust through the north dipping faults are probably heated up by magmatic intrusions, and some of waters containing meteoric and magmatic fluids rise up to surface through the permeable faults, particularly

through the lower bounding sub-horizontal Gediz detachment fault (GDF). The GDF also has a special importance in areas A and B. In area A, it facilitates descending of meteoric water into the deep reservoir and ascending of the geothermal fluids to the shallow reservoir. On the other hand, the GDF in area B acts as a boundary for the geothermal reservoir and provides locally confinement of heat and geothermal fluids. The geothermal manifestations in area A, B and D are spatially coincident with the intersecting zone of two fractures, namely the GDF and high angle normal faults. Furthermore, in areas A and D, the 3D MT modeling results bring out a well-defined interface between the sedimentary cover and underlying metamorphic basement due to high resistivity contrast between two layers, and this boundary characterizes the GDF. Moreover, in area C, it is shown that the maximum thickness of the sedimentary layer reaches 2500-3000 m in the middle part of the graben basin. However, the corresponding thickness decreases gradually on the northern and southern margins of the graben. The thickness of the sedimentary layer becomes much thinner towards the eastern end of the graben, which is depicted in area D. 3D resistivity models in area C also delineate an undulating basement topography under the conductive sedimentary fill of the graben.

REFERENCES

- Aizawa, K., Y. Ogawa, and T. Ishido, "Groundwater flow and hydrothermal systems within volcanic edifices: delineation by electric self-potential and magnetotellurics" *Journal of Geophysical Research.*, Vol. 114, B01208, 2009.
- Akın, U., U.E. Ulugergerli, and S. Kutlu, "The assessment of geothermal potential of Turkey by means of heat flow estimation", *Bulletin of the Mineral Research and Exploration*, Vol. 149, pp. 201-210, 2014.
- Akyol, N., L. Zhu, B.J. Mitchell, H. Sözbilir, and K. Kekovalı, "Crustal structure and local seismicity in western Anatolia", *Geophysical Journal International*, Vol. 166, pp. 1259-1269, 2006.
- Arango, C., A. Marcuello, J. Ledo, and P. Queralt, "3D magnetotelluric characterization of the geothermal anomaly in the Lluçmajor aquifer system (Majorca, Spain)", *Journal of Applied Geophysics*, Vol. 68, pp. 479-488, 2009.
- Archie, G.E., "The electrical resistivity log as an aid in determining some reservoir characteristic", *Transactions of the AIME*, Vol. 146, pp. 54-62, 1942.
- Arnason, K., H. Eysteinnsson, and G.P. Hersir, "Joint 1D inversion of TEM and MT data and 3D inversion of MT data in the Hengill area, SW Iceland", *Geothermics*, Vol. 39, pp. 13-34, 2010.
- Arpat, E., and E. Bingöl, "Ege bölgesi graben sisteminin gelişimi üzerine düşünceler", *Mineral Research and Exploration Institute (MTA) of Turkey Bulletin (in Turkish)*, Vol. 79, pp. 1-9, 1969.
- Ateş, A., P. Kearey, and S. Tufan, "New gravity and magnetic anomaly maps of Turkey", *Geophysical Journal International*, Vol. 136, pp. 499-502, 1999.

Aydın, I., H.I. Karat, and A. Koçak, “Curie-Point Depth Map of Turkey”, *Geophysical Journal International*, Vol. 162, pp. 633–640, 2005.

Baba, A., and H. Sözbilir, “Source of arsenic based on geological and hydrochemical properties of geothermal systems in Western Turkey”, *Chemical Geology*, Vol. 334, pp. 364–377, 2012.

Baba, A., C. Şimşek, O. Gündüz, A. Elçi, and A. Murathan, “Hydrochemical Properties of Geothermal Fluid and Its Effect on the Environment in Gediz Graben, Western Turkey”, *Proceedings World Geothermal Congress 2015*, Melbourne, Australia, 2015.

Barka, A., “The North Anatolian Fault Zone”, *Annales Tectonicae*, Vol. 6, pp. 164-195, 1992.

Başokur A.T., *Türev tabanlı parametre kestirim yöntemleri*, JFMO Eğitim Yayınları, 2015.

Bayrak, M., and S.S. Nalbant, “Conductive crust imaged in western Turkey by MT”, *Geophysical Research Letters*, Vol. 28, pp. 3521-3524, 2001.

Bedrosian, P., “MT + Integrating Magnetotellurics to Determine Earth Structure, Composition and Processes”, *Survey in Geophysics*, Vol. 28, pp. 121-167, 2007.

Berdichevsky, M. N., and V. I. Dmitriev, “*Models and Methods of Magnetotellurics*”, Springer, Berlin, 2008.

Berkthold, A., “Electromagnetic studies in geothermal regions”, *Geophysical Surveys*, Vol. 6, pp. 173-200, 1983.

Bertrand, E.A., T.G. Caldwell, G.J., Hill, E.L. Wallin, S.L. Bennie, N. Cozens, S.A. Onacha, G.A. Ryan, C. Walter, A. Zaino, and P. Wameyo, “Magnetotelluric imaging of upper-crustal

convection plumes beneath the Taupo Volcanic Zone, New Zealand”, *Geophysical Research Letters*, Vol. 39, L02304, 2012.

Bertrand, E.A., T.G. Caldwell, G.J. Hill, S.L. Bennie, and S. Soengkono, “Magnetotelluric imaging of the Ohaaki geothermal system, New Zealand: Implications for locating basement permeability”, *Journal of Volcanology and Geothermal Research*, Vol. 268, pp. 36-45, 2013.

Bertrand, E.A., T.G. Caldwell, S. Bannister, S. Soengkono, S.L. Bennie, G.J. Hill, and W. Heise, “Using array MT data to image the crustal resistivity structure of the southeastern Taupo Volcanic Zone, New Zealand”, *Journal of Volcanology and Geothermal Research*, Vol. 305, pp. 63-75, 2015.

Biryol, C.B., S.L. Beck, G. Zandt, and A. Özacar, “Segmented African lithosphere beneath the Anatolian region inferred from teleseismic P-wave tomography”, *Geophysical Journal International*, Vol. 184, pp. 1037-1057, 2011.

Bozkurt, E., “Neotectonics of Turkey-a synthesis”, *Geodinamica Acta*, Vol. 14, pp. 3-30, 2001.

Bozkurt, E., “Origin of NE-trending basins in western Turkey”, *Geodinamica Acta*, Vol. 16, pp. 61-81, 2003.

Bozkurt, E., and H. Sözbilir, “Tectonic evolution of the Gediz Graben: field evidence for an episodic, two-stage extension in western Turkey”, *Geological Magazine*, Vol. 141, pp. 63-79, 2004.

Bozkurt, E., and S.K. Mittwede, “Introduction: Evolution of continental extensional tectonics of western Turkey”, *Geodinamica Acta*, Vol. 18/3-4, pp. 153-165, 2005.

Browne, P.R.L., “Hydrothermal alteration in active geothermal fields”, *Annual Review Earth and Planetary Sciences*, Vol. 6, pp. 229-250, 1978.

Cagniard, L., “Basic Theory of the Magnetotelluric Method in Geophysical Prospecting”, *Geophysics*, Vol. 18, pp. 605-635, 1953.

Caldwell, G., C. Pearson, and H. Zahadi, “Resistivity of rocks in geothermal systems: A laboratory study”, *Proceedings of the 8th Geothermal Workshop, Auckland, New Zealand*, Auckland University, 1986.

Caldwell, T.G., H.M. Bibby, and C. Brown, “The magnetotelluric phase tensor”, *Geophysical Journal International*, Vol. 158, pp. 457-469, 2004.

Campanya, J., J. Ledo, P. Queralt, A. Marcuello, J.A. Munoz, M. Liesa, A.G. Jones, “New geoelectrical characterization of a continental collision zone in the Central-Eastern Pyrenees: Constraints from 3-D joint inversion of electromagnetic data”, *Tectonophysics*, Vol. 742-743, pp. 168-179, 2018.

Chang, P.Y., W. Lo, S.R. Song, K.R. Ho, C.S. Wu, C.S. Chen, Y.C. Lai, H.F. Chen, and H.Y. Lu, “Evaluating the Chingshui geothermal reservoir in northeast Taiwan with a 3D integrated geophysical visualization model”, *Geothermics*, Vol. 50, pp. 91-100, 2014.

Chave, A. D., and A. G. Jones, *The Magnetotelluric Method: Theory and Practice*, Cambridge University Press, 2012.

Chiang, C.W., H.L. Hsu, and C.C. Chen, “An Investigation of the 3D Electrical Resistivity Structure in the Chingshui Geothermal Area, NE Taiwan”, *Terrestrial Atmospheric and Oceanic Sciences*, Vol. 26(3), pp. 269-281, 2015.

Cohen, H.A., C.J. Dart, H.S. Akyüz, and A. Barka, “Syn-rift sedimentation and structural development of the Gediz and Büyük Menderes graben, western Turkey”, *Journal of the Geological Society, London*, Vol. 152, pp. 629-638, 1995.

Çağlar, I., “Electrical Resistivity Structure of the Northwestern Anatolia and its Tectonic Implications for the Sakarya and Bornova Zones”, *Physics of the Earth Planetary Interiors*, Vol. 125, pp. 95-110, 2001.

Çakır, Z., “Along-strike discontinuity of active normal faults and its influence on Quaternary travertine deposition: examples from western Turkey”, *Turkish Journal of Earth Sciences*, Vol. 8, pp. 67-80, 1999.

Çiftçi, N.B., and E. Bozkurt, “Anomalous stress field and active breaching at relay ramps: a field example from Gediz Graben, SW Turkey”, *Geological Magazine*, Vol. 144, pp. 687-699, 2007.

Çiftçi, N.B., and E. Bozkurt, “Evolution of the Miocene sedimentary fill of the Gediz Graben, SW Turkey”, *Sedimentary Geology*, Vol. 216, pp. 49-79, 2009a.

Çiftçi, N.B., and E. Bozkurt, “Pattern of normal faulting in the Gediz Graben, SW Turkey”, *Tectonophysics*, Vol. 473, pp. 234-260, 2009b.

Çiftçi, N.B., and E. Bozkurt, “Structural evolution of the Gediz Graben, SW Turkey: temporal and spatial variation of the graben basin”, *Basin Research*, Vol. 22, pp. 846-873, 2010.

Çiftçi, N.B., R.Ö. Temel, and H. İztan, “Hydrocarbon occurrences in the western Anatolia (Aegean) grabens, Turkey: Is there a working petroleum system?”, *AAPG Bulletin*, Vol. 94, pp. 1827-1857, 2010.

Çiftçi, N.B., “In-situ stress field and mechanics of fault reactivation in the Gediz Graben, Western Turkey”, *Journal of Geodynamics*, Vol. 65, pp. 136-147, 2013.

Dewey, J.F., and A.M.C. Şengör, “Aegean and surrounding regions: Complex multiplate and continuum tectonics in a convergent zone”, *Geological Society of America Bulletin*, Vol. 90, pp. 84-92, 1979.

Dewey, J.F., “Extensional collapse of orogens”, *Tectonics*, Vol. 7, pp. 1123-1139, 1988.

Didana, Y.L., S. Thiel, and G. Heinson, “Three dimensional conductivity model of the Tendaho High Enthalpy Geothermal Field, NE Ethiopia”, *Journal of Volcanology and Geothermal Research*, Vol. 290, pp. 53-62, 2015.

Oner, Z., and Y. Dilek, “Supradetachment basin evolution during continental extension: The Aegean province of western Anatolia, Turkey”, *Geological Society of America Bulletin*, Vol. 123, pp. 2115-2141, 2011.

Oner, Z., and Y. Dilek, “Fault kinematics in supradetachment basin formation, Menderes core complex of western Turkey”, *Tectonophysics*, Vol. 608, pp. 1394-1412, 2013.

Dogliani, C., S. Agostini, M. Crespi, F. Innocenti, P. Manetti, F. Riguzzi, Y. Savaşçın, “On the extension in western Anatolia and the Aegean Sea”, *Journal of Virtual Exploration*, Vol. 8, pp. 169-183, 2002.

Dolmaz, M.N., Z.M. Hisarlı, T. Ustaömer, and N. Orbay, “Curie Point Depths Based on Spectrum Analysis of Aeromagnetic Data, West Anatolian Extensional Province, Turkey”, *Pure and Applied Geophysics*, Vol. 162, pp. 571–590, 2005.

Egbert, G. D. and J. R. Booker, “Robust estimation of geomagnetic transfer functions”, *Geophysical Journal International*, Vol. 87, pp. 173-194, 1986.

Egbert, G. D., “Robust multiple-station magnetotelluric data processing”, *Geophysical Journal International*, Vol. 130, pp. 475-496, 1997.

Egbert, G. D. and A. Kelbert, “Computational Recipes for Electromagnetic Inverse Problems”, *Geophysical Journal International*, Vol. 189, pp. 251-267, 2012.

Emre, T. and H. Sözbilir, “Tectonic evolution of the Kiraz Basin, Küçük Menderes Graben: Evidence for compression/uplift-related basin formation overprinted by extensional tectonics in west Anatolia”, *Turkish Journal of Earth Sciences*, Vol. 16, pp. 441-470, 2007.

Ercan, T., J.I. Matsuda, K. Nagao, and I. Kıta, “Anadolu’daki sıcak sularda bulunan doğal gazların izotopsal bileşimleri ve karbondioksit gazının enerji açısından önemi (in Turkish)”, *In: Dünya Enerji Konseyi, Türkiye 6. Enerji Kongresi*, İzmir, Turkey, pp. 197-207, 1994.

Erdoğan E., and M.E. Candansayar, “The conductivity structure of the Gediz Graben geothermal area extracted from 2D and 3D magnetotelluric inversion: Synthetic and field data applications”, *Geothermics*, Vol. 65, pp. 170-179, 2017.

Erkan, K., “Geothermal investigations in western Anatolia using equilibrium temperatures from shallow bore holes”, *Solid Earth*, Vol. 6, pp. 103-113, 2015.

Eyidoğan H., and J. Jackson, “A seismological study of normal faulting in the Demirci, Alaşehir and Gediz earthquakes of 1969-70 in western Turkey: implications for the nature and geometry of deformation in the continental crust”, *Geophysical Journal of the Royal Astronomical Society*, Vol. 81, pp. 569-607, 1985.

Faulds, J.E., V. Bouchot, I. Moeck, and K. Oguz, “Structural controls on geothermal systems in western Turkey: a preliminary report”, *GRC Transactions*, Vol. 33, pp. 375-381, 2009.

Fossen, H., *Structural Geology*, Cambridge University Press, 2016.

Gamble, T.D., W.M. Goubau, and J. Clark, “Magnetotelluric with a Remote Magnetic Reference”, *Geophysics*, Vol. 44, pp. 53-68, 1979.

Gemici, Ü., and G. Tarcan, “Distribution of boron in thermal waters of western Anatolia, Turkey, and examples of their environmental impacts”, *Environmental Geology*, Vol. 48, pp. 87-98, 2002.

Gessner, K., L.A. Gallardo, V. Markwitz, U. Ring, and S.N. Thomson, "What caused the denudation of the Menderes Massif: Review of crustal evolution, lithosphere structure, and dynamic topography in southwest Turkey", *Gondwana Research*, Vol. 24, pp. 243-274, 2013.

Güleç, N., and D.R. Hilton, "Helium and heat distribution in western Anatolia, Turkey: Relationship to active extension and volcanism", *Geological Society of America Special Paper*, Vol. 409, pp. 305-319, 2006.

Gürer, A., Ö.F. Gürer, A. Pinçe, and O.M. İlkışık, "Conductivity structure along the Gediz Graben, western Anatolia, Turkey: tectonic implications", *International Geology Review*, Vol. 43, pp.1129-1144, 2001.

Gürer, A., A. Pinçe, Ö.F. Gürer, and O.M. İlkışık, "Resistivity Distribution in the Gediz Graben and its Implications for Crustal Structure", *Turkish Journal of Earth Sciences*, Vol. 11, pp. 15-25, 2002.

Gürer, O.F., E. Sangu, and M. Özburan, "Neotectonics of the SW Marmara region, NW Anatolia, Turkey", *Geological Magazine*, Vol. 143, pp. 229-241, 2006.

Griffiths, D. J., "*Introduction to Electrodynamics*", 3rd Edition, Prentice-Hall, Upper Saddle River, NJ, 1999.

Harinarayana, T., K.K. Abdul Azeez, K. Naganjaneyulu, C. Manoj, K. Veeraswamy, D.N. Murthy, and S. Prabhakar Eknath Rao, "Magnetotelluric studies in Puga valley geothermal field, NW Himalaya, Jammu and Kashmir, India", *Journal of Volcanology and Geothermal Research*, Vol. 138, pp. 405-424, 2004.

Harinarayana, T., K.K. Abdul Azeez, D.N. Murthy, K. Veeraswamy, S.P. Eknath Rao, C. Manoj, and K. Naganjaneyulu, "Exploration of geothermal structure in Puga geothermal field, Ladakh Himalayas, India by magnetotelluric studies", *Journal of Applied Geophysics*, Vol. 58, pp. 280-295, 2006.

Heise, W., T.G. Caldwell, H.M. Bibby, S.C. Bannister, “Three-dimensional modeling of magnetotelluric data from the Rotokawa geothermal field, Taupo Volcanic Zone, New Zealand”, *Geophysical Journal International*, Vol. 173, pp. 740-750, 2008.

Heise, W., T.G. Caldwell, E.A. Bertrand, G.J. Hill, S.L. Bennie, N.G. Palmer, “Imaging the deep source of the Rotokawa and Waimangu geothermal fields, Taupo Volcanic Zone, New Zealand”, *Journal of Volcanology and Geothermal Research*, Vol. 314, pp. 39-48, 2016.

Hetzl, R., H. Zwingmann, A. Mulch, K. Gessner, C. Akal, A. Hampel, T. Güngör, R. Petschick, T. Mikes, and F. Wedin, “Spatiotemporal evolution of brittle normal faulting and fluid infiltration in detachment fault systems: A case study from the Menderes Massif, western Turkey”, *Tectonics*, Vol. 32, pp. 1-13, 2013.

Hochstein, M.P., “Classification and assessment of geothermal resources”, *Dickson MH and Fanelli M (eds) Small geothermal resources, UNITAEW NDP Centre for Small Energy Resources*, Rome, Italy, pp. 31-59, 1990.

Hohmann, G.W., “Three-dimensional EM modeling”, *Geophysical Surveys*, Vol. 6, 27-53, 1983.

Horasan, G., L. Gülen, A. Pınar, D. Kalafat, N. Özel, H.S. Kuleli, and A.M. Işıkara, “Lithospheric structure of the Marmara and Aegean regions, Western Turkey”, *Bulletin of the Seismological Society of America*, Vol. 92, pp. 322-329, 2002.

Işık, V., G. Seyitoğlu, and İ. Çemen, “Ductile-brittle transition along the Alaşehir detachment fault and its structural relationship with the Simav detachment fault, Menderes massif, western Turkey”, *Tectonophysics*, Vol. 374, pp. 1-18, 2003.

İlkışık, O.M., “Regional Heat Flow in Western Anatolia Using Silica Temperatures Estimates from Thermal Springs”, *Tectonophysics*, Vol. 244, pp. 175-184, 1995.

Jiracek, G.R., V. Haak, K.H. Olsen, “*Practical Magnetotellurics in a Continental Rift Environment*”, in K.H. Olsen, ed., *Continental rifts: evolution, structure and tectonics*, Elsevier, New York, pp. 103-129, 1995.

Jones, A.G., “Parkinson's Pointers Potential Perfidy!”, *Geophysical Journal of the Royal Astronomical Society*, Vol. 87, pp. 1215-1224, 1986.

Jones, A.G., A.D. Chave, D. Auld, K. Bahr, and G. Egbert, “A comparison of techniques for magnetotelluric response function estimation”, *Journal of Geophysical Research*, Vol. 94, pp. 14201-14213, 1989.

Jones, A.G., and I. Dumas, “Electromagnetic images of a volcanic zone”, *Physics of the Earth and Planetary Interiors*, Vol. 81, pp. 289-314, 1993.

Jones, A.G., “Distortion of magnetotelluric data: its identification and removal”, In: A.D. Chave, A.G. Jones (eds), *The Magnetotelluric Method: Theory and Practice*, 1st edn., Cambridge University Press, New York, 2012.

Kaufman A. A. and G.V. Keller, *The magnetotelluric sounding method, methods in geochemistry and geophysics*, Elsevier scientific publishing, Amsterdam, 1981.

Karato, S., and D. Wang, “Electrical conductivity of minerals and rocks”, *Physics and Chemistry of the Deep Earth*, John Wiley and Sons, LTD, Chichester, 2013.

Kelbert, A., N. Meqbel, G.D. Egbert, K. Tandon, “ModEM: a modular system for inversion of electromagnetic geophysical data”, *Computers&Geosciences*, Vol. 66, pp. 40-53, 2014.

Kiyan, D., A.G. Jones, and J. Vozar, “The inability of magnetotelluric off-diagonal impedance tensor elements to sense oblique conductors in three-dimensional inversion”, *Geophysical Journal International*, Vol. 196, pp. 1351-1364, 2014.

Koçyiğit, A., H. Yusufoglu, and E. Bozkurt, "Evidence from the Gediz graben for episodic two-stage extension in western Turkey", *Journal of Geological Society, London*, Vol. 156, pp. 605-616, 1999.

Krieger, L., and J.R. Peacock, "MTpy: a Python toolbox for magnetotellurics", *Computers & Geosciences*, Vol. 72, pp. 167-175, 2014.

Kuyumcu, Ö.C., U.Z. Destegül Solaroğlu, S. Hallinan, B. Çolpan, E. Türkoğlu, and W. Soyer, "Interpretation of 3D magnetotelluric (MT) surveys: basement conductors of the Menderes Massif, Western Turkey", *GRC Transactions*, Vol. 35, pp. 861-866, 2011.

Larsen, J.C., R.L. Mackie, A. Manzella, A. Fiordelisi, and S. Rieven, "Robust smooth magnetotelluric transfer functions", *Geophysical Journal International*, Vol. 124, pp. 801-819, 1996.

Lee, T.J., Y. Song, and T. Uchida, "Three-dimensional magnetotelluric surveys for geothermal development in Pohang Korea", *Exploration Geophysics*, Vol. 38, pp. 89-97, 2007.

Lee, T.J., H. Nuree, and Y. Song, "Magnetotelluric survey applied to geothermal exploration: An example at Seokmo Island, Korea", *Exploration Geophysics*, Vol. 41, pp. 61-68, 2010.

Le Pichon, X, and J., Angelier, "The Hellenic arc and trech system: a key to the neotectonic evolution of the eastern Mediterranean area", *Tectonophysics*, Vol. 60, pp. 1-42, 1979.

Lips, A.L.W., D. Cassard, H. Sözbilir, and Y. Yılmaz, "Multistage exhumation of the Menderes Massif, western Anatolia (Turkey)", *International Journal of Earth Sciences*, Vol. 89, pp. 781-792, 2001.

Llera, F.J., M. Sato, K. Nakatsuka, and H. Yokoyama, "Temperature dependence of the electrical resistivity of water saturated rocks", *Geophysics*, Vol.56, pp. 576-585, 1990.

Lubimova, E.A., U.A. Zorin, and S.V. Lysak, “Geothermal anomaly in the Baikal lake region”, *Geothermics*, Vol. 1, pp. 31-34, 1972.

Marti, A., “*A Magnetotelluric Investigation of Geoelectrical Dimensionality and Study of the Central Betic Crustal Structure*”, Ph.D. Thesis, Universitat de Barcelona Department de Geodinmica i Geofísica, 2006.

Meqbel, N.M., G. D. Egbert, P.E. Wannamaker, A. Kelbert, “Deep electrical resistivity structure of the northwestern U.S. derived from 3-D inversion of USArray magnetotelluric data”, *Earth and Planetary Science Letters*, Vol. 402, pp. 290-304, 2014.

McClusky, S., S. Balassanian, A. Barka, C. Demir, S. Ergintav, I. Georgiev, O. Gurkan, M. Hamburger, K. Hurst, H. Kahle, K. Kastens, G. Kekelidze, R. King, V. Kotzev, O. Lenk, S. Mahmoud, A. Mishin, M. Nadariya, A. Ouzounis, D. Paradissis, Y. Peter, M. Prilepin, R. Reilinger, I. Sanli, H. Segeer, A. Tealeb, M.N. Toksöz, and G. Veis, “Global Positioning System constraints on plate kinematics and dynamics in the eastern Mediterranean and Caucasus”, *Journal of Geophysical Research*, Vol. 105, pp. 5695-5719, 2000.

McKenzie, D.P., “Active tectonics of the Alpine-Himalaya belt: the Aegean Sea and surrounding regions”, *Geophysical Journal of the Royal Astronomical Society*, Vol. 55, pp. 217-254, 1978.

Meju, M.A., “Geoelectromagnetic exploration for natural resources: models, case studies and challenges”, *Surveys in Geophysics*, Vol. 23, pp. 133-205, 2002.

Mertoglu, O., S. Sakir, and N. Basarir, “Geothermal country update report of Turkey (2010-2015)”, *Proceedings World Geothermal Congress*, Melbourne, Australia, 2015.

Meqbel, N.M., “*The electrical conductivity structure of the Dead Sea Basin derived from 2D and 3D inversion of magnetotelluric data*”, Dissertation, Freie Universität, Berlin 2009.

Meulenkamp, J.E., W.J.R. Wortel, W.A. VanWamel, and W. Spakman, "On the Hellenic subduction zone and geodynamic evolution of Crete in the late Middle Miocene", *Tectonophysics*, Vol. 146, pp. 203-215, 1988.

Miensopust, M.P., "*Multidimensional Magnetotellurics: A 2D case study and a 3D approach to simultaneously invert for resistivity structure and distortion parameters*", Ph.D. Thesis, National University of Ireland, 2010.

Muffler, P., and R. Cataldi, "Methods for regional assessment of geothermal resources", *Geothermics*, Vol. 7, pp. 53-89, 1978.

Munoz, G. "Exploring for geothermal resources with electromagnetic methods", *Surveys in Geophysics*, Vol. 35, pp. 101-122, 2014.

Mutlu, A.K., and H. Karabulut, "Anisotropic Pn tomography of Turkey and adjacent regions", *Geophysical Journal International*, Vol. 187(3), pp.1743-1758, 2011.

Newman, G.A. E. Gasperikova, G.M. Hoversten, P.E. Wannamaker, "Three-dimensional magnetotelluric characterization of the Coso geothermal field", *Geothermics*, Vol. 37, pp. 369-399, 2008.

Niasari, S.W., "*Magnetotelluric investigation of the Sipoholon geothermal field, Indonesia*", Ph.D. Thesis, GFZ, 2015a.

Niasari, S.W., G. Munoz, M. Kholid, E. Suhanto, and O. Ritter, "3D inversion of Magnetotelluric data from the Sipoholon geothermal field, Sumatra Indonesia", *Proceedings World Geothermal Congress 2015*, Melbourne, Australia, 2015b.

Ogawa, Y., N. Matsushima, H. Oshiman, S. Takakura, M. Utsugi, K. Hirano, M. Igarashi, and T. Doi, "A resistivity cross-section of Usu volcano, Hokkaido, Japan, by audiomagnetotellurics soundings", *Earth Planets and Space*, Vol. 50, pp. 339-346, 1998.

Oner, Z., and Y. Dilek, "Supradetachment basin evolution during continental extension: The Aegean province of western Anatolia, Turkey", *Geological Society of America Bulletin*, Vol. 123, pp. 2115 -2141, 2011.

Oner, Z., and Y. Dilek, "Fault kinematics in supradetachment basin formation, Menderes core complex of western Turkey", *Tectonophysics*, Vol. 608, pp. 1394-1412, 2013.

Oskooi, B., and A. Manzella, "2D inversion of the Magnetotelluric data from Travale geothermal field in Italy", *Journal of the Earth Space Physics*, Vol. 36, pp. 1-18, 2011.

Özen, T., A. Bulbul, and G. Tarcan, "Reservoir and hydrogeochemical characterizations of the Salihli Geothermal Fields in Turkey", *Proceedings World Geothermal Congress*, Bali, Indonesia, 2010.

Özen, T., A. Bulbul, and G. Tarcan, "Reservoir and hydrogeochemical characterizations of geothermal fields in Salihli, Turkey", *Journal of Asian Earth Sciences*, Vol. 60, pp. 1-17, 2012.

Palacky, G.J., "Resistivity characteristics of geologic targets", In: M.N. Nabighian (ed), *Electromagnetic Methods in Applied Geophysics*, Vol. 1, pp. 53-129, 1987.

Parkinson, W.D., "The Influence of Continents and Oceans on Geomagnetic Variations", *The Geophysical Journal of the Royal Astronomical Society*, Vol. 6, pp. 411-449, 1962.

Patro, P.K., "Magnetotelluric studies for hydrocarbon and geothermal resources: Examples from the Asian region", *Surveys in Geophysics*, pp. 1-37, 2017.

Pellerin, L., J.M. Johnston, and G.W. Hohmann, "A numerical evaluation of electromagnetic methods in geothermal exploration", *Geophysics*, Vol. 61, pp. 121-130, 1996.

Pina-Varas, P., J. Ledo, P. Queralt, A. Marcuello, F. Bellmunt, R. Hidalgo, M. Messeiler, “3-D magnetotelluric exploration of Tenerife Geothermal System (Canary Islands, Spain)”, *Surveys in Geophysics*, Vol. 35, pp. 1045-1064, 2014.

Ritter, O., A. Hoffmann-Rothe, P. A. Bedrosian, U. Weckmann and V. Haak, “Electrical Conductivity Images of Active and Fossil Fault Zones”, *The Geological Society of London, Special Publications*, Vol. 245, pp. 165-186, 2005.

Saemundsson, K., “Geothermal systems in global perspective”, *Presented at Short Course IV on Exploration for Geothermal Resources*, Lake Naivasha, Kenya, 2009.

Sari, C., and M. Şalk, “Sediments thicknesses of the western Anatolia graben structures determined by 2D and 3D analysis using gravity data”, *Journal of Asian Earth Sciences*, Vol. 26, pp. 39-48, 2006.

Sass, P., O. Ritter, L. Ratschbacher, J. Tjypel, V.E. Matiukov, A.K. Rybin, V. Yu. Batalev, “Resistivity structure underneath the Pamir and Tian Shan”, *Geophysical Journal International*, Vol. 198, pp. 564-579, 2014.

Saunders, P., K. Priestly, and T. Taymaz, “Variations in the crustal structures beneath western Turkey”, *Geophysical Journal International*, Vol. 134, pp. 373-389, 1998.

Schmucker, U., “Regional induction studies: A review of methods and results”, *Physics of the Earth Planetary Interiors*, Vol. 7, pp. 365-378, 1973.

Selim, H.H., and G. Yanık, “Development of the Cambazlı (Turgutlu/MANISA) fissure-ridge-type travertine and relationship with active tectonics, Gediz Graben, Turkey”, *Quaternary International*, Vol. 199, pp. 157-163, 2009.

Serpen, U., N. Aksoy, T. Öngür, and E.D. Korkmaz, “Geothermal energy in Turkey: 2008 update”, *Geothermics*, Vol. 38, pp. 227-237, 2009.

Seyitoğlu, G., and B.C. Scott, “Age of the Alaşehir graben (west Turkey) and its tectonic implications”, *Geological Journal*, Vol. 31, pp. 1-11, 1996.

Seyitoğlu, G., I. Cemen and O. Tekeli, “Extensional folding in the Alaşehir (Gediz) graben, western Turkey”, *Journal of the Geological Society, London*, Vol. 157, pp. 1097-1100, 2000.

Simpson, F. and K. Bahr, *Practical Magnetotellurics*, Cambridge University Press, 2005.

Sözbilir H., “Oligo-Miocene extension in the Lycian Orogen: evidence from the Lycian molasses basin, SW Turkey”, *J. Geodinamica Acta*, Vol. 18, pp. 255-282, 2005.

Stratton, J. A., *Electromagnetic Theory*, McGraw-Hill Book Co, New York, 1941.

Şengör, A.M.C., and Y. Yılmaz, “Tethyan evolution of Turkey: A plate tectonic approach”, *Tectonophysics*, Vol. 75, pp. 181-241, 1981.

Şengör, A.M.C., N. Görür, and F. Şaroğlu, “Strike-Slip Deformation Basin Formation and Sedimentation: Strike-Slip Faulting and Related Basin Formation in Zones of Tectonic Escape: Turkey as a Case Study. In: Biddle, K.T. and Christie-Blick, N. (Eds.), *Strike-Slip Faulting and Basin Formation*”, *Society of Economic Paleontologists and Mineralogist, Special Publication*, Vol. 37, pp. 227-264, 1985.

Tamanyu, S., and K. Sakaguchi, “Conceptual model for non-volcanic geothermal resources-examples from Tohoku Japan”, *Proceedings European Geothermal Conference*, Szeged, Hungary, Hungarian Geothermal Association, 2003.

Tarcan, G., “Mineral saturation and scaling tendencies of waters discharged from wells (>150 °C) in geothermal areas of Turkey”, *Journal of Volcanology and Geothermal Research*, Vol. 142, pp. 263-283, 2005.

Tarcan, G., S. Filiz, and U. Gemici, “Geology and geochemistry of the Salihli geothermal fields”, *Proceedings World Geothermal Congress*, Kyushu-Tohoku, Japan, 2000.

Ten Dam A., and I. Khrebtov, "The Menderes Massif Geothermal Province", *Geothermics*, Vol. 2, pp. 117-123, 1970.

Tietze, K. and O. Ritter, "Three-dimensional magnetotelluric inversion in practice-the electrical conductivity structure of the San Andreas Fault in Central California", *Geophysical Journal International*, Vol. 195, pp. 130-147, 2013.

Tikhonov, A.N. and V.I. Arsenin, "Solutions of ill-posed problems", *New York: Wiley*, 1977.

Tikhonov, A.N., "On Determining Electrical Characteristics of the Deep Layers of the Earth's Crust", *Doklady*, Vol. 73, pp. 281-285, 1950.

Uchida, T., "Resistivity structure of Sumikawa geothermal field, northeastern Japan, obtained from magnetotelluric data", *Proceedings World Geothermal Congress*, Florence, Italy, 1995.

Uchida, T., T.J. Lee, M. Honda, and A. Andan, "2D and 3D interpretation of magnetotelluric data in the Bajawa geothermal field central Flores, Indonesia", *Bulletin of the Geological Survey of Japan*, Vol. 53, pp. 265-283, 2002.

Uchida, T., "Three-dimensional magnetotelluric investigation in geothermal fields in Japan and Indonesia", *Proceedings World Geothermal Congress*, Antalya, Turkey, 2005.

Uchida, T., and Y. Sasaki, "Stable 3D inversion of MT data and its application to geothermal exploration", *Exploration Geophysics*, Vol. 37, pp. 223-230, 2006.

Uchida, T., "Three- dimensional interpretation of AMT data in Ogiri geothermal field, Japan", *Proceedings World Geothermal Congress*, Bali, Indonesia, 2010.

Uchida, T., S. Takakura, T. Ueda, M. Adachi, H. Ozeki, K. Kamada, and T. Sato, “3D Magnetotelluric survey at the Yanaizu-Nishiyama geothermal field, northern Japan”, *Proceedings of the 9th Geothermal Symposium*, 2011.

Ucok, H., I. Ershaghi, and G. Olhoeft, “Electrical resistivity of geothermal brines”, *Journal of Petroleum Technology*, Vol.32, pp.717-727, 1980.

Ulugergerli, E.U., G. Seyitoğlu, A.T. Başokur, C. Kaya, U. Dikmen, and M.E. Candansayar, “The Geoelectrical Structure of Northwestern Anatoli, Turkey”, *Pure and Applied Geophysics*, Vol. 164, pp. 999-1026, 2007.

Ussher, G., C. Harvey, R. Johnstone, and E. Anderson, “Understanding the resistivities observed in geothermal systems”, *Proceedings World Geothermal Congress*, Kyushu-Tohoku, Japan, 2000.

Uzel, B., C.G. Langereis, N. Kaymakci, H. Sözbilir, Ç. Özkaymak, and M. Özkaptan, “Paleomagnetic evidence for an inverse rotation history of Western Anatolia during exhumation of Menderes core complex”, *Earth Planet. Sci. Lett.*, Vol. 414, pp. 108-125, 2015.

Vanacone, E.A., T. Taymaz, and E. Saygin, “Moho structure of the Anatolian Plate from receiver function analysis”, *Geophysical Journal International*, Vol. 193, pp. 329-337, 2013.

Vozoff, K., “*The Magnetotelluric Method*”, in Nabighian, M. N., Ed., *Electromagnetic Methods in Applied Geophysics: SEG., 2B*, pp. 641-711, 1991.

Wang, T., and G.W. Hohmann, “A finite-difference, time-domain solution for three-dimensional electromagnetic modeling”, *Geophysics*, Vol. 58, pp. 797–809, 1993.

Wannamaker, P.E., P.E. Rose, W.M. Doerner, B.C. Berard, J. McCulloch, and K. Nurse, “Magnetotelluric surveying and monitoring at the Coso geothermal area, California, in

support of the enhanced geothermal systems concept: survey parameters and initial results”, *Proceedings Twenty-Ninth Workshop on Geothermal Reservoir Engineering*, Stanford, California, 2004.

Ward, H. Stanley, and G. W., Hohmann, “Electromagnetic Theory for Geophysical Applications”, *Electromagnetic Methods in Applied Geophysics*, Vol. 1, pp. 130-311, 1987.

Weaver, J.T., A.K. Agarwal, and F.E.M. Lilley, “Characterization of the magnetotelluric tensor in terms of its invariants”, *Geophysical Journal International*, Vol. 141, pp. 321-336, 2000.

Weidelt, P., “The inverse problem of geomagnetic induction”, *Zeitschrift für Geophysik*, Vol. 38, pp. 257-289, 1972.

Wiese, H., “Geomagnetische Tiefentellurik. II. Die Streichrichtung der Untergrundstrukturen des elektrischen Widerstandes, erschlossen aus geomagnetischen Variationen”, *Geofis. Pura. Appl.*, Vol. 52, pp. 83-103, 1962.

Wyatt, A. (ed), “*Challinor’s Dictionary of Geology (Sixth Edition)*”, University of Wales Press, Cardiff, p. 374, 1986.

Williams, C.F., M.J. Reed, and A.F. Anderson, “Updating the classification of geothermal resources”, *Proceedings of the Thirty-Sixth Workshop on Geothermal Reservoir Engineering*, Stanford University, California, U.S.A., 2011.

Yee, K. S., “Numerical solution of initial boundary value problems involving Maxwell’s equations in isotropic media”, *IEEE Transactions on Antennas and Propagation*, Vol. 14, pp. 302-307, 1966.

Yilmazer, S., S. Pasvanoğlu, and S. Vural, “The relation of geothermal resources with young tectonics in the Gediz Graben (West Anatolia) and their hydrogeochemical analyses”, *Proceedings World Geothermal Congress*, Bali, Indonesia, 2010.

Yin, Y., S. Jin, W. Wei, M. Santosh, H. Dong, C. Xie, “Construction and destruction of the North China Craton with implications for metallogeny: Magnetotelluric evidence from the Hengshan-Wutai-Fuping region within Trans-North China Orogen”, *Gondwana Research*, Vol. 40, pp. 21-42, 2016.

Yin, Y., S. Jin, W. Wei, G. Ye, J. Jing, L. Zhang, H. Dong, C. Xie, H. Liang, “Lithospheric rheological heterogeneity across an intraplate rift basin (Linfen Basin, North China) constrained from magnetotelluric data: Implications for seismicity and rift evolution”, *Tectonophysics*, Vol. 717, pp. 1-15, 2017.

Zhang, L., T. Hao, Q. Xiao, J. Wang, L. Zhou, M. Qi, X. Cui, and N. Cai, “Magnetotelluric investigation of the geothermal anomaly in Hailin, Mudanjiang, northeastern China”, *Journal of Applied Geophysics*, Vol. 118, pp. 45-65, 2015.

Zhdanov, M.S., *Inverse Theory and Applications in Geophysics*, Elsevier, 2015.

Zhu, L., B.J. Mitchell, N. Akyol, I. Cemen, and K. Kekovali, “Crustal thickness variations in the Aegean region and implications for the extension of the continental crust”, *Journal of Geophysical Research*, Vol. 111, B01301, 2006.

APPENDIX A: SKEW ANGLES

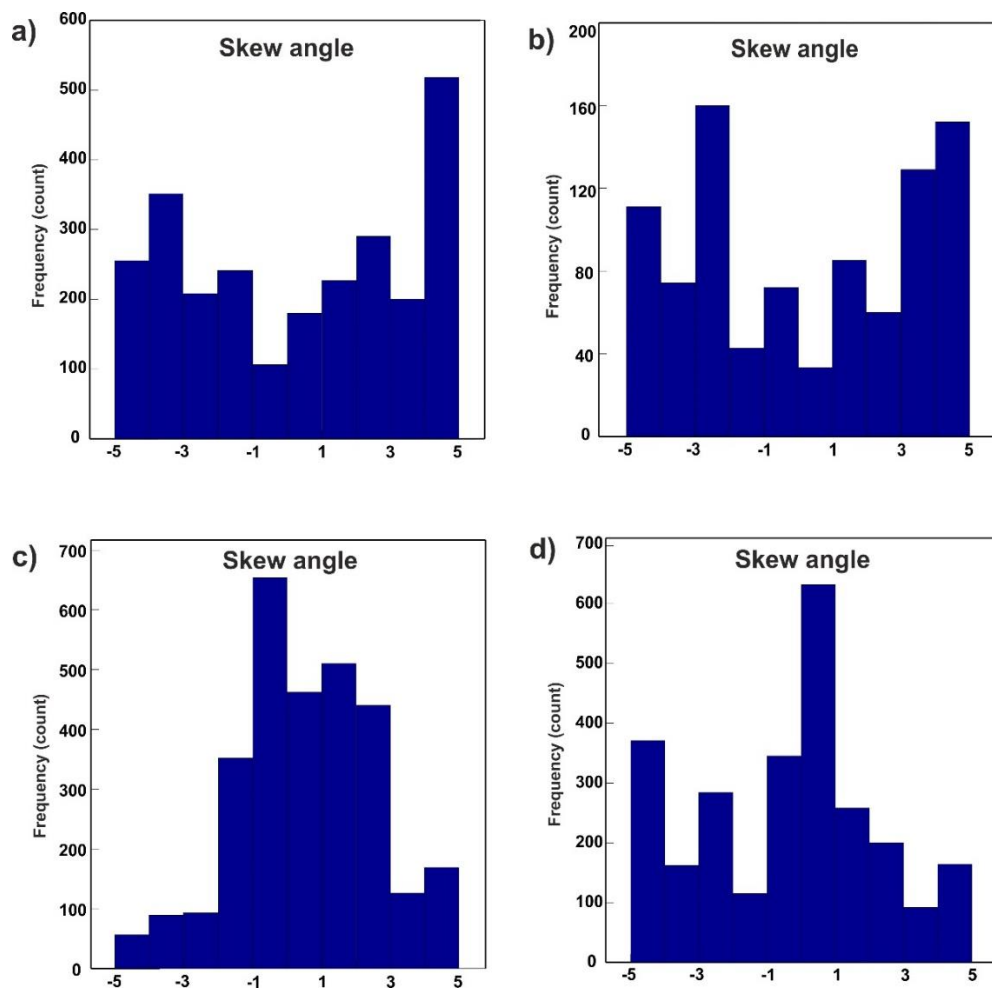


Figure A.1. The histograms showing the skew angles at each investigation area, area A (a), B (b), C (c) and D (d).

APPENDIX B: INITIAL MODELS

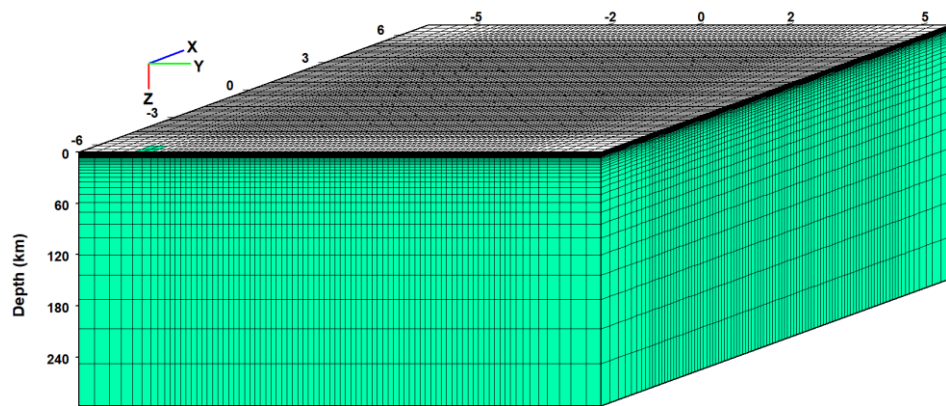


Figure B.1. A schematic view of the 3D model used for the inversion in investigation area A. X- and Y-axes denote N-S and E-W directions, respectively. Z-axis is downwards. The MT sites are located at the center of the grid.

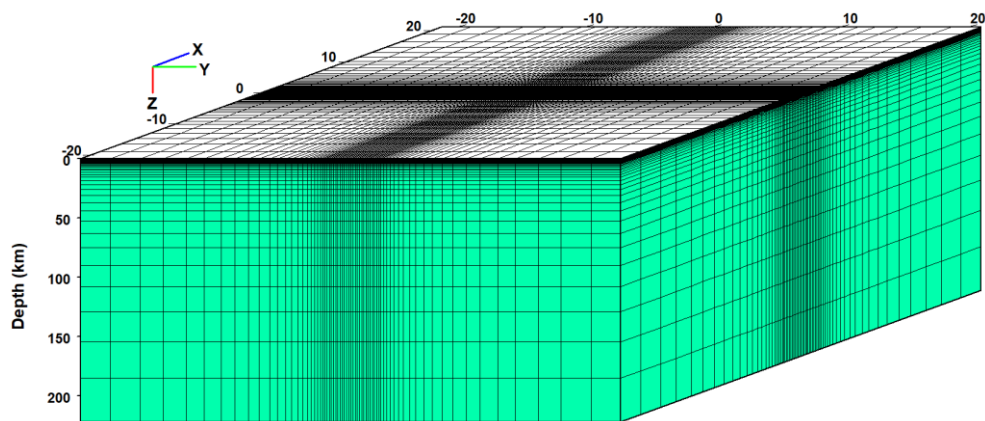


Figure B.2. A schematic view of the 3D model used for the inversion in investigation area B. X- and Y-axes denote N-S and E-W directions, respectively. Z-axis is downwards. The MT sites are located at the center of the grid.

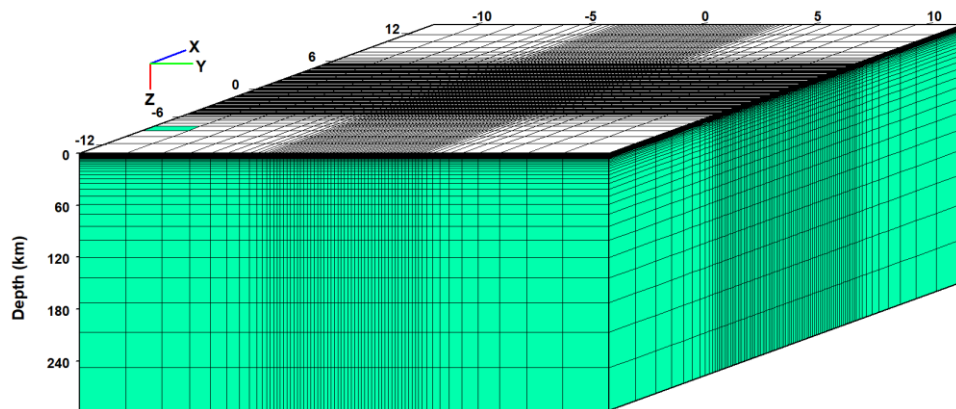


Figure B.3. A schematic view of the 3D model used for the inversion in investigation area C. X- and Y-axes denote N-S and E-W directions, respectively. Z-axis is downwards. The MT sites are located at the center of the grid.

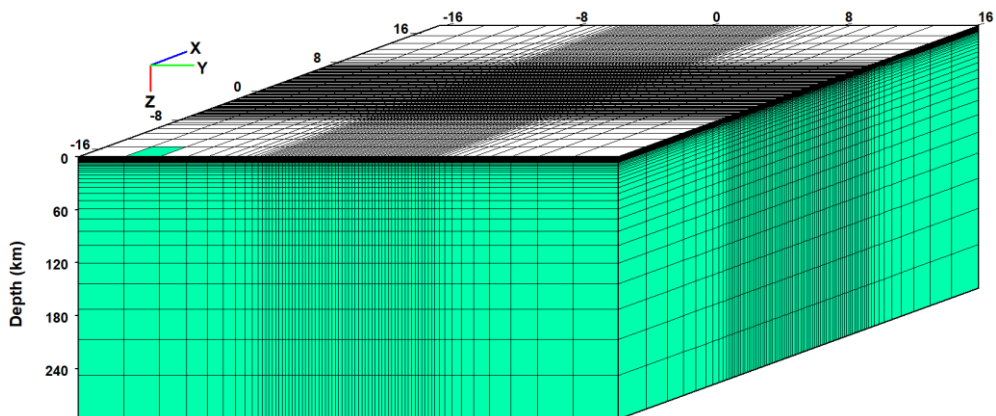


Figure B.4. A schematic view of the 3D model used for the inversion in investigation area D. X- and Y-axes denote N-S and E-W directions, respectively. Z-axis is downwards. The MT sites are located at the center of the grid.

APPENDIX C: DATA MISFITS

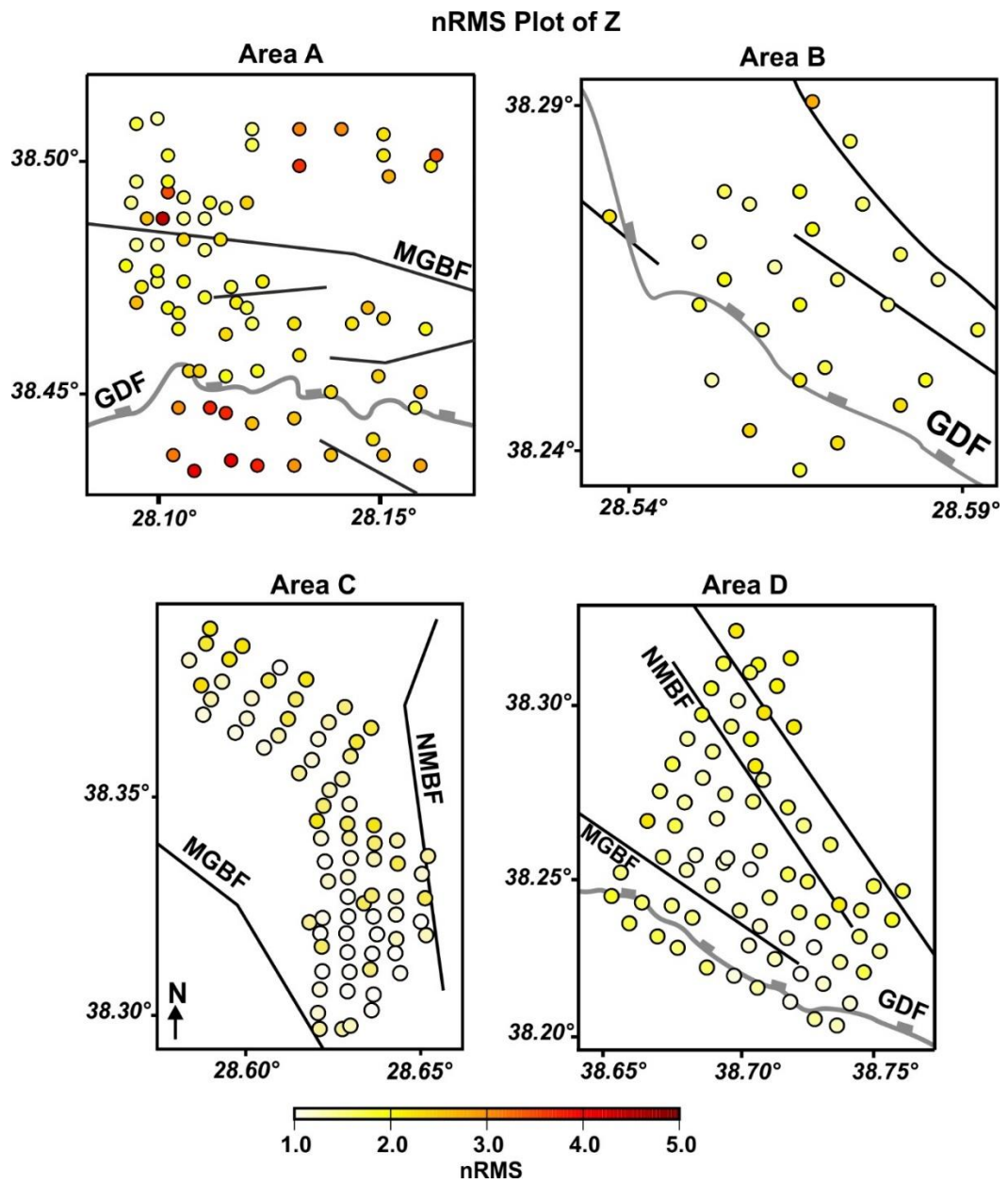


Figure C.1. Data fits presented as nRMS at each investigation area (A, B, C and D) for full impedance tensor (Z).